Abstract

The employment of X-ray computed microtomography has been an excellent 3D imaging technique to explore subsurface multiphase flow and trapping at pore-scale which are important for environmental applications and petroleum-engineering processes. There is a need to apply new techniques to recover the remaining oil in the existing reservoirs to meet the expected increased demand for oil. Nanotechnology applications have received lots of attention in the oil industry, particularly because of its significant potential for enhanced oil recovery as a new method. However, pore-scale investigation of the capability of nanoparticles to recover more oil is limited in literature.

This study evaluates the effect of Silica-based nanofluid on the remaining oil saturation at pore-scale employing X-ray microtomography. It investigates the connectivity of the residual oil phase after nanofluid flooding under different capillary numbers. It also compares the remaining oil phase saturation and topology after nanofluid flooding to non-nanofluid flooding at same capillary numbers. The induced oil recovery and change in oil topology after nanofluid tertiary recovery is also characterized.

This study used Bentheimer sandstone samples with 4 mm diameter, with crude oil as the non-wetting phase, and with brine (7 wt% CsCl) and nanofluid (7 wt% CsCl + 0.1 wt% silica nanoparticles) as the wetting phase. This study successfully built a core-flooding setup integrated with a high-resolution X-ray micro-tomography scanner to capture the pore-scale fluid configuration. Seven experiments were performed during this study, and the produced 3D images were processed and analysed to quantify the remaining oil saturation, oil recovery, and normalized Euler characteristic. In addition, the fraction of grain surfaces wetted with the aqueous phase was quantified for all the experiments based on a method described in this study.

The results showed a reduction in the residual oil saturation and connectivity with increasing the capillary number for the non-nanofluid imbibition tests. At same capillary numbers, the silica nanoparticles reduced trapping efficiency, internal connectivity and size of the remaining oil clusters. However, it was observed that the silica nanoparticles were more effective. In addition, it was found that the nanoparticles had a unique ability to disconnect the remaining oil phase even when the remaining oil phase saturation was high. This ability of the nanoparticles resulted in a higher oil recovery after nanofluid tertiary recovery.

Furthermore, the nanoparticles were significantly able to detach the oil phase from the grain surfaces as shown by the surface area index. The surface area indices evaluated for the nanofluid experiments were always higher compared to the non-nanofluid experiments at the same capillary numbers.

Acknowledgements

I would fist like to express my profound gratitude to my thesis supervisor Prof. Ole Torsæter for his continuous support, considerable encouragement, and valuable comments and remarks.

I cannot express how grateful I am to have amazing parents who emotionally and financially supported me throughout this journey at NTNU. My mother's daily messages to keep me motivated significantly have had a positive impact on my work during this study. Special thanks also go to my supportive siblings: Sundus, Talal, Nasr and Salma.

I will forever be appreciative for the knowledge and skills that I have acquired while working with postdoctoral fellow Haili Long-Sanouiller. I would like also to thank Eng. Roger Overå for providing the equipment and materials I needed to build the experimental setup, and for teaching me valuable laboratory skills. In addition, I really appreciate PhD candidate Alberto Bila for sharing the knowledge about nanotechnology for EOR on core-scale. I am grateful to Prof. Carl Fredrik Berg, Prof. Per Arne Slotte, and postdoctoral fellow Hamid Hosseinzade for the valuable discussion and feedback.

Furthermore, I would like to thank Amine Bouhouche for being a real friend and I am forever indebted for your support and advice. Last but not least, thanks to all of the friends that I made at NTNU who helped to add enjoyment to this journey since 2016: Fenna Verkerk, Jose Kastanjetre, Sofia Soloperto, Berta Pzvz, Bernardo Camargo, Amaury a. Toloza, Stephen Kohler, Ole Aleksander Hansen, Mohamed Fathy, Andreea Chiriac, Gustavo Góngora, and Ivana maslonková.

Trondheim, Norway – January, 2019.
Salem Akarri

Table of Contents

List of Figures

List of Tables

Abbreviations and Nomenclature

$\boldsymbol{\theta_A}$	Advancing contact angle
$\boldsymbol{\theta_H}$	Hinging contact angle
$\boldsymbol{\theta_R}$	Receding contact angle
$\boldsymbol{\chi_{NW}}$	Composite Euler number for non-wetting phase
2D	Two-dimensional
3D	Three-dimensional
A	Cross-sectional area
a	Aspect ratio
AM	Arc meniscus
$\mathbf{A_{wo}}$	Grain surface area wetted by oil
$\mathbf{A_{ww}}$	Grain surface area wetted by water
$\mathbf{C_a}$	Capillary number
$\mathbf{CO_2}$	Carbon dioxide
D	Diameter
e.g.	exempli gratia (for example)
EOR	Enhanced oil recovery
i.e.	id est (that is)
IFT	Interfacial Tension
K	Permeability
L	Length
micro-CT, mCT, & CMT	Computed microtomography
NPs	Nanoparticles
nw	Non-wetting
Ø	Porosity
$\mathbf{P_c}$	Capillary pressure
$\mathbf{P_c^{max}}$	Threshold capillary pressure
r	Radius
R.F.	Recovery factor
$\mathbf{R^2}$	Coefficient of determination
REV	Representative elementary volume
S.A.I.	Surface area index
$\mathbf{S_o}$	Oil saturation
$\mathbf{S_{or}}$	Remaining oil saturation
$\mathbf{S_w}$	Water saturation
$\mathbf{S_{wi}}$	Irreducible water saturation
TM	Terminal meniscus
U	Superficial velocity
$\mathbf{V_B}$	Bulk volume
$\mathbf{v_{in}}$	Inner contact line velocity
Vp	Pore volume
w	Wetting
wt. %	Weight percent
$\boldsymbol{\beta_0}$	Zeroth Betti number
$\boldsymbol{\beta_1}$	First Betti number
$\boldsymbol{\beta_2}$	Second Betti number
μm	Micron (equals to 1×10^{-6} meter)
$\boldsymbol{\pi}$	Pi number (≈ 3.14159)
$\boldsymbol{\sigma}$	Interfacial tension

Q	Flow rate
T_a	Advective transport time
T_f	Layering formation time
κ	Total curvature
μ_{INV}	Invading phase viscosity
v_{INV}	Invading phase velocity

Chapter 1

Introduction

1.1 Motivation

Multi-phase flow and trapping in natural subsurface porous media has been considered highly significant for environmental applications and petroleum-engineering processes such as geologic sequestration of CO_2, and hydrocarbon recovery [1-3]. The employment of X-ray computed microtomography (also known as micro-CT, mCT, X-ray CMT) has been an excellent 3D imaging technique to explore subsurface multiphase flow and trapping owing to the superb features offered by this technology [1, 4].

First of all, this imaging technique non-destructively generates reliable three-dimensional images for the examined material, i.e. porous media and saturating fluids [1]. In addition, this imaging approach provides high spatial resolutions, enabling the identification and resolution of the rock-fluid, fluid-fluid and fluid-rock-fluid interfaces [1], which are important for the examination of the amount, distribution, and connectivity of fluids within the porous material [4]. Moreover, this technique provides a representative elementary volume (REV) scale [1], which is required for the pore-scale investigation of fluids flow and trapping in porous media and was confirmed by the REV analysis presented in [2, 4].

In addition to the high spatial resolutions of this technique, synchrotron-based fast micro-CT scanners have upgraded this state of the art technique by offering high temporal resolutions [1]. This technology has enabled the capture of flow dynamics in porous media, which significantly helped to overcome the lack of understanding of pore-scale dynamic transient process between the initial state (i.e. connected non-wetting phase, known as *post drainage*) and final state (i.e. trapped non-wetting phase as immobile clusters, known as *post imbibition*) [4-9]. Moreover, the feasibility offered by micro-CT scanners to perform surface and sub-surface conditions experiments inside the machine chamber on the scanning stage is a vital feature [1, 2, 10-12].

X-ray microtomography has significantly helped to establish a pore-scale perspective on multiphase flow and trapping in porous media [13]. In recent years, there have been many interesting and valuable publications employing micro-CT scanners, investigating this topic to build a pore-scale understanding of the occurring processes and controlling properties to optimize the engineering of hydrocarbon recovery and geological storage of CO_2. In-situ wettability, flow regimes, pore-scale dynamic mechanisms, phase topology, pore-network

statistics, property prediction, and flow modelling are key examples of the published work in this area of research [2, 5, 7-9, 11, 13-19].

Wettability is still not a fully understandable concept when it is used to explain pore-scale displacements. Literature lacks scientific laws and equations to describe wettability and its relation to multiphase flow and trapping. Recently significant consideration has been subjected to understand in-situ wettability and to replace the conventional methods providing an average value of the wetting state of a porous system [11, 12, 20, 21]. Wettability is vital since it plays a critical role in multiphase flow and trapping mechanisms at pore-scale in reservoirs where the target is to recover hydrocarbon or trap carbon dioxide (CO_2), particularly by strongly affecting capillary pressures, relative permeability and fluid saturations (i.e. residual non-wetting phase saturation) [10-12, 22].

The IEA (International Energy Agency) reported in its world energy outlook (2018) that energy demand may increase by more than 25% in 2040, and that a gap in supply of oil is expected in 2020 due to the increase in the world population and higher activities in the petrochemical industry [23]. Discovering new oil fields has recently been difficult and as the result the proven world reserves of oil are not increasing in the last years according to the BP statistical review of world energy 2018 [24]. Therefore, there is a need to apply new techniques to recover the remaining oil in the existing reservoirs.

Enhanced oil recovery (EOR) is a recovery stage to increase the microscopic displacement and volumetric sweep efficiency of the oil to reduce the residual oil in place via several methods such as chemical flooding [25, 26]. Nanotechnology applications have received lots of attention in the oil industry, particularly because of its significant potential for enhanced oil recovery as a new method [25-27]. In addition, it is also considered as a potential improver of the conventional EOR techniques such as polymer (chemical) EOR [25-27]. The available research on nanotechnology for EOR showed positive impact on reducing the remaining oil saturations mainly on core-scale experiments. Few pore-scale studies are available to investigate the mechanisms deriving the nanofluids to produce more oil and the pore-scale changes in the fluid configuration post the nano-flooding.

1.2 Objectives

This master thesis aims to achieve three main objectives:

1. To build a new flooding setup for miniature samples and to be successfully integrated with a micro-CT scanner in the reservoir laboratory in the Norwegian University of Science and Technology (NTNU).
2. To utilize the new experimental setup to perform pore-scale experiments to provide new insights for the use of nanoparticles to reduce the amount of trapped crude oil in natural rock samples, i.e. Bentheimer sandstone.
3. To investigate the usefulness of a surface wetting descriptor extracted from micro-CT images, which has never been reported in literature before.

1.3 Thesis Structure

The structure of this master thesis is as follows:

Chapter 1: It gives the motivation of this master thesis, objections and the way the thesis is structured.

Chapter 2: It investigates the displacement processes at pore-scale from a simplified modelling point of view and micro-CT experimental observations. Secondly, it discusses two important displacement processes of flow and trapping in porous media; specifically, Euler characteristic and in-situ contact angle. Last but not least, it explores the factors controlling trapping in porous media, which are considerably connected to the displacement processes and descriptors.

Chapter 3: It explores two main mechanisms responsible for the increased oil recovery by nanoparticles (NPs): reduction in wettability alteration, and interfacial tension. Secondly, it presents the findings on nanotechnology for EOR via the use of X-ray microtomography from literature.

Chapter 4: It firstly provides the method to quantify a surface area index to describe wetting of surfaces from micro-CT images. After that, it uses two open 3D data for flow and trapping experiments. The surface area index is calculated to correlate it to in-situ contact angle as well as fluid topology and pore-scale events.

Chapter 5: Properties of the rock and fluids used in the experiments of this study are given. Then, it describes the experimental setup designed for this thesis, followed experimental procedures, and an overview of the experiments.

Chapter 6: Results and discussion of 7 experiments are presented, including: comparisons between the experiments.

Chapter 7: The conclusions based on the image analysis performed on open data in chapter 4, and the experimental work presented in chapter 5 and chapter 6 are provided. It is followed by recommendations to enhance the quality and efficiency of the work presented in this study. Finally, a list of potential experimental studies is presented, to gain in-depth knowledge about the surface area index and nanotechnology for EOR. The following is a list of potential experimental studies.

Chapter 2

Flow and Trapping in Porous Media: A Literature Review

This chapter firstly investigates the displacement processes at pore-scale from a simplified modelling point of view and micro-CT experimental observations. Secondly, it discusses two important displacement processes of flow and trapping in porous media; specifically, Euler characteristic and in-situ contact angle. Last but not least, it explores the factors controlling trapping in porous media, which are considerably connected to the displacement processes and descriptors.

2.1 Pore-Scale Displacement Processes

A porous medium with two fluid phases (i.e. water and oil) in contact with the solid surfaces has one of these two fluids coating, or spreading on, more of the solid surfaces, hence, it is called the wetting phase [28, 29]. The other fluid phase with less preference to spread on the solid surfaces is denoted as the non-wetting phase [28, 29]. Based on this classification of fluid phases in a porous material into: wetting and non-wetting phases, the displacement processes are classified into a drainage process (the displacement of the wetting phase by the non-wetting phase) and imbibition process (the displacement of the non-wetting phase with the wetting phase) [8, 11, 13, 29]. However, the two processes are not perfectly reversible, since they have different local displacement mechanisms owing to several factors such as wettability of the rock matrix [29].

Consider a reservoir to be fully saturated with water (wetting phase), then the hydrocarbon migration from a source rock to the reservoir is a primary drainage process, while the injection of water to increase the oil recovery from this reservoir is an imbibition process [2, 13, 29]. In addition, injection of CO_2 to store it in a saline aquifer is considered to be drainage, and the flow back of the water to the porous rock is an imbibition process leading to CO_2 trapping [4, 13, 29].

This section presents simplified models for the pore-space of the medium and assumes that the flow is capillary-dominated, excluding viscous forces, for the description of drainage and imbibition. Therefore, this discussion does not account for flow in near-wellbore regions, which is viscous-dominated [2]. For a capillary-dominated flow, it is important to introduce the Young-Laplace equation which includes capillary pressure (P_c), interfacial tension (σ), and principal radii of curvature (r_1 and r_2), see equation 1 [13, 21, 30]. Moreover, the capillary

pressure (P_c) can be written in terms of total curvature (κ) of fluid-fluid interface, see equation 2 [13], which is the difference between the non-wetting phase pressure (P_{nw}) and the wetting phase pressure (P_w), see equation 3 [13, 31].

$$P_c = \sigma \left(\frac{1}{r_1} + \frac{1}{r_2}\right) \quad (1)$$

$$P_c = \sigma\kappa, \quad where\ \kappa = \left(\frac{1}{r_1} + \frac{1}{r_2}\right) \quad (2)$$

$$P_c = P_{nw} - P_w \quad (3)$$

Consider a cylindrical tube comprising two fluid phases, see Figure 1, where (r) is the radius of the cylindrical tube, (θ) is the contact angle, (R_c) is the mean radius of curvature [21]. Since $r_1 = r_2 = \frac{r}{\cos(\theta)} = \frac{1}{R_c}$, leading to equation 4 and 5 [13, 21]:

$$P_c = \frac{2\,\sigma\cos(\theta)}{r} \quad (4)$$

$$P_c = \frac{2\,\sigma}{R_c} \quad (5)$$

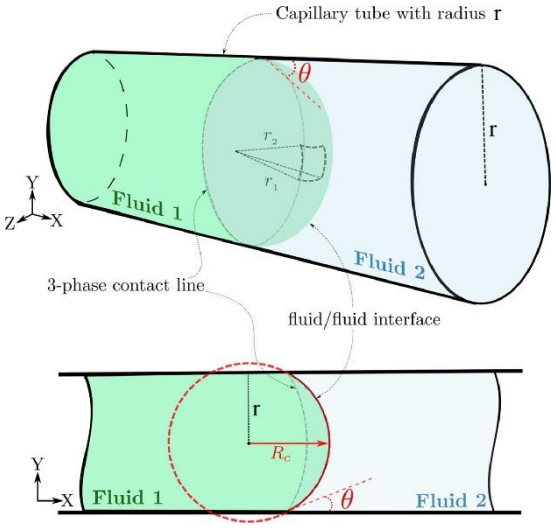

Figure 1: A schematic view of a cylindrical tube containing two fluid phases [21]

2.1.1 Drainage

For a porous medium completely filled with a wetting phase, if a non-wetting phase is introduced to the system, i.e. drainage process, the non-wetting phase pressure (P_{nw}) will gradually increase, leading to an increase in the capillary pressure (P_c), according to equation 3 [11, 13]. Figure 2 shows a small extracted area from a micro-CT image of a dry scan (pore-

space is not filled with fluids), where large bodies are called pores (widest regions) which are connected by narrow regions called pore-throats [21, 32-34].

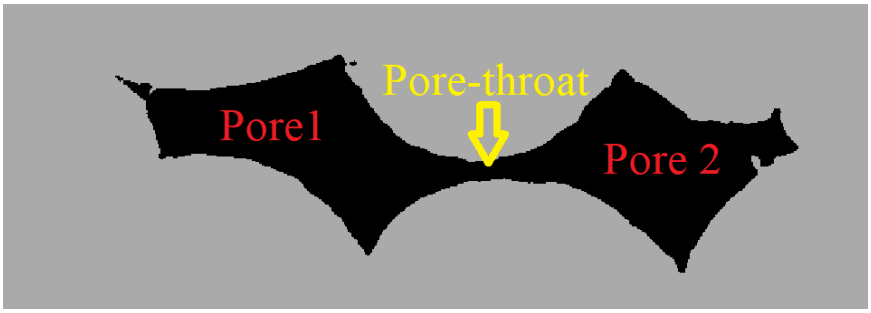

Figure 2: 2D micro-CT image of grains in gray and pore-space in black from experiment I1 in chapter 6

For simplicity, consider the pores and pore-throats to have a circular cross-section, then equation 4 suggests that for wide regions (i.e. pores) with large radius (r), the capillary pressure will be small [13]. Similarly, the capillary pressure should be large to minimize the radius of curvature of the fluid-fluid interface to fit in the pore-throats (narrow regions) [13]. Khishvand et al (2016) observed from micro-CT images that the non-wetting phase will fill easily the widest pore-space elements in the beginning of the drainage process since they have lower requirement of the capillary pressure compared to passing the pore-throats, which is termed the threshold entry pressure [11].

During drainage, the contact angle in equation 4 is a (wetting phase) receding contact angle (θ_R), see equation 6 [11, 13, 35]. It is also worth mentioning that the fluid-fluid interface, during drainage, passing from one pore to another through pore-throats is called a terminal meniscus (TM) interface [11, 13]. There are two features of this interface separating between the non-wetting and wetting phase at the pore-throat junction: (1) it blocks the flow path when it is in the pore elements, (2) the principal radii of curvature are almost equal ($r_1 \approx r_2$) [11, 13]. Figure 3 shows a terminal meniscus (TM) interface between oil in red and brine in blue at the entry of a pore-throat, where grain is in grey. It also shows the interface between the oil and brine in a corner, which is called an arc meniscus (AM) interface [11, 13].

$$P_c = \frac{2\,\sigma\cos(\theta_R)}{r} \qquad (6)$$

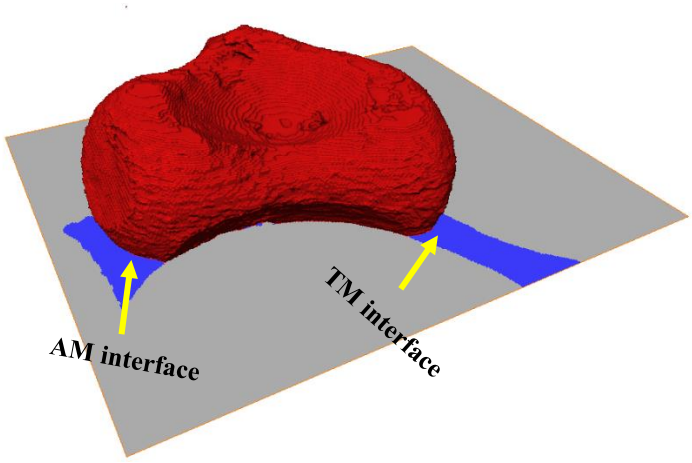

Figure 3: An AM and TM interface between oil and brine from dataset 1 in chapter 4

Figure 4 shows how the oil-water TM interface changes according to the size of the region; a) in the pore far from the throat, b) in the pore but near to the throat, and c) after passing the centre of the pore-throat [35]. Therefore, the local capillary pressure will increase (to pass a throat) and decrease (once the interface is in the pore region) to progress through the pore space during the drainage process [13]. Therefore, the progress of a drainage process is significantly controlled by the size/geometry of the throats [13] [35], in other words, the threshold throat-entry capillary pressures between the non-wetting and wetting phase highly govern the process under capillary-dominated flow i.e. quasistatic flow [36].

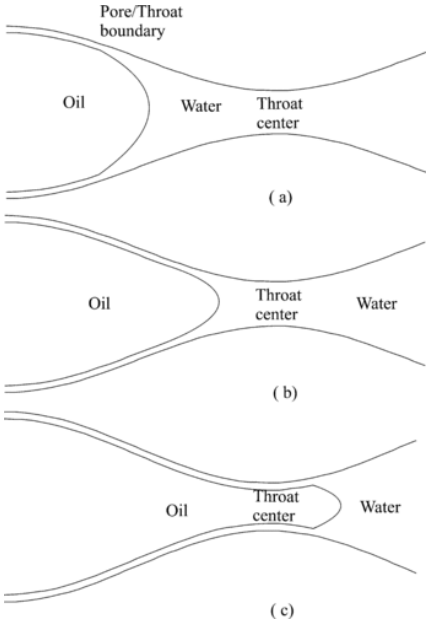

Figure 4: (TM) interface changes its curvature according to the size of the region i.e. pore or throat [35]

Haines jump. The TM interface leaves the pore-throat (high pressure region) to the bounding pore (low pressure region), which creates a pressure gradient leading to an instantaneous filling of the pore bodies, known as the Haines jump [21, 29, 36]. Consider a constant non-wetting

phase pressure (P_{nw}), after the fast invasion of the pore, and the TM interface is at the entry of the throats connected to the current filled pore-body with the non-wetting phase. The throats satisfying the entry threshold pressure will be invaded and more pores will be rapidly filled by the Haines jump [29, 36]. The throats not satisfying the entry conditions are not invaded unless the capillary pressure is high enough, particularly in the early time of drainage [11, 21].

Bultreys et al (2015) captured the Haines jump, see Figure 5, in a Bentheimer sandstone (a pore body in light gray and a pore-throat in black) using fast micro-CT scanner and found that the oil phase, in red, passed the throat and filled the pore body, indicated by the arrow, during 4 seconds (from t = 136 s to t = 140 s) [37]. However, Armstrong et al (2015) show that Haines jumps happen very fast in milliseconds as shown in Figure 6 [38]. It is obvious that the fluids flow is significantly faster (283 ft/day to 2830 ft/day, from this example) at pore-scale during this event compared to the considered average global velocity in a reservoir. Nevertheless, these rapid events have a significant effect on the fluid distribution and connectivity within the porous material [29]. For example, consider a large pore body that will be filled with Haines jump, the source of the non-wetting i.e. oil will be from the previously filled pore elements, leading to a redistribution of the fluids [38].

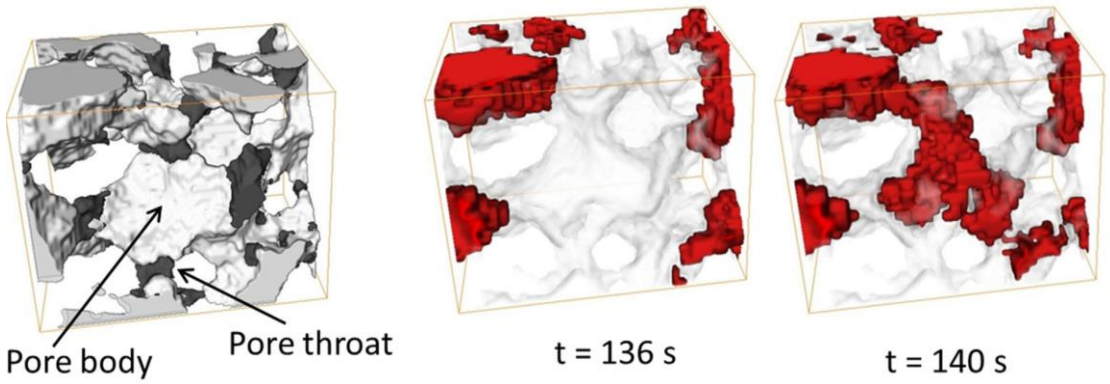

Figure 5: Presentation of Haines jump in a Bentheimer sandstone captured using micro-CT [37]

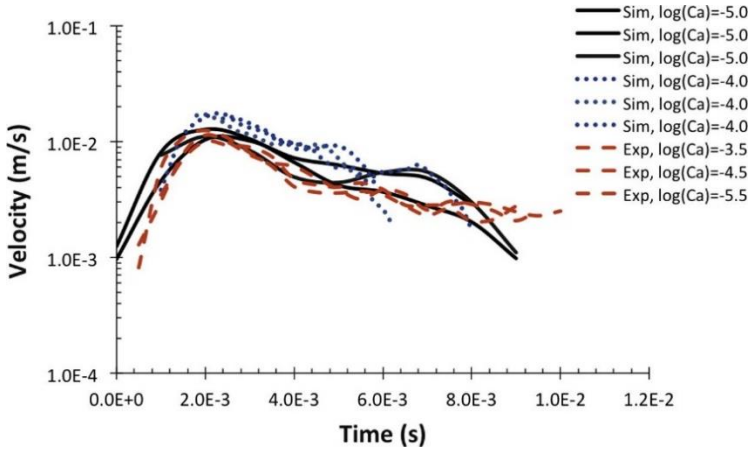

Figure 6: Results for the velocity of the TM interface during a Haines jump [37]

Post-invasion. The displacement of the wetting phase by the non-wetting phase is not a 100% efficient process such that it leaves some of the wetting phase in the narrowest regions of the porous media [13, 35]. For instance, leaving layers of the wetting phase in the corners of the throats after the passage of the TM interface [13, 35]. Figure 7 shows similar wetting layers (in gray) in a throat being displaced by a non-wetting phase [13, 35]. The wetting layers are kept in the corners, with an arc menisci (AM) interface, by the force of the threshold capillary pressure (or P_c^{max}) in the throat [13, 35].

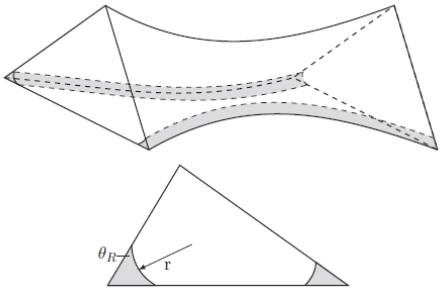

Figure 7: Wetting layers (in gray) along corners of a throat (top) and cross-section of the throat (bottom) [13]

During a Haines jump, since the TM interface rapidly moves to the pore after passing the pore-throat, there can be a disconnection in the non-wetting phase in the pore-throat [29, 35]. The reason behind it is the drop in the capillary pressure since the non-wetting phase will be in a wider region, leading to a reduction in the force pushing the wetting layers to the corners of the pore-throat, which can result in separating the non-wetting phase into two components [13, 35]. Therefore, a small distinct non-wetting ganglion can form in the new pore-body [32]. This mechanism is called snap-off, and since it occurs by displacing the non-wetting phase by the wetting phase, it is a local imbibition event during drainage [13, 32, 35]. Figure 8 shows localized imbibition of water at the narrowest region of the pore-throat to snap off the oil phase

to create an oil ganglion on the right side of the pore-throat [35]. Herring et al (2018) noticed that the frequency of the local snap-off during drainage is related to the non-wetting saturation in the system such that it is increases with increasing the non-wetting phase saturation [29].

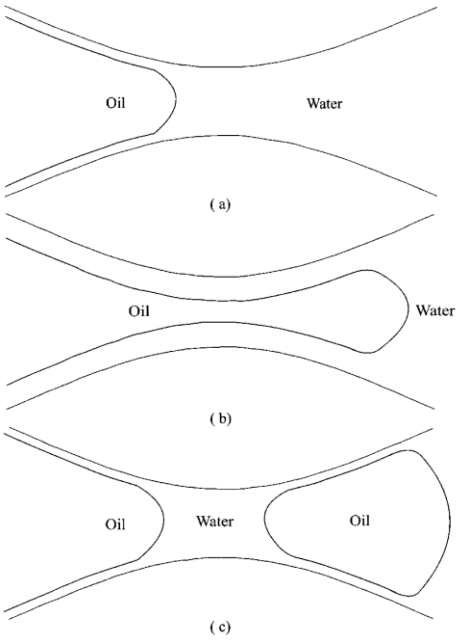

Figure 8: (a) oil at the throat entry, (b) oil invading a wider pore element, & (c) water snaps off oil [35]

2.1.2 Imbibition

Consider the state of the porous medium after the drainage process, where the non-wetting phase fills the centres of the pores and throats, while the wetting-phase is forced to stay in the narrow regions (i.e. corners) of the solid matrix in the form of connected wetting layers [13, 29]. Post-drainage at irreducible wetting phase saturation (S_{wi}), most of volume of the non-wetting fluid phase exists as a single component i.e. a large cluster and the remaining volume will be in a form of very small ganglia/clusters [5], see Figure 9. This section discusses two main machinimas for the imbibition of the wetting phase to displace the non-wetting fluid phase: snap-off and piston-like displacement.

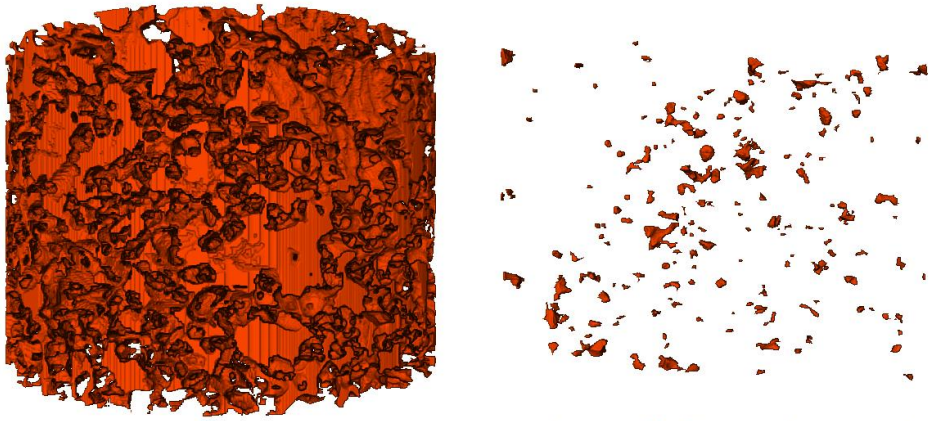

a) Biggest cluster that contains 99% of the total oil

b) Small clusters that contain 1% of the total oil

Figure 9: Demonstration of the cluster-volume state of oil after drainage from dataset 2 in chapter 4

2.1.2.1 Snap-Off Mechanism

The initial local capillary pressure at the AM interface (with receding contact angle θ_R) is high in the beginning of an imbibition process, but it progressively decreases as more of the wetting phase is added to the system (P_w increases in equation 3) [13]. Meanwhile, at the narrowest regions of the media, i.e. throats, the force on wetting layers will start to reduce, leading to increase in the volume of the wetting phase, (known as swelling) [13, 29, 35]. In addition, the injected wetting phase to the system will not flow out of the system in the early time of the imbibition process, therefore, it will accumulate in these layers, leading also to swelling of the layers [35].

However, the interface location will be pinned at its location until a maximum value of the contact angle is attained, which is called the (wetting phase) advancing contact angle (θ_A) [11, 13]. Any contact angle observed between the initial receding contact angle (corresponding to $P_c^{\max}$ post drainage) and the advancing contact angle (corresponding to P_c^{adv} required to move the interface) is called a hinging contact angle θ_H [11, 13]. The AM interface starts to move with an advancing θ_A towards the centre of the throat (known as swelling of the layers), and if the swelling wetting layers meet in the centre of the pore-throat (corresponding to a capillary pressure called the critical P_c), the non-wetting phase will be snapped-off, i.e. the contact with the solid matrix is eliminated [13]. Figure 10 shows the size increase in the wetting phase (in blue) and decrease in the non-wetting volume size in a cross-section of a throat in sandstone rock (in light gray) until snap-off happens at t = 61 min 26 s [39].

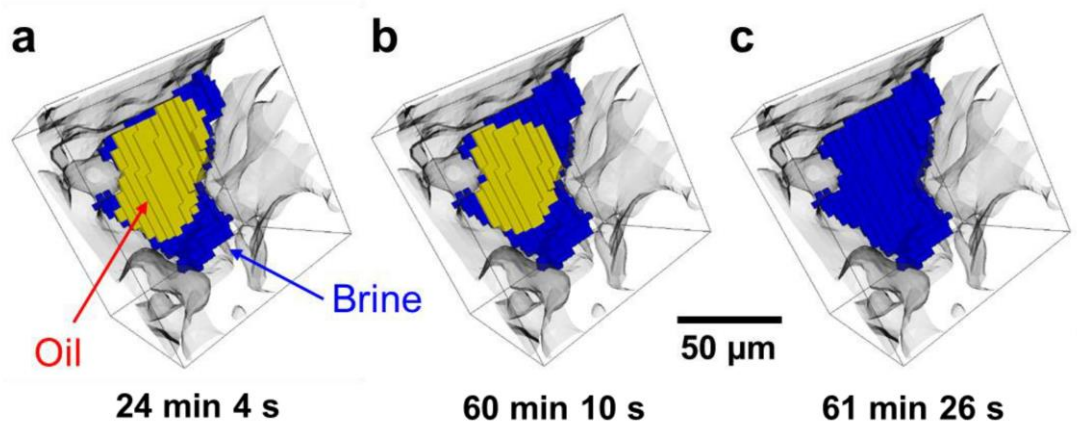

Figure 10: Swelling of the water layers leading to snapping-off the oil in a throat [39]

Singh et al (2017) observed that the snap-off events including the movement of the interfaces to disconnect the non-wetting phase takes several minutes, which is significantly slower than the Haines jumps discussed in section 2.1.1 [39]. If snap-off occurs in all of the throats surrounding a pore, this leads to trapping of the non-wetting phase by the wetting phase [32]. This event is strongly influenced by the pore-space architecture (discussed in section 2.3.2) and wettability (discussed in section 2.3.4) [14, 30, 39]. In addition, snap-off occur throughout the rock sample, while the wetting phase is still filling only the pores near to the injection end, owing to the connection between the swelling layers [39]. Rücker et al (2015) noticed that the frequency of the local snap-off during imbibition is related to the wetting saturation in the system such that it is increases with increasing the wetting phase saturation, and at high wetting phase saturation the number of snap-off events sharply increases [5].

2.1.2.2 Piston-Like Displacement

The second mechanism during imbibition is the piston-like displacement or called pore-filling mechanism [39]. TM fluid-fluid interfaces are responsible for the filling of a significant portion of the porous medium during imbibition, which is controlled by threshold entry pressures similar to the drainage process but lower P_c values [13, 39]. The process can be classified into two cases: (1) piston-like throat filling. (2) pore-filling.

Piston-like throat filling. As long as the adjacent pore to the throat is filled with the wetting phase, this filling mechanism is possible when the threshold entry pressure is met, otherwise, the only possible mechanism is snap-off inside the throat [13]. Blunt (2017) proved that providing that the adjacent pore to the throat has a wetting-phase, the piston-like throat filling always wins the competition with snap-off, reducing the global trapping in the media. The reason is that the threshold P_c required for piston-like displacement is higher than the critical P_c

required for snap-off (note: Pc decreases during imbibition) [39]. During this process, the AM interface at the corners of the throats are either receding contact angles or hinging contact angles (already swelling), which makes a difference when calculating the required local P_c pressure; more complicated for AM interfaces with hinging angles [13].

Pore-filling. After filling the throats or being initially filled with the wetting phase, to invade the pores with the wetting phase, the TM interface must fit the radius of pore (r_p) to be able to invade the centre of the pore with an advancing contact angle, see equation 7 [13]. Hence, the process depends on the radius of the pore, the pores of the smaller radius will be imbibed first since the capillary pressure is higher in the beginning of the imbibition process [13].

$$P_c = \frac{2\,\sigma\cos(\theta_A)}{r_p} \tag{7}$$

Furthermore, the process is highly dependent on the type of fluid in the adjacent throats of the pore such that how many pore-throats are filled with the wetting phase [39]. Considering a pore with four adjacent throats, as the number of adjacent throats filled with non-wetting phase increases as the radius of curvature gets larger, making the required P_c to be higher to fill the pore, and vice versa [13]. Figure 11 shows an illustration of the two cases: I1 where there is only one throat with non-wetting phase (in white) and, as a result, a smaller radius of curvature, and I2 where there are two adjacent throats with non-wetting phase, leading to a larger radius (smaller P_c or higher wetting phase pressure is required to displace the non-wetting phase) [13].

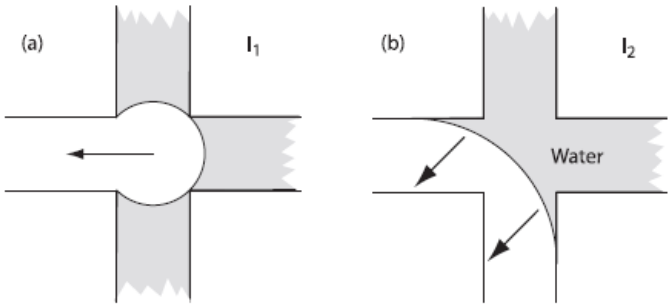

Figure 11: Effect of the adjacent throats on the pore filling mechanism [13]

2.2 Pore-Scale Descriptors

The section discusses two vital pore-scale descriptors, Euler characteristic (χ) and in-situ contact angle, utilized in recent research to investigate pore-scale multi-phase flow and trapping in porous media, and to evaluate and explain pore-scale static and dynamic processes using high spatial- and temporal-resolution micro-CT scanners. This section presents theory, definitions, equations, workflows and applications related to the two pore-scale descriptors.

However, the findings and results associated with the application of these descriptors in pore-scale trapping experiments are discussed in section 2.3.

2.2.1 3D Euler Characteristic

When a topological property of an object is not altered by continuous deformation of its shape (i.e. stretching, bending, and twisting) is called a topological invariant [4, 40]. Therefore, a topological invariant of an object changes, for example, by splitting it into smaller objects or sticking it to other objects, i.e. discontinuous deformation [4] [4, 6, 18]. Hence, a topological invariant is a solid descriptor of an object's connectivity such as the connectivity of the non-wetting phase within a porous medium. Figure 12 shows 3D visualization of non-wetting phase (i.e. oil), from experiment I1 in chapter 6, for post-drainage on the left and post-imbibition on the right of the picture. It is visually obvious that the oil connectivity changed by the wetting phase displacement of the non-wetting phase, however, there is a need to find a topological invariant to quantify the state of connectivity, as a result allowing comparisons between different experiments and states.

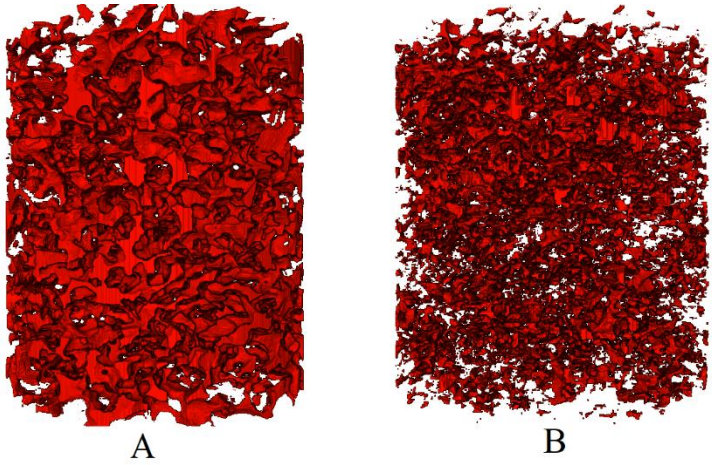

Figure 12: 3D visualization of non-wetting phase within a miniplug for A) post-drainage and B) post-imbibition

In recent years, Euler characteristic (χ), also known as Euler number, has been effectively employed in porous media from micro-CT images as a quantitative descriptor of phase connectivity in a porous material, since it is a topological invariant [4]. Phase topology (connectivity) has been related to phase saturation (initial, transient and final saturation) [4, 5, 18] and capillary trapping (represented by capillary number) [4], and relative permeability [7] by using the Euler characteristic (χ).

It is worth mentioning that Euler characteristic (χ) can also be seen as a descriptor of the possible pathways for the non-wetting phase to be mobilized through during displacement by a wetting

phase [18], used a descriptor of the connectivity of between the pores within a sample [41], as a descriptor of trapping efficacy [18], and as a predictor of relative permeability [42]. Moreover, it was used for understanding fluid flow regimes [8], and imbibition displacement events [5, 9], and it was used in the description of free energy for immiscible two-fluid flow [43].

The Euler number, which is dimensionless [6], for a non-wetting fluid phase within a porous medium is given by equation 8, which is the alternating summing of the first three elements of the family of Betti numbers β_i from homology theory [1, 4-6, 8, 18, 42].

$$\chi = \beta_0 - \beta_1 + \beta_2 \quad (8)$$

Where β_0, zeroth Betti number, is the number of isolated non-wetting fluid phase components (i.e. clusters or connected pathways at S_{wi}), β_1, first Betti number, is the number of redundant connections or loops via pore throats within the non-wetting phase components, and β_2 , second Betti number, is the number of wetting clusters/blobs or solid particles suspended in the non-wetting fluid, creating cavities or hollows within the non-wetting phase [1, 4-6, 8, 18, 42].

Betti numbers. Considering a non-wetting cluster is highly branched in multi pores via pore throats, if cutting this cluster at a specific throat does not split it into two clusters, this connection/loop via the pore throat is counted in the first Betti number (β_1) [4, 6]. Moreover, β_2 is zero for porous media experiments, since it is not possible to have a solid particle (i.e. grain) surrounded completely by the non-wetting fluid phase [4-6, 18], and the wetting fluid phase (i.e. brine) cannot be floating as droplets in a non-wetting phase such as air or carbon dioxide due to its low density [4, 18]. Even if the non-wetting phase is denser, i.e. crude oil, the second Betti number (β_2) is not worth considering compared to β_1 and β_0, as proven by the calculations in [6] and assumed in [5]. Thus, equation 1 can be reduced to equation 9 for flow experiments in a porous medium.

$$\chi = \beta_0 - \beta_1 \quad (9)$$

Examples. Figure 13 includes three clusters (A, B and C) of non-wetting phase extracted from the dataset 1 and dataset 2 used in chapter 4. Since each cluster is treated individually (a single element), the zeroth Betti number (β_o) is 1 for A, B and C. Cluster A, containing a non-wetting blob, clearly has no branching via pore-throats, making the first Betti number (β_1) to be zero, since there are no redundant connections or loops. Cluster B branches in three pores via two connections, however, the first Betti number (β_1) is also equal to zero, since making a cut in any of these connections splits the cluster into two elements (see the green dashed lines on cluster B), which violates the definition of β_1, discussed above, see figure Figure 13. Therefore,

cluster A and B, which are different in the size and shape, have the same Euler number ($\chi_A = \chi_B = 1$), according to equation 2. The first Betti number (β_1) is non-zero for cluster C, since it has redundant loops/connections where indicated by the red dashed lines, leading to a negative value for χ_C. As the number of redundant loops/connections increases as the Euler number becomes more negative, indicating a higher state of connectedness [4, 42].

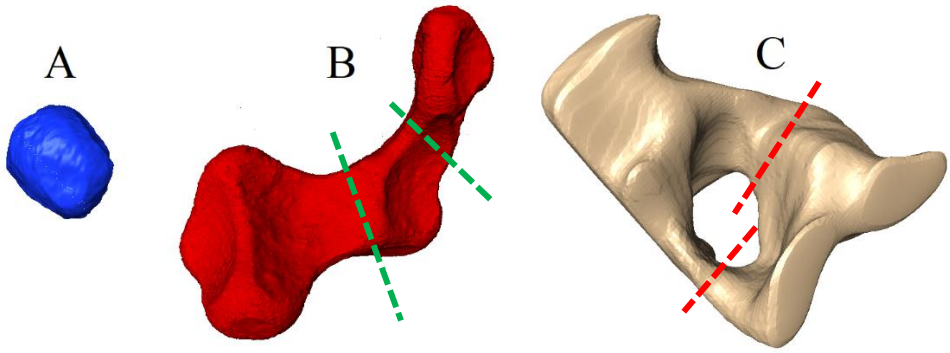

Figure 13: Three non-wetting clusters with zero, non-redundant, and redundant connections for A to C, respectively

Reporting methods. If there are 1000 clusters within a porous medium, then there are 1000 Euler numbers following the approach explained above. Fortunately, Euler characteristic is an extensive property, therefore, the sum of the 1000 numbers leads to a composite Euler number (1st method), given by equation 10, which represents the entire non-wetting volume within the porous material [4, 18]. This method of reporting the Euler number was used in experiments including a single porous material, for example the flow experiment in [5], and the aim was to continuously evaluate the non-wetting phase topology from the post-drainage state to the post-imbibition state. Moreover, this composite number can be normalized with the bulk volume of the porous material, see equation 11, to acquire an intensive quantity with units of mm^{-3} for convenience [6, 9].

However, this composite Euler number is still not appropriate to compare non-wetting phase topology between experiments of samples of different pore structure. Therefore, a decent approach is to normalize any acquired Euler number of the non-wetting phase by the Euler number of the non-wetting phase when its saturation is 100% in the porous system, see equation 12, which is equivalent to Euler number of the pore structure within the system [4, 18]. Therefore, the maximum normalized value by this approach is 1, which represents most connectedness, and indicates that the connectivity of the phase increases as the normalized number approaches 1 and vice versa [4]. When the composite Euler number of the non-wetting

phase within the sample is positive for a highly disconnected phase, the normalized value becomes less than zero [4].

$$\chi_{NW} = \sum_{i=1}^{N} \chi_i \tag{10}$$

$$\hat{\chi}_{NW} = \frac{\chi_{NW}}{V_B} \tag{11}$$

$$\hat{\chi}_{NW} = \frac{\chi_{NW}}{\chi_{100\%NW}} \tag{12}$$

Properties. Furthermore, the normalized composite Euler number of the total non-wetting phase can be classified into two $\hat{\chi}_{NW}$; one for the non-wetting ganglia and the other for the non-wetting connected pathway, which is defined as the biggest non-wetting cluster in the system [6]. The aim of this classification is to evaluate the hysteresis in topology of total non-wetting phase, non-wetting ganglia, and non-wetting connected path as a function of saturations [6]. Moreover, the Euler characteristic is a process-dependent property, for example, it depends on which phase is displacing the other (i.e. drainage or imbibition) [8] and on the injection flow rate [6]. Last but not least, the Euler characteristic of the wetting phase is an independent measurement of the non-wetting Euler number [8].

2.2.2 In Situ Contact Angle

Wettability is a key parameter for understanding subsurface processes in porous media such as hydrocarbon recovery by flooding, geological storage of carbon dioxide (CO_2), and migration of contaminants in water aquifers [3, 10, 22, 44]. Furthermore, wettability plays a critical role in multiphase flow and trapping mechanisms at pore-scale in reservoirs where the target is to recover hydrocarbon or trap carbon dioxide (CO_2), particularly by strongly affecting capillary pressures, relative permeability and fluid saturations (i.e. residual non-wetting phase saturation) [10-12, 22].

From pore-scale perspective, wettability is defined as the relative tendency of one of two or more immiscible fluids to adhere to, spread on or wet the grain surfaces within a porous medium, depending on the chemical nature and spread ability of the fluids, physical and chemical nature of the grain surfaces (controlling preferentiality), and pore-scale complex physical and chemical interactions between the rock and fluids [10, 11, 28, 45-50].

Wettability can be quantitatively evaluated by measuring a contact angle between the fluid-fluid interface and the fluid-solid interface at the three-phase contact point, and then following specific criteria leads to an indication of the system's state of wettability [28]. Figure 14

demonstrates the measurement of a contact angle through the denser phase (i.e. water) to indicate the wettability condition (i.e. preferential wetting of the solid by the denser phase) [28, 51]. However, the range of each wettability condition is different in literature, particularly for the neutral wet state, see Table 1 for cut-off criteria for the wettability states as stated by three well-known studies [52-54].

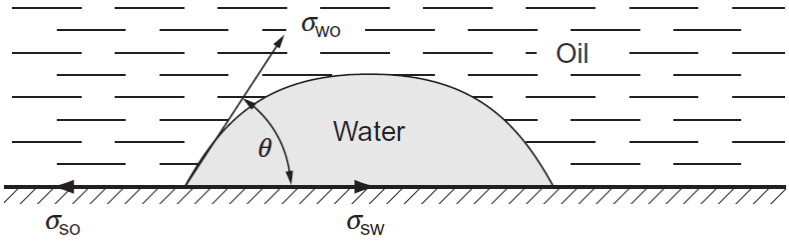

Figure 14: Contact angle measured through denser phase and Young equation parameters [51]

The conventional approaches to measure contact angles, such as using sessile drop method, modified sessile drop method, and Wilhelmy plate technique, severely fail to mimic the factors and conditions controlling wettability at pore-scale in a real natural porous material [28, 55]. To explain, the experiments using these approaches perform the tests on solid surfaces that are ideal (smooth, flat and chemically homogenous), leading to non-representative contact angle to account for roughness, curvature and mineral heterogeneity at micro-scale, respectively [12]. This single contact angle measured in ideal conditions cannot be representative for the random micro-distribution of contact angles within the rock [56]. Fortunately, imaging techniques have influentially reshaped research styles in geoscience applications, particularly high-resolution imaging techniques such as X-ray micro-computed tomography (micro-CT) [57, 58].

Table 1: Cut-off criteria for wettability states as found by three different studies [52-54].

Source	Wettability state	Contact angle
Trieber et al. (1972)	water-wet	0º to 75º
	Neutral-wet	75º to 105º
	Oil-wet	105º to 180º
Morrow et al. (1976)	water-wet	0º to 62º
	Neutral-wet	62º to 133º
	Oil-wet	133º to 180º
Chilingar and Yen (1983)	Strongly water-wet	0º to 20º
	Water-wet	20º to 80º
	Neutral-wet	80º to 100º
	Oil-wet	100º to 160º
	Strongly oil-wet	160º to 180º

In recent years, there has been a tremendous interest in exploring and building protocols for measuring in-situ contact angles from micro-CT images for static [12, 22, 59] and dynamic experiments [2, 11], natural rock samples [2, 11, 12, 59] and glass beads [22], and two-phase

and three-phase experiments [11]. In literature, there is a manual method [2, 11, 12, 22] and three automatic algorithms [20, 21, 30] to measure in-situ contact angles from micro-CT images. Moreover, there are several applications for the extracted contact angles at pore-scale, starting from indicating the wettability of the system to explaining the displacement events at pore-scale [2, 11, 12, 20-22, 30, 59].

Manual method. On gray-scale or segmented micro-CT images, the in-situ contact angle can be manually determined by following several manual and semi-automatic steps to obtain a plane including a three-phase contact point, fluid-fluid interface, and fluid-solid interface, where the contact angle is manually measured by the user [12, 22, 30]. Therefore, it is a single-measurement method, user-subjective and time consuming, knowing that a miniature rock sample has hundreds of thousands of contact points [21, 59].

Andrew et al. (2014) was the first to establish the protocols for measuring in-situ contact angles from micro-CT images for a supercritical CO_2–brine–carbonate system [12]. This work performed the manual approach at 300 three-phase contact points within a carbonate mini-plug, concluding that the mean local contact angle was $45° \pm 6°$, i.e. weakly water-wet system. Lv et al (2016) showed the success of this pore-scale approach by a comparison with the contact angles measured by sessile drop method [22].

This valuable work inspired other researchers to design experiments at pore-scale to investigate in-situ wettability by applying this method. This approach was utilized to explore the impact of wettability alteration by fatty acid on the morphologies of residual oil (i.e. formation of non-wetting layers vs. formation of clusters/ganglia) in a quarry calcite [60], to determine the contact-angle hysteresis (receding and advancing contact angles) for dynamic experiments to evaluate trapping under different wettability states (water-wet vs. mixed-wet) [2] and to explain pore-scale displacement mechanisms during imbibition and drainage for two-phase and three-phase flow [11].

The manual approach starts with deciding on which ganglion/globule to be extracted as a subvolume from the segmented micro-CT images [2, 11, 12, 61], see Figure 15 showing the extraction of a non-wetting phase globule (in red) which is trapped by the wetting phase (in blue) with the porous rock (in gray) [11]. After that, the subvolume, on the right side of Figure 15, is processed by an interface labelling filter, such as the 3D Sobel filter, to find the three-phase contact lines (made of points called triple points) within the subvolume [2, 11, 12, 61].

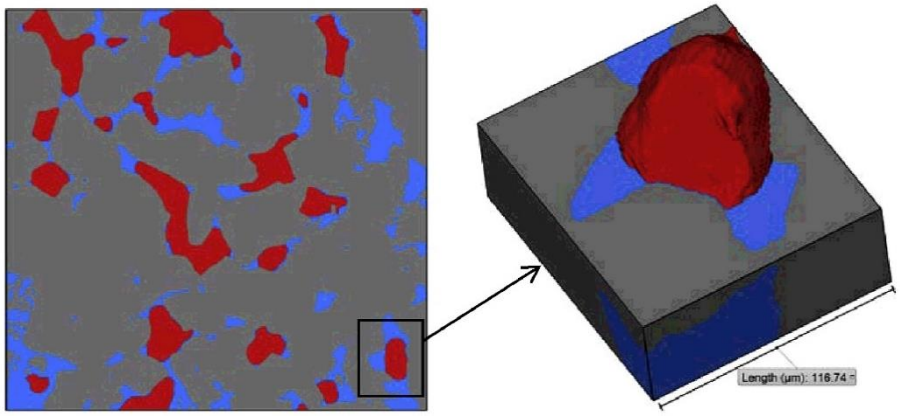

Figure 15: Trapped non-wetting phase globule within a porous media [11]

Figure 16 demonstrates a trapped non-wetting globule labelled with the three-phase contact lines (in yellow) [11]. The next step is to choose a triple point of interest on the three-phase contact line where the contact angle is measured [2, 11, 12, 61], for example point A in Figure 16. After that, the data of this subvolume is processed using a resampling filter to create a plane including the triple point, i.e. point A, such that the plane has a normal vector at point A, which is parallel to the contact line including point A, making the plane perpendicular to the contact line [2, 11, 12, 61], see Figure 17(a). Figure 17(b) shows the final step which is to construct two interfacial tangents on the resamples plane X to measure the contact angle at point A [11].

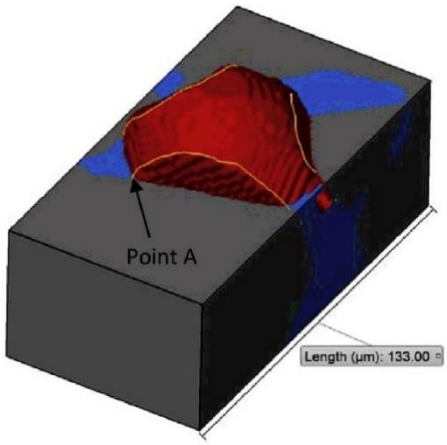

Figure 16: A trapped non-wetting globule labelled with the three-phase contact lines (in yellow) [11]

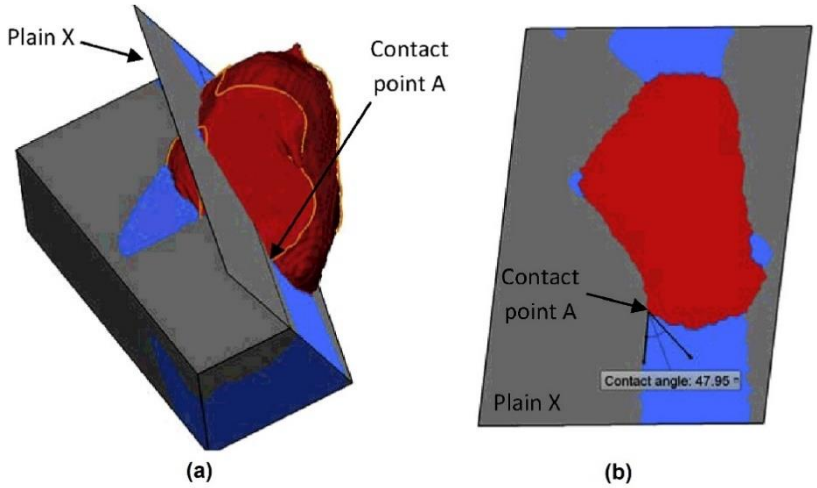

Figure 17: Plane X perpendicular to the contact line in (a) and measuring the contract angle in (b) [11]

Automatic methods. There has been also an interest to develop automated methods to extract as much wettability parameters as possible from a porous medium, to exclude the user subjectivity, and to make the process time-saving [20, 21, 30]. Moreover, it will significantly improve the simulation of flow and trapping in porous media which is vital for the assessment of the geological storage of CO_2 and recovery schemes for hydrocarbon reservoirs, since the pore-network models will not be assigned a uniform state of wettability [14, 21, 30, 62, 63].

In literature, to the best of our knowledge, there are only three works in the field of developing algorithms for contact angle estimation [20, 21, 30]. Klise et al. (2016) developed an automated method to find the two-phase and three-phase boundaries in micro-CT images (which are interfaces in 2D, see Figure 18) and three-phase contact lines (contact points in 2D, see Figure 18), and then a volumetric-search function (gray circle in 2D, see Figure 18) defines solid-fluid and fluid-fluid interfaces for every point on the three-phase contact line, gray circle in 2D [20]. Next, the algorithm estimates the contact angle with equation 13 [20].

$$\theta_c = \pi - \cos^{-1}(n_{fluid/fluid} \cdot n_{solid/fluid}) \quad (13)$$

Where $n_{fluid/fluid}$ is the normal vector to the fluid-fluid interface, i.e. kerosene/brine interface in Figure 18, and $n_{solid/fluid}$ is the normal vector to the solid/fluid interface, i.e. glass/brine interface in Figure 18.

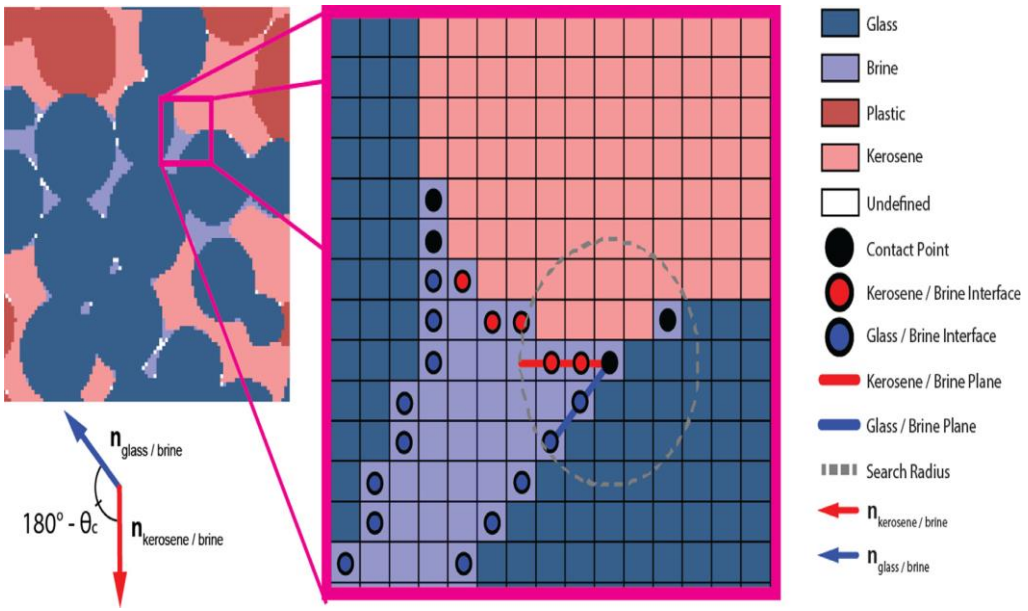

Figure 18: Klise et al. (2016) method to estimate contact angles in kerosene-brine-glass system [20].

Scanziani et al. (2017) automatized the aforementioned manual method such that the algorithm will find the normal plane for the three-phase contact point, and after estimating the contact angle, it moves to next point [30]. However, the method does not use normal vectors to the interfaces to estimate the contact angle via equation 9, similar to Klise et al. (2016) method. Figure 19 demonstrates their approach which is to fit a circle (in white) to the fluid-fluid interface (fluids are in green and blue), smooth the solid surface (in gray) by linear regression (in black), and then construct a tangent (in yellow) to the circle at the contact point. It is worth mentioning that fitting a circle to the fluid-fluid interfaces is limited for a constant curvature of the fluid–fluid interface when the system is at equilibrium [30]. This equilibrium state is defined by the Young-Laplace equation.

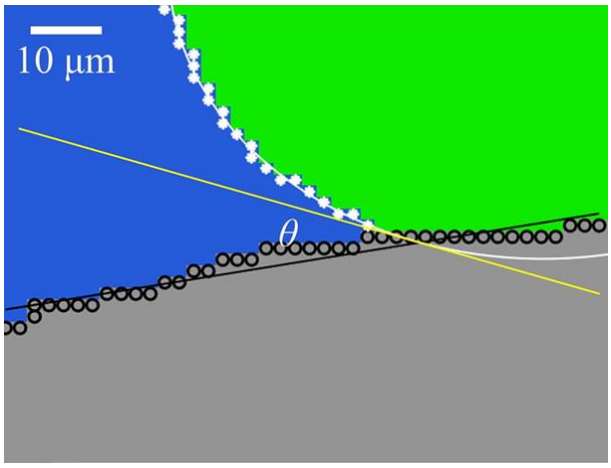

Figure 19: Scanziani et al. (2017) method to estimate in-situ contact angles by fitting a circle [30]

Presented work by Klise et al. (2016) and Scanziani et al. (2017) suffers from a main limitation which is they are strongly dependent on the fluid-fluid and fluid-solid interfaces which are not accurately acquired by micro-CT images, particularly for natural rocks exhibiting high complexity in roughness, pore-geometry, and curvatures [21, 30]. Klise et al. (2016) reported that a significant fraction of the total triple-contact points were not valid in the estimation, although the program was applied on uniform glass/plastic beads, and also their sensitivity analysis showed that the imaging resolution has a high impact on the results following this approach [20].

Scanziani et al. (2017) confirmed that a higher resolution would increase the accuracy of the obtained results and showed that his algorithm underestimated the mean contact angle by 4.8^{o} to 9.5^{o} degrees in Ketton–brine–decane system [30]. In addition, since Scanziani et al. (2017) algorithm requires the system to be at equilibrium, it cannot be applied to dynamic experiments where contact angle hysteresis is estimated at pore-scale, similar to what has been done manually in [2] and [11].

AlRatrout et al. (2017) presented an automated approach reducing the dependency on the resolution by subjecting the system to smoothing the surfaces of the boundaries where the phases contact, with maintaining two parameters constant: (1) the volume of the fluids with the system, and (2) the locations of the three-phase contact lines [21]. This method also considers only systems at equilibrium following the approach by Scanziani et al. (2017), which enables justifying their use of the smoothing approach of the fluid-fluid surfaces (interfaces in 2D) [21].

In addition, they use the Young-Laplace equation to estimate the contact angle, similar to the approach by Klise et al. (2016) [21]. Figure 20 (Note b, d and f are for a subvolume of a trapped oil ganglion located in the black circles in a, c, and e, respectively) shows the workflow of this smoothing-based approach to estimate in-situ contact angles from segmented micro-CT images, which has four steps: extracting contact surfaces between the phases, smoothing these surfaces, extracting the contact lines, and finally applying equation 13 at every contact point [59].

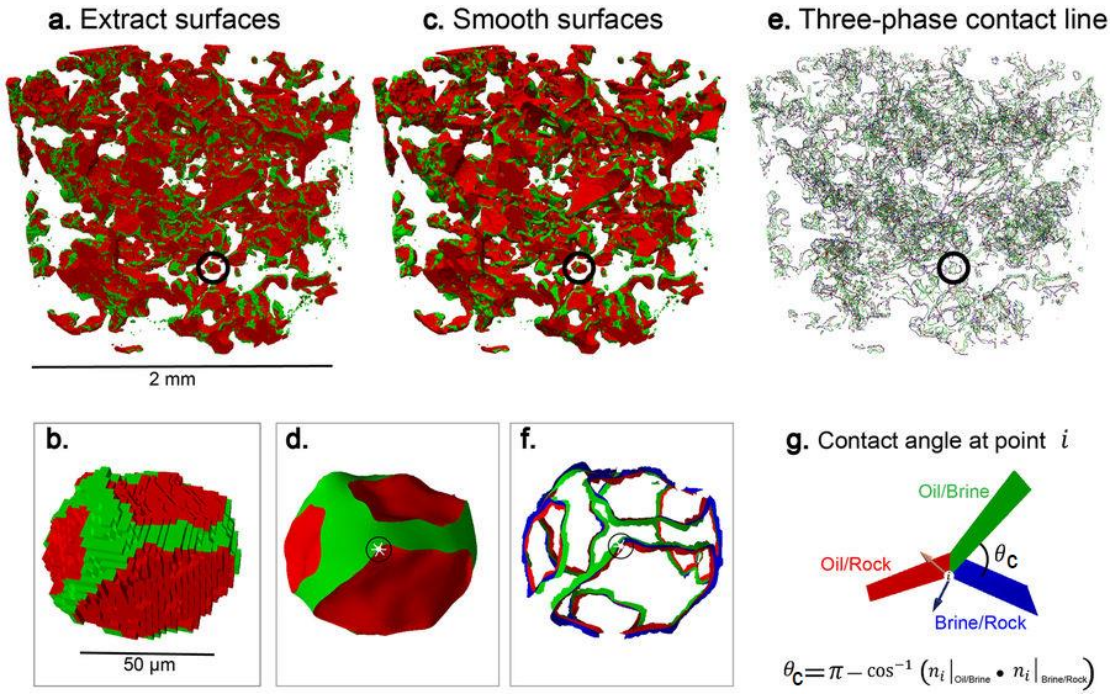

Figure 20: AlRatrout et al. (2017) automatic method applied on micro-CT segmented images [59]

Automated methods significantly helped to connect the application of in-situ wettability characterization to flow and trapping studies in natural porous media. AlRatrout et al. (2017) approach was applied on pore-scale studies to investigate the effect of mixed-wettability states created by local wettability alteration via ageing on oil recoveries through estimating tremendous number of contact angles (between 0.5 to 1.4 million angles depending on the sample) [59]. In addition, it was also applied on limestone samples to correlate local wettability to surface roughness and interfacial curvature [15, 63].

2.3 Trapping in Porous Media

The trapping of the non-wetting phase is a favourable process for geologic carbon dioxide storage and a process that should be minimized for hydrocarbon recovery [4]. This section investigates four factors controlling the trapping of the non-wetting phase, specifically; capillary number (C_a), initial topology of the non-wetting phase, porous media architecture, and wetting conditions.

2.3.1 Capillary Number (C_a)

Capillary trapping of the non-wetting phase is a significant pore-scale mechanism for hydrocarbon recovery and geological storage of CO_2 [2-4, 18, 64]. It is engineered by changing injected fluid properties and flow conditions such as temperature, pressure, flow rate, and salinity [2, 4]. Capillary number (C_a) is related to the amount of residual non-wetting phase by

capillary trapping, and C_a is a function of invading phase velocity (υ_{INV}), invading phase viscosity (μ_{INV}) and interfacial tension (σ), see equation 14 [4, 65]. The invading velocity is given by equation 15 where: Q is the flow rate, A is the cross-sectional area of the porous sample, and ϕ is the porosity [4, 65].

$$C_a = \frac{\upsilon_{INV} \cdot \mu_{INV}}{\sigma} \tag{14}$$

$$\upsilon_{INV} = \frac{Q}{A\phi} \tag{15}$$

The C_a number combines viscous forces ($\upsilon_{INV} \cdot \mu_{INV}$; numerator of equation 5) and capillary forces (σ; denominator of equation 5) which is unique for two-phase flow compared to a single phase flow [65]. If C_a increases by increasing the numerator or decreasing the denominator in equation 5, the non-wetting trapping i.e. residual non-wetting phase reduces in the porous medium [2, 65, 66]. In other words, as the flow transit from being capillary force to viscous force dominated, as less of the non-wetting phase is trapped within the porous medium [4]. Moreover, during this transition, at a specific value of C_a, which is called the critical C_a, the rate of decline in the amount of trapped non-wetting phase will start to be faster compared to C_a values less than $Ca_{critical}$ [4, 66]. In literature, pore-scale studies can be classified into two types with respect to capillary numbers (C_a): a single-C_a imbibition experiments and multi-C_a imbibition experiments.

A single-C_a experiment is used when the aim of the experiment is to keep the parameters involved in the C_a constant (effect of interfacial tension, flow rate and viscosity is not examined) for an imbibition test on a specific sample for applications such as to perform non-wetting phase cluster analysis [19], to evaluate in-situ wettability [12], to estimate interfacial curvature [15, 63], and to examine pore-scale dynamics [5, 9].

Furthermore, there are studies conducting several experiments of different C_a numbers to investigate the effect of the capillary number parameters on trapping [2, 4, 18, 67]. Such experiments can be on different samples and then the results can be normalized for comparisons [4, 18], or on a single sample by drainage-imbibition cycling where all drainage processes should be of the same flow-rate and injected pore volumes to guarantee generating the same initial water saturation in the sample [2].

The flow regime can be either capillary-dominated or viscous-dominated [2, 4, 13], which depends on the purpose of the experiment, and can be controlled by increasing the flow rate [2], increasing the viscosity [67], or reducing the interfacial tension between the fluids [68].

Moreover, if the capillary number for the experiment is adequately high (viscous-dominated flow), it can lead to a dynamic flow regime which is a flow regime significantly reducing the amount of trapped non-wetting phase by both mobilization mechanism and changing the order of pore-scale displacement/filling events such snap-off, piston-like advance and cooperative pore filling [2, 4, 13, 69].

Experimental findings. Herring et al (2013) stated that capillary trapping of carbon dioxide CO_2 considerably depends on the capillary number C_a of the imbibition process, such that the trapping decreased with increasing the capillary number [4]. Khishvand et al (2016) performed three micro-scale flooding experiments on Bentheimer sandstone to examine the effect of the capillary number on non-wetting trapping by varying only the injection flow rate and found that the residual non-wetting phase saturation and the size of the trapped ganglia decreased at higher capillary numbers [2]. Heshmati and Piri (2018) showed that increasing the capillary numbers led to a higher production of the non-wetting phase, but showed that considerably high flow rates such that corresponding to viscous-dominated flow regimes, there was no significant difference in the non-wetting phase recovery, but considerably on the non-wetting phase size distributions [70].

It is important to emphasize that C_a is not the only controller of the amount of trapped non-wetting phase since other factors such as the initial non-wetting phase topology [4, 18] and porous media shape and structure, discussed in section 2.3.2 and 2.3.3, respectively.

2.3.2 Initial Non-Wetting Phase Topology

The use of X-ray microtomography to explore the topology of the non-wetting fluid in a porous material prior to the imbibition process has helped significantly to establish a relationship between the pre-imbibition state of non-wetting phase connectivity and the trapped residual non-wetting phase with the porous medium [4]. In other words, it is related to how much CO_2 can be stored in the porous system for environmental applications and how much oil can be recovered from the reservoir for petroleum engineering applications [4, 18, 19].

On field-scale CO_2 storage application, the supercritical CO_2 drainage process is engineered, therefore, it is important to evaluate this relationship [4, 18]. On the other hand, the relationship is not as significant for field-scale hydrocarbon recovery since the oil migration from a source rock over millions of years is a natural phenomenon [13]. However, the primary drainage with oil in pore-scale experiments is engineered, then the initial topology of the non-wetting phase

becomes important for accurate comparisons between different recovery schemes i.e. imbibition by different capillary numbers or different salinities.

Experimental findings. Wardlaw and Yu (1988) performed displacement experiments in glass micromodels and concluded that there is a relationship between the non-wetting topology initial and final state of an imbibition process [34]. As discussed in section 3.3, Euler Characteristic (χ) is the descriptor of phase connectivity (topology) within a porous media. Herring et al (2013) was the first to apply this descriptor on 3D micro-CT images to investigate how the initial non-wetting topology affects the displacement/trapping efficiency [4]. Herring et al (2013) found that capillary trapping depends on the initial non-wetting connectivity, and that it is an inversely proportional relationship in Bentheimer sandstone, see Figure 21 [4]. Figure 21 has total non-wetting trapping (residual non-wetting saturation divided by initial non-wetting saturation; SR/SI) on the y-axis and normalized Euler Characteristic (most connectedness is given by a value of 1) by equation 12 in section 2.2.1.

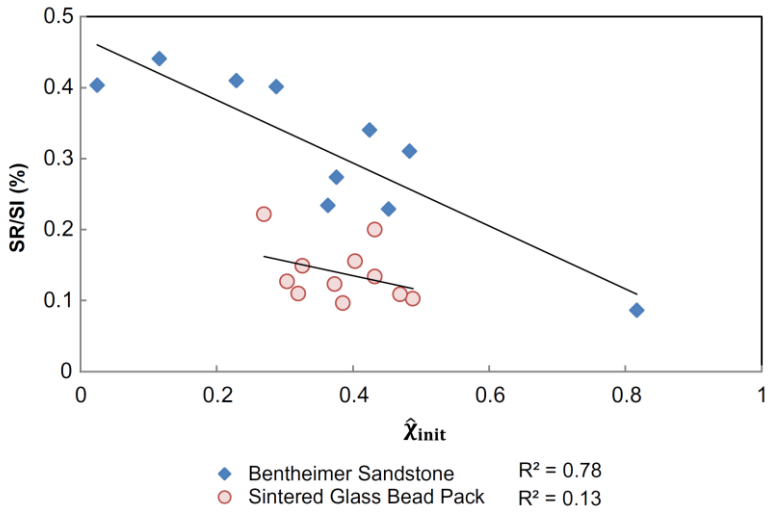

Figure 21: Total non-wetting trapping (SR/SI) verses normalized Euler Characteristic [4]

2.3.3 Pore-Space Architecture

The amount of non-wetting phase trapped in a porous medium is strongly associated with the geometry and structure of the pore-space [13, 32, 34]. Snap-off during an imbibition process is a significant mechanism responsible for trapping non-wetting phase via swelling of wetting layers residing in crevices and corners of the throats [13], discussed in section 2.1.2. Figure 5 shows an example of snap-off for a non-wetting phase using micro-CT images at pore-scale.

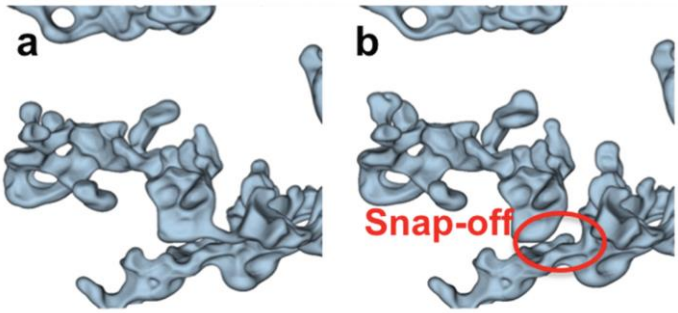

Figure 22: Snap-off event during imbibition in a borosilicate glass sample [7]

It was found that this mechanism depends on the ratio of the diameter of the pore element to the diameter of the throat element, which is called in literature "pore body-throat aspect ratios", [13, 32], see equation 16, where *a* is the aspect ratio and *D* is the diameter of the pore or throat. The possibility of the non-wetting phase to be trapped in a pore increases as the aspect ratio increases [71], i.e. generally greater than unity [32]. However, Blunt (2017) states that for a network model with elements (pores and throats) assumed to be circular, the aspect ratio has to be greater than 2 for snap-off to occur [13].

$$a = \frac{D_{pore}}{D_{throat}} \tag{16}$$

$$a = \frac{D_{pore}}{\sum_1^i D_{throat_i}} \tag{17}$$

In addition, a pore usually is connected/bounded by several throats, which arise the question how to calculate the aspect ratio to know whether snap-off is favoured or not. Blunt (2017) mentions that for this case the aspect ratio is calculated using the mean of the surrounding throat diameters [13], see equation 17, where *i* is the number of bounding throats. For the whole porous sample, it can be assigned also average aspect ratio [13]. For example, micro-CT images of Leopard, Berea and Bentheimer samples showed an average aspect ratio of 5.5, 4.3 and 4.4, respectively [32].

For example, Herring et al (2018) used micro-CT images of Leopard, Berea and Bentheimer samples to find the average aspect ratio of 5.5, 4.3 and 4.4, respectively [32]. It was also found that the trapping efficiency (residual non-wetting saturation divided by initial non-wetting saturation; $S_{R,\,NW}/S_{I,\,NW}$) in Leopard with a = 5.5 to be higher by 25% compared to the other two rocks, see Figure 23. A simulation study by Mahmud and Nguyen (2006) found that small aspect ratios reduced the local snap-off event within the simulated pore-network, leading to higher displacement efficiency of the non-wetting phase i.e. lower residual trapping [71]. Since

glass beads exhibit small aspect ratios [8], the trapping efficiency is expected to be very low to represent the non-wetting phase trapping in natural rocks.

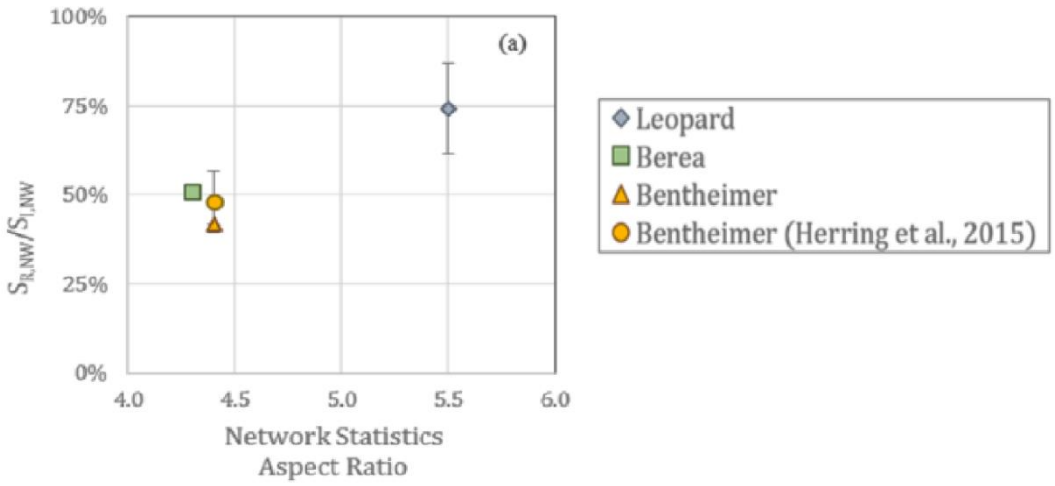

Figure 23: Trapping efficiency as a function of aspect ratio [32].

It is worth mentioning that filling of the bounding throats of a pore starts from the smallest to the largest throat [13]. Therefore, the largest throat, connected to a pore is significant to the trapping process by snap-off, such that if this throat is adequately large, the non-wetting phase can be displaced through it by the wetting phase, leading to trapping failure [13].

Another aspect to consider is the effect of the number of throats connected to a pore, which is called "pore coordination number" [32]. It was found that as this number increases as the possibility of non-wetting trapping increases [33]. Herring et al (2018) found that although this number is important for trapping by snap-off, it is not sufficient to predict the amount of non-wetting trapping [32]. In addition, since this number refers to the number of throats connected to the pore-body, then it can also give an indication of the connectivity of the pore-space structure [19].

2.3.4 Wetting Conditions

In-situ wettability described by contact angles at pore-scale is highly significant for the non-wetting phase trapping process for hydrocarbon recovery and CO_2 storage [11, 30, 45, 59, 60, 62, 64]. Section 2.2.1 presented that the AM interface of the swelling layers during possible snap-off events shows a change in contact angles from receding to advancing contact angles through hinging contact angles. Therefore, the contact angles are significant for the probability of the snap-off mechanism to occur in the narrow regions of a pore-throat [13]. Blunt (2017) presented that network statistics for throat snap-off in Berea sandstone to be less by 10% by

changing the contact angle range form (30^o to 60^o) to (60^o to 90^o) [13]. Therefore, the number of isolated ganglia by snap-off is less in weakly water-wet and intermediate-wet systems.

Alhammadi et al (2017) measured the in-situ contact angles in three mixed-wet samples and concluded that most water-wet sample (mean contact angle is 77^o and oil recovery is 67.1%) had the residual oil trapped as ganglia while the intermediate-wet sample (mean contact angle is 94^o and oil recovery is 84.0%) had the residual oil confined to small pores with oil-wet surfaces, see Figure 24 [59]. Therefore, it is important to consider the in-situ wettability state of the rock when trapping is investigated, particularly for simulation modelling of two-phase flow. The old approach of assigning a single uniform contact angle for the pore elements is not enough for accurate match with experimental data, but the pores should be assigned well-representative contact angles of every single pore which is dependent on the dynamic contact angles [11, 13, 14, 72].

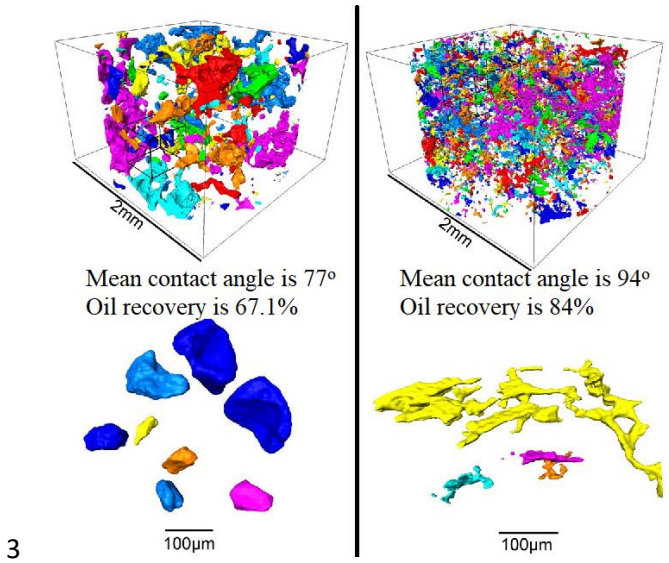

Figure 24: Effect of in-situ wettability on the snap-off by trapping as isolated ganglia [59]

Chapter 3

Nano-Technology for Enhanced Oil Recovery

Enhanced oil recovery (EOR) is a recovery stage to increase the microscopic displacement and volumetric sweep efficiency of the oil to reduce the residual oil in place via several methods such as chemical flooding [25, 26]. Nanotechnology applications have received lots of attention in the oil industry, particularly because of its significant potential for enhanced oil recovery as a new method [25-27]. In addition, it is also considered as a potential improver of the conventional EOR techniques such as polymer (chemical) EOR [25-27]. The available nanoparticles for EOR are with dimensions in the range from 1 nanometre to 100 nanometres [25, 27]. Furthermore, nanoparticles (NPs) for EOR can be classified into three types: metal oxide (e.g. aluminium oxide (Al_2O_3) NPs), organic (e.g. cellulose NPs) and inorganic nanoparticles (e.g. silica (SiO_2) NPs) [27].

Owing to the small size of nanoparticles, they have large surface area per unit volume which is an important property [25, 26]. In addition, a key feature of nanoparticles is that their functionality can be modified to change the reservoir properties controlling the fluid flow and trapping in porous media [25, 27]. EOR fluids with NPs increase the oil recovery mainly via wettability alteration and interfacial tension reduction, and possibly via reduction in oil viscosity and reservoir permeability alteration [25, 27]. It is worth mentioning that most of the available research has investigated NPs for EOR using conventional core flooding and 2D glass micromodels. To the best of our knowledge, there are only two studies ([73] and [74]) that utilized X-ray microtomography to investigate nanotechnology for EOR.

This chapter explores two main mechanisms responsible for the increased oil recovery by NPs: reduction in wettability alteration and interfacial tension. Secondly, it presents the findings on nanotechnology for EOR via the use of X-ray microtomography.

3.1 Wettability Alteration

As discussed before, pore-scale wetting conditions of a porous medium plays a considerable role in fluids flow and trapping. The presence of NPs at the fluid-solid interfaces leads to a change of the solid surface wettability [25]. For example, treatment (fully saturating the sample with nanofluid and then drying it) of neutral and oil-wet Berea sandstone cores with hydrophilic silica NPs altered the wettability (quantified by Amott index) to be more water-wet [75, 76]. Li

et al (2015) reported that the presence of crude oil in Berea sandstone cores decreased the capability of nanoparticles to alter the system wettability [77].

In addition, it was found that the wettability (described by contact angle measured on a smooth oil-wet glass surface) shifted towards water-wet state as the concentration of NPs increased [75]. However, Maghzi et al (2012) used a glass micromodel aged with heavy crude oil for 20 days to be oil-wet, see Figure 25, and observed that silica NPs altered the wettability of the glass to water-wet, see Figure 26 [26, 78]. Another study used strongly water-wet glass micromodel and observed that the contact angles increased after flooding the system with nanofluid, indicating that the wettability alteration towards a neutral-wet state [79]. It seems that the direction of change in the solid wettability is not consistent, and it depends on factors such as the initial state of wettability and wetting condition of the NPs [79, 80].

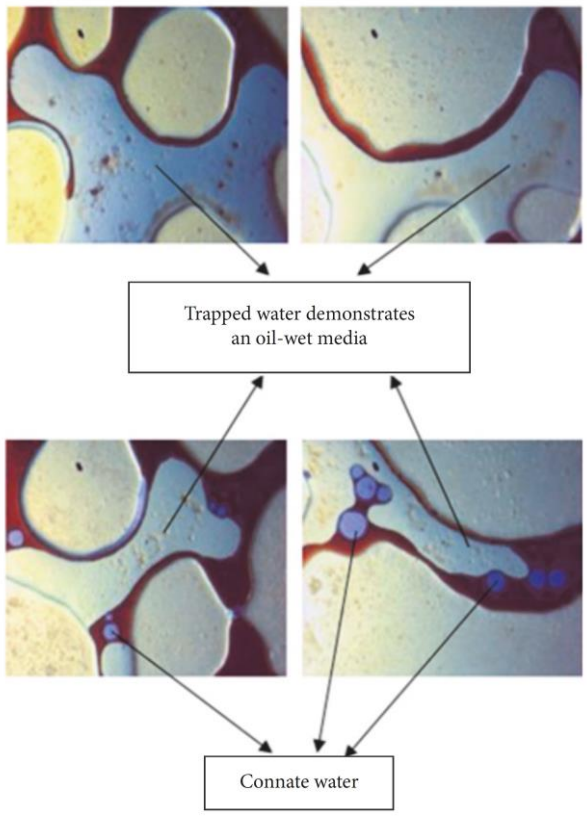

Figure 25: Pore-scale visualization of oil-wet glass micromodel after water flooding [26]

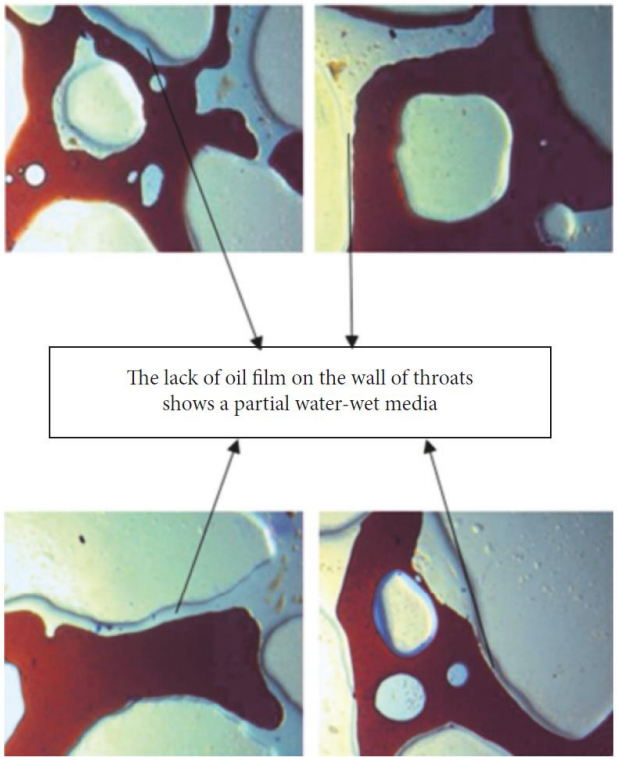

Figure 26: Change of the initial glass wettability from oil-wet to water-wet due to NPs injection [26]

It is important to understand the mechanisms responsible for altering the rock wettability by nanofluids. Layering of nanoparticles in a small region near to three-phase contact boundary (point in 2D) was investigated in literature to be one of these mechanisms, resulting in a force known as structural disjoining pressure.

3.1.1 Structural Disjoining Pressure

Structural disjointing pressure is considered to be a mechanism contributing to the rock wettability alteration when NPs are introduced to a porous system [73]. Wasan and Nikolov (2003) were the first to present the nanoparticle structuring phenomenon leading to a force normal to the fluid-fluid or fluid-solid interface, called structural disjointing pressure [81]. Consider an oil drop on solid surface surrounded by a nanofluid, see Figure 27, the small region near to the three-phase contact point is called a wedge film region (the small magnified region on the left) and the region far from the contact point (contact line in 3D) in the nanofluid phase is called the bulk meniscus region [73, 81]. In the wedge region, the nanofluid exists as a film consisting of NP layers, which creates a tension gradient increasing in the direction towards the three-phase contact point, as shown in Figure 27, resulting in a higher normal force on the oil-solid interface (i.e. at the tip of the wedge region) [73, 81, 82]. Two events occur due to this

phenomenon: (1) Detaching the oil phase from the solid and (2) progressive spreading of the nanofluid film on the solid surface [73].

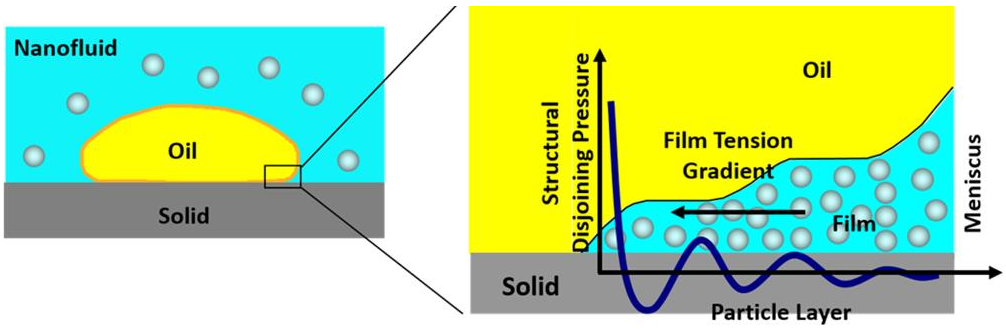

Figure 27: Nanoparticle structuring phenomenon leading to a force normal to the interface [73]

It is obvious that the higher structural disjointing pressure preferable for higher recovery by reducing the surfaces wetted by the oil phase. There are several factors controlling the amount of structural disjointing pressure such as capillary number, contact angle, salinity and NPs size, concentration and wettability [26, 73, 82-84].

Zhang et al (2016) concluded that at high capillary numbers (C_a), the contribution of this mechanism is lower due to fast displacement events, not giving adequate time for structural disjoining pressure to detach the oil phase [73]. Furthermore, they also excluded interfacial tension effect on oil recovery by using a nanofluid and non-nanofluid of the same interfacial tension, and they quantified the structural disjoining pressure induced oil recovery to be 12.6% at $C_a = 10^{-7}$ [73]. Zhang et al (2016) mentioned that the rate of these two events reduces as the salinity of the fluid system increases [73]. However, nanofluids with high osmotic pressure, small size NPs, and low polydispersity NPs have the ability to function well at high salinity as experimentally proven by Zhang et al (2014) [85].

Kondiparty et al (2011) showed that a larger size of the nanoparticles leads to a lower magnitude of the structural disjoining pressure [82]. In a system with a small contact angle is preferred since it provide a larger distance for structural disjoining pressure to act on the interface [82]. Kondiparty et al (2012) experimentally showed that the rate of the two resulting events from nanoparticle structuring (spreading of the nanofilm and detaching the oil phase from the solid surface) increases at higher concertation of NPs [83]. Moreover, the wettability of the NPs (hydrophilic NPs or hydrophobic NPs) is important, for example, hydrophobic NPs prefer to be around the oil-nanofluid interface, which makes the concertation of the NPs in the layering zone less, resulting in a lower structural disjoining pressure [84].

3.2 Interfacial Tension

The interfacial tension plays a vital role in the capillary trapping of the non-wetting phase, since IFT contributes to the value of the capillary pressure (P_c) and capillary number (C_a) as discussed in Chapter 1. A lower interfacial tension (IFT) increases the capillary number and decreases the capillary pressure, resulting in higher oil recovery i.e. lower residual oil saturation.

The interfacial tension (IFT) between oil and nanofluid is lower than IFT between oil and brine [80, 86]. In addition, the reduction in IFT increases as the NPs concentration increases, however, the reduction can still be observed in very low concertation nanofluids [26, 80, 86]. In addition, the type of NPs determines the magnitude of IFT reduction and presence of surfactant in the nanofluid has also an effect on the IFT reduction [26, 87]. Kamal et al (2017) gathered IFT data from 7 studies showing the effect of NPs type, concentration and surfactant concertation on the IFT reduction, see Table 2 [26]. It is worth mentioning that at high concentration of NPs, the rate of reduction of IFT declines as experimentally shown in [74, 76], see Figure 28. The reduction in IFT by nanoparticles is caused by the adsorption of the nanoparticles to the fluid-fluid interface, having a surfactant-like behaviour [74, 87].

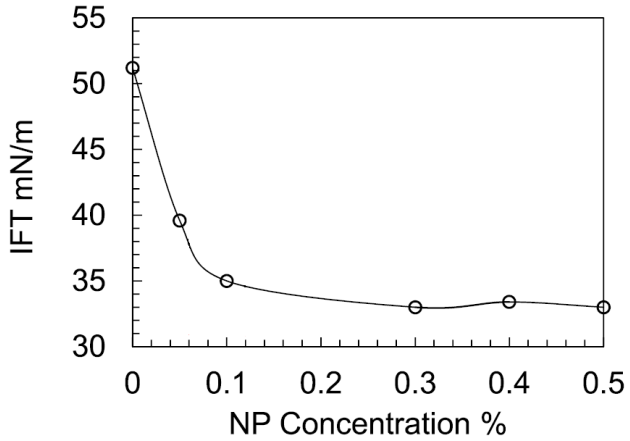

Figure 28: IFT reduction as a function of silica NPs concentration [74]

Table 2: IFT data with and without NPs for different NPs types and concentrations [26]

Entry#	NPs	NPs conc. (wt%)	Dispersion media	Surfactant conc. (wt%)	IFT without NPs (mN/m)	IFT with NPs (mN/m)
(1)	SiO_2	0.3	Propanol	0	38.5	1.45
(2)	SiO_2	0.1	Water	0	13.62	10.69
(3)	SiO_2	0.1	Ethanol	0	25	5
(4)	SiO_2	0.05	Brine	0	19.2	16.9
(5)	SiO_2	0	Brine	0.5	21.7	4.2
(6)	SiO_2	0.1	Brine	0.5	21.7	4.5
(7)	SiO_2	0.5	Brine	0.5	21.7	5.2
(8)	SiO_2	1.0	Brine	0.5	21.7	5.8
(9)	SiO_2	1.5	Brine	0.5	21.7	6.1
(10)	SiO_2	2.0	Brine	0.5	21.7	6.3
(11)	Al_2O_3	0.3	Propanol	0	38.5	2.25
(12)	Fe_2O_3	0.3	Propanol	0	38.5	2.75
(13)	ZrO_2	0.01	Water	0.2	16	3.1
(14)	ZrO_2	0.01	Water	0.3	18.4	5.4
(15)	ZrO_2	0.001	Water	0	51.4	37.2
(16)	ZrO_2	0.01	Water	0	51.4	37.2
(17)	ZrO_2	0.1	Water	0	51.4	36.8

3.3 Pore-Scale Studies via Micro-CT

To the best of our knowledge, Pak et al (2018) and Zhang et al (2016) are the only two studies using X-ray microtomography to explore nanotechnology for oil recovery [73, 74]. This section summarizes the findings of these interesting studies.

Pak et al (2018). They performed a secondary recovery by waterflooding on a carbonate sample with oil saturation of 78.28%, then the sample was flooded with a 0.06 wt% silica-based nanofluid, and finally flooded with a 0.12 wt% silica-based nanofluid [74]. A capillary number of 10^{-7} was kept the same for the three stages, indicating capillary dominant flow regime [74]. The first observation was that the remaining oil saturation was not reduced by the nanofluid, however, the distribution of the oil clusters/ganglia changed locations in the pore-space, particularly for the 0.12 wt% nanofluid [74]. Secondly, it was found that increasing the concentration of the NPs leads to smaller oil ganglia and larger oil-brine interface, suggesting that nanoparticles can create oil-in-water emulsions [74]. Furthermore, they proved it by 3D micro-visualization and observed that larger pores had most of the oil-in-brine emulsions, see Figure 29 (oil in light gray, brine in black, rock in dark gray) [74]. The effectiveness of the higher concentration of NPs in remobilizing the trapped oil and also to create stable emulsions (lower number of coalescence events) is due to the lower interfacial tension caused by high number of NPs at the oil-brine interface [74].

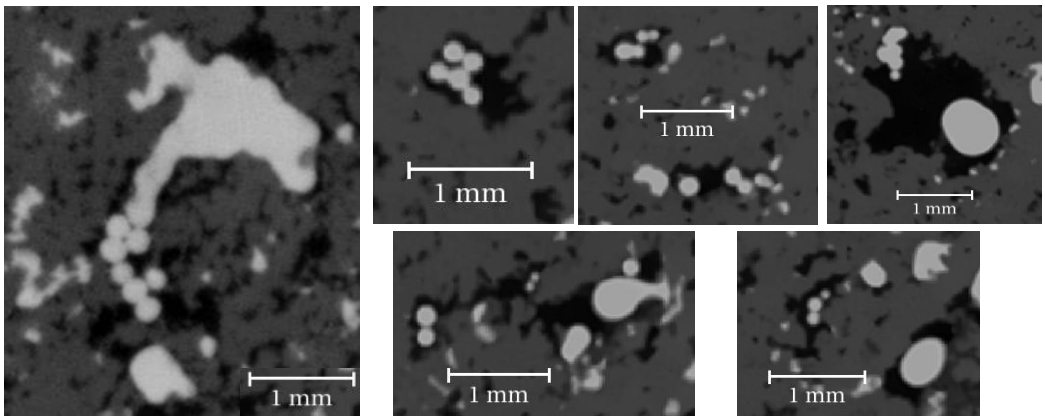

Figure 29: Pore-scale images for oil-in-brine emulsions after the 0.12 wt% nanofluid flooding [74]

Zhang et al (2016). They performed several experiments with a glass bead pack and designed them to start with a secondary recovery ($C_a = 10^{-7}$) by waterflooding, then flooding either with brine or a 0.227 wt% polymeric nanofluid at ($C_a = 10^{-7}$, 10^{-5}, or 10^{-4}) [73]. Pore-scale analysis showed that the capillary number increased as the incremental oil recovery declined when using the nanofluid, which was opposite to the observations during brine flooding [73]. This interesting observation was explained by calculating the time needed for nanoparticles layering in the wedge region, explained in section 2.1, to create enough structural disjointing pressure to detach the oil phase from the bead matrix [73].

$$T_f = \frac{D_p}{v_{in}} \tag{18}$$

$$T_a = \frac{L\emptyset}{U} \tag{19}$$

Equation 1 estimates the layering formation time T_f; where D_p is the grain diameter, and v_{in} is the inner contact line velocity [73]. T_f should be less than the advective transport time (T_a) of the nanoparticles inside the sample, given by equation 2; where L is the sample length, $\emptyset$ is the sample porosity and U is the superficial velocity [73]. It was found that only the lowest C_a provided that $T_f << T_a$, enabling the structuring phenomenon to alter the rock wettability, leading to a higher recovery [73]. To make sure that time played a significant role in the ability of NPs to enhance oil recovery, the process after tertiary recovery by nanofluid was stopped for some time and then the flooding was continued at the same C_a [73]. They found that the longer the cease of flow period (longer soaking time) resulted in higher oil recoveries [73]. The pore-scale visualization showed that nanofluids are considerably capable of reducing the sizes of the remaining oil clusters [73].

These two studies presented how interesting findings at pore-scale can be obtained via micro-CT. However, there are still many situations and ideas to be discovered at pore-scale in the

future to obtain new insights about nanotechnology for EOR. In addition, these two studies showed that at the same flooding scenario (same $C_a = 10^{-7}$), the results were different due to different type and concentration of NPs, and pore-space structure.

Chapter 4

A Surface Area Index to Describe Wetting of Surfaces

In chapter 1, wettability was defined as the relative tendency of one of two or more immiscible fluids to adhere to, spread on or wet the grain surfaces within a porous medium, depending on the chemical nature and spread ability of the fluids, physical and chemical nature of the grain surfaces (controlling preferentiality), and pore-scale complex physical and chemical interactions between the rock and fluids [10, 11, 28, 45-50]. In other words, it is a competition between at least two fluid phases to maintain physical contact with solid surfaces, which is controlled by several factors.

Chapter 2 showed that wettability is described by in-situ contact angles measured at three-phase contact points and a distribution of contact angles or a mean value is an indicator of the rock wettability. In available literature, there is no attempt to utilize/report the fraction of grain surfaces is coated by the wetting phase or the non-wetting phase to indicate wettability at pore-scale. In addition, chapter 3 showed that structural disjoining pressure resulting from the structuring of nanoparticles in the wedge region is able to detach the oil phase from the rock surface, and it is a function of several factors such as nanofilm formation time and concertation. This phenomenon was studied on smooth flat surfaces [81-85] to see the reduction in contact with the surface, and by 3D micro-visualization to only quantify the reduction in non-wetting phase saturation due to increased nanofilm formation time (T_f) [73].

Quantifying the fraction of solid surfaces wetted by each phase can be a solid descriptor for understanding processes and mechanisms in porous media. For example, it can be used to indicate wettability of a porous medium since wettability is defined based on surface wetting. Another example, the alteration of wettability by structuring of nanoparticles can be directly related to the reduction in oil contact with the natural solid surface at pore-scale using this fraction, as an alternative to using sessile drop on smooth surfaces of a single mineral i.e. quartz. It also provides a direct evidence of the effect of nanofilm formation time (T_f) on detaching the oil phase from the solid surfaces, as an alternative to measuring the incremental oil recovery (reduction in S_o) with different soaking times.

This chapter firstly provides the method to quantify a surface area index to describe wetting of surfaces from micro-CT images. After that, it uses two open 3D data for flow and trapping

experiments. The surface area index is calculated to correlate it to in-situ contact angle as well as fluid topology and pore-scale events.

4.1 Method

Consider a rock with water as wetting phase and oil as non-wetting phase, the surface area index (S.A.I.), defined as the fraction of the surface area of the grain wetted by the water, is given by equation 1; where A_{ww} is the grain surface area wetted by water and A_{wo} is the grain surface area wetted with oil. To extract these parameters, image analysis is applied on segmented 3D images where the three phases (grain, water and oil) are distinguished, see Figure 30. The software used to find the surface area index is aviso 9.2 (by Thermo Fisher Scientific) and ImageJ (by U. S. National Institutes of Health, Bethesda, Maryland, USA). Figure 31 demonstrates the workflow followed to find A_{ww} and A_{wo}.

$$\text{Surface area index}\,(\text{S.A.I.}) = \frac{A_{ww}}{A_{ww}+A_{wo}} \tag{20}$$

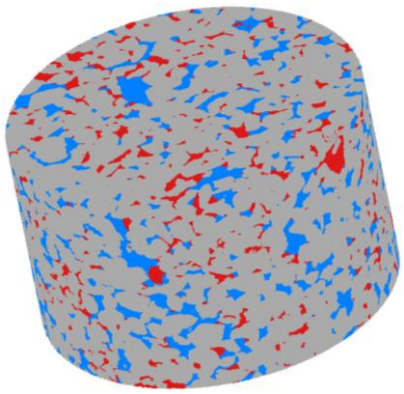

Figure 30: Segmented 3D image; where rock in gray, oil in red and water in blue

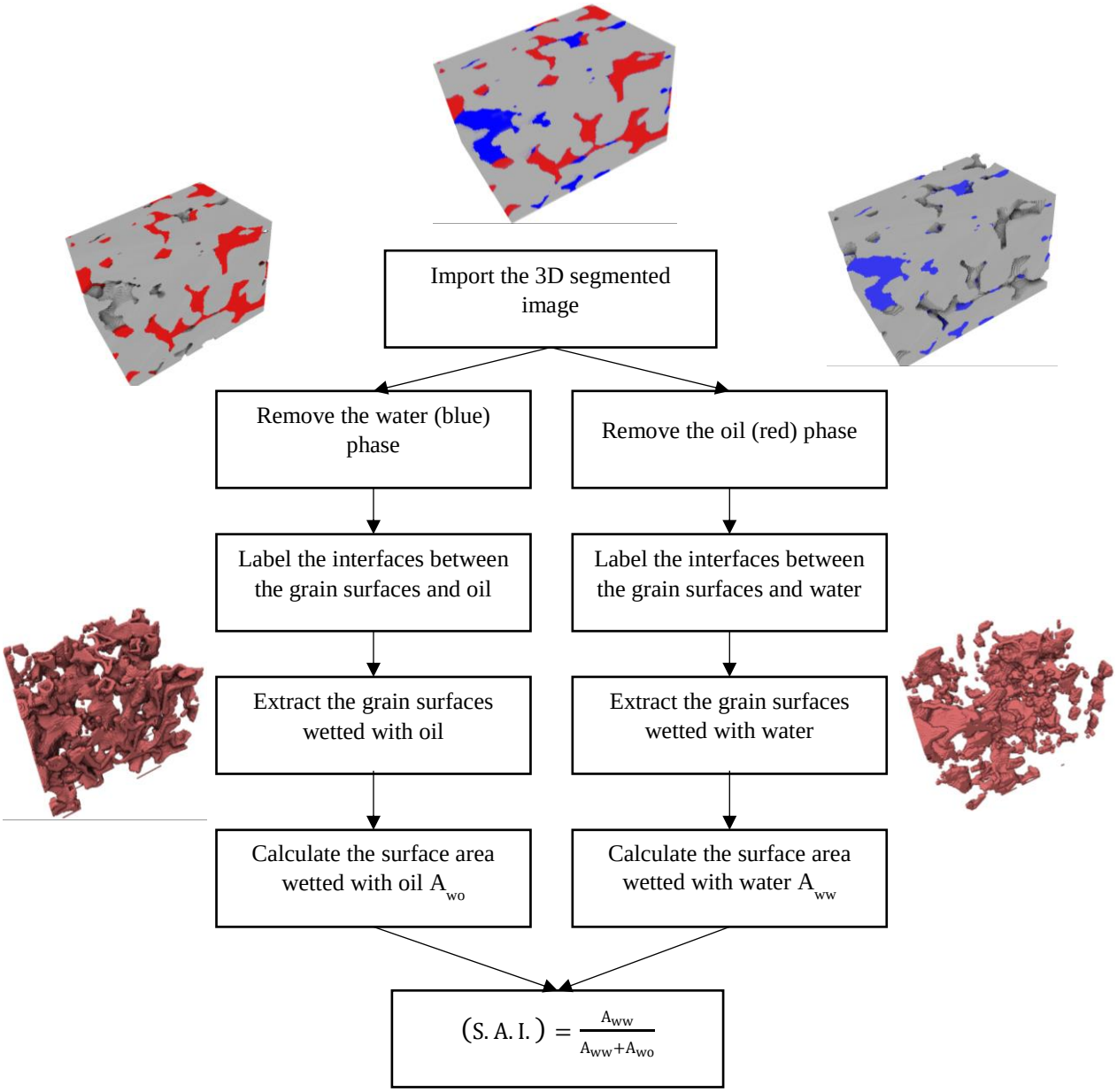

Figure 31: Workflow to calculate the surface area index using Avizo 9.2

4.2 Open Data

To be able to evaluate the surface area index, there is a need for many experiments to see how it correlates to wettability, saturations, fluid topology, and pore-scale. Therefore, this thesis takes advantage of the available data from two pore-scale studies. Table 3 presents the references of data and related publications (note this chapter refers to each dataset as dataset 1 and dataset 2).

Table 3: References for open data used to test the surface area index

Dataset #	Related Publications	Reference for Data
1	• Amer M. Alhammadi, Ahmed AlRatrout, Kamaljit Singh, Branko Bijeljic & Martin J. Blunt, (2017), In situ characterization of mixed-wettability in a reservoir rock at subsurface conditions, *Scientific Reports*, https://doi.org/10.1038/s41598-017-10992-w. • AlRatrout, A., Blunt, M. J., & Bijeljic, B., (2018), Spatial correlation of contact angle and curvature in pore-space images, *Water Resources Research*, 54, 6133–6152, https://doi.org/10.1029/2017WR022124.	Alhammadi, A., AlRatrout, A., Bijeljic, B., & Blunt, M, (2018), X-ray micro-tomography datasets of mixed-wet carbonate reservoir rocks for in situ effective contact angle measurements, *Digital Rocks Portal*, https://doi.org/10.17612/P7VQ2G.
2	• Rücker, M., S. Berg, R. T. Armstrong, A. Georgiadis, H. Ott, A. Schwing, R. Neiteler, N. Brussee, A. Makurat, L. Leu, M. Wolf, F. Khan, F. Enzmann, and M. Kersten, (2015), From connected pathway flow to ganglion dynamics, *Geophys. Res. Lett.*, 42, 3888–3894, https://doi.org/10.1002/2015GL064007. • F.O. Alpak, S. Berg, I. Zacharoudiou. (2018) Prediction of fluid topology and relative permeability in imbibition in sandstone rock by direct numerical simulation, *Advances in Water Resources*, 122, 49-59. https://doi.org/10.1016/j.advwatres.2018.09.001. • S. Berg, M. Rücker, H. Ott, A. Georgiadis, H. van der Linde, F. Enzmann, M. Kersten, R.T. Armstrong, S. de With, J. Becker, A. Wiegmann, (2016), Connected pathway relative permeability from pore-scale imaging of imbibition, *Advances in Water Resources*, 90, 24-35, https://doi.org/10.1016/j.advwatres.2016.01.010.	Berg, S., Armstrong, R., & Wiegmann, A. (2018), Gildehauser Sandstone datasets, *Digital Rocks Portal*, https://doi.org/10.17612/P7WW95.

4.3 Results and Discussions

4.3.1 In-Situ Contact Angle

Dataset 1 includes micro-CT images for three carbonate samples of different wettability states due to saturation with different oils. It was found that the three samples (sample 1, sample 2, and sample 3) showed different oil recovery factors (67.1%, 58.6% and 84%, respectively), and mean in-situ contact angles (77°, 104°, and 94°, respectively) [59]. The authors explained that the highest recovery was due to the intermediate wettability state in sample 3, since it has lower rate of oil trapping by snap-off events and no formation of oil layers within the sample [59]. The surface area index was calculated for the three samples, results are shown in Table 4 and Figure 32.

Table 4: Surface area index and mean in-situ contact angle for the samples in dataset 1

Sample #	Mean in-Situ Contact Angle [59]	Surface Area Index
Sample 1	77°	0.796
Sample 2	104°	0.427
Sample 3	94°	0.690

Table 4 and Figure 32 show that the surface area index increases as the mean in-situ contact angle decreases, which is described with a linear relationship with a coefficient of determination (R^2) of 0.86. For sample 1, the most water-wet sample, most of the oil is trapped by snap-off, which leads to losing most of the oil contact with the grain surfaces, resulting in the highest S.A.I. The opposite case is sample 2 with the lowest S.A.I. and it has the most oil-wet state, leading to continuous oil layers in the sample which are in contact with the grain surfaces. The snap-off events and formation of oil layers along the grain surface are not favoured in the intermediate wet state, such as sample 3, leading to a S.A.I of 0.690.

Although there is a need for more samples to test the relationship between the surface area index and mean in-situ contact angle, the index works well to compare the state of wettability. In addition, these data provide an indication that the index can describe the non-wetting phase topology and pore-scale events.

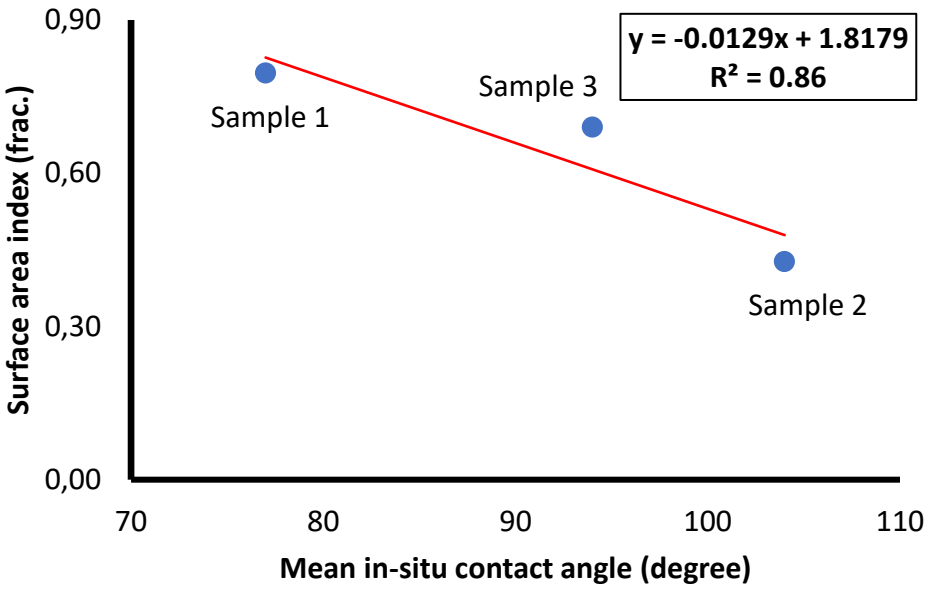

Figure 32: Surface area index as a function of mean in-situ contact angle for dataset 1

4.3.2 Fluid Topology

Based on the aforementioned discussion in section 3.4.1, the connectivity of the remaining oil in the three samples in dataset 1 should be the most in sample 2 (oil exists as wetting layers) and the least in sample 1 (oil trapped by snap-off). Avizo 9.2 is used to apply the method discussed in section 1.2.3 for the Euler characteristic on these samples. Table 5 includes the results and confirms the relationship between the surface area index and the non-wetting phase connectivity based on the discussion above.

The positive Euler number for the residual oil in sample 1 indicates that there are many components i.e. clusters with Euler number of 1 and as discussed in section 1.3.1, this means that there are no redundant loops/connections for the trapped oil clusters. The loss of these connections strongly supports that the oil was snapped off in the pore-throat regions. Sample 2 shows a very low Euler number for the remaining oil which indicates high connectivity in the remaining oil and as a result many redundant loops/connections. This indicates that the oil remains in the sample as connected layers with many branches within the sample. Sample 3 has a negative Euler number which indicates that there are clusters with redundant loops/connections.

To accurately compare between the oil topology in the three samples, the normalized Euler number by pore-space connectivity (given by equation 12 in chapter 1) is calculated and reported in Table 5. Note that normalized Euler number of 1 is the maximum possible connectivity and a negative value indicate the presence of more clusters/components with no

redundant loops/connections. Table 5 and Figure 33 show that the surface area index increases as the connectivity of the remaining oil decreases, which is described with a strong linear relationship with a coefficient of determination (R^2) of 0.9997.

Table 5: Surface area index, mean in-situ contact angle and Euler number for the samples in dataset 1

Sample #	Mean in-Situ Contact Angle	Surface Area Index	Euler Number	Normalized Euler Number ($\hat{\chi}_o$)
Sample 1	77°	0.796	537	-0.297
Sample 2	104°	0.427	-42997	0.895
Sample 3	94°	0.690	-754	0.065

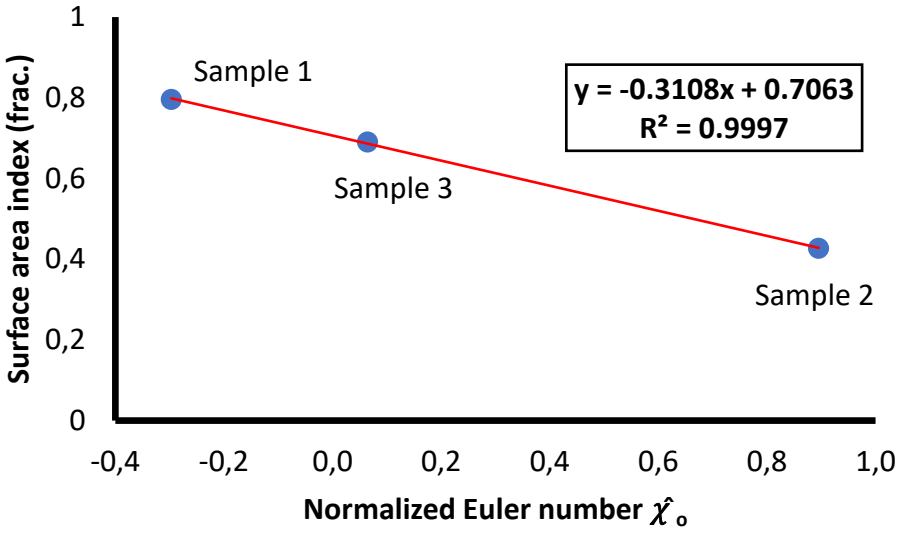

Figure 33: Surface area index as a function of normalized Euler number ($\hat{\chi}_o$) for dataset 1

Dataset 2 presents imaging using fast synchrotron-based X-ray computed microtomography of an imbibition process in a Gildehauser sandstone sample under capillary-dominated flow regime [5]. The authors showed the change in oil topology described by Euler characteristic (not normalized) as a function of time [5]. Since the available number of scans is 40 for this experiment, a similar figure to Figure 33 can be generated after calculating the normalized Euler number ($\hat{\chi}_o$), to confirm the linear relationship between the surface area index and normalized Euler number ($\hat{\chi}_o$), using 40 data points. Figure 34 shows that the relation is strongly linear with a coefficient of determination (R^2) of 0.9976. Therefore, the surface area index is an excellent indicator of the non-wetting phase topology.

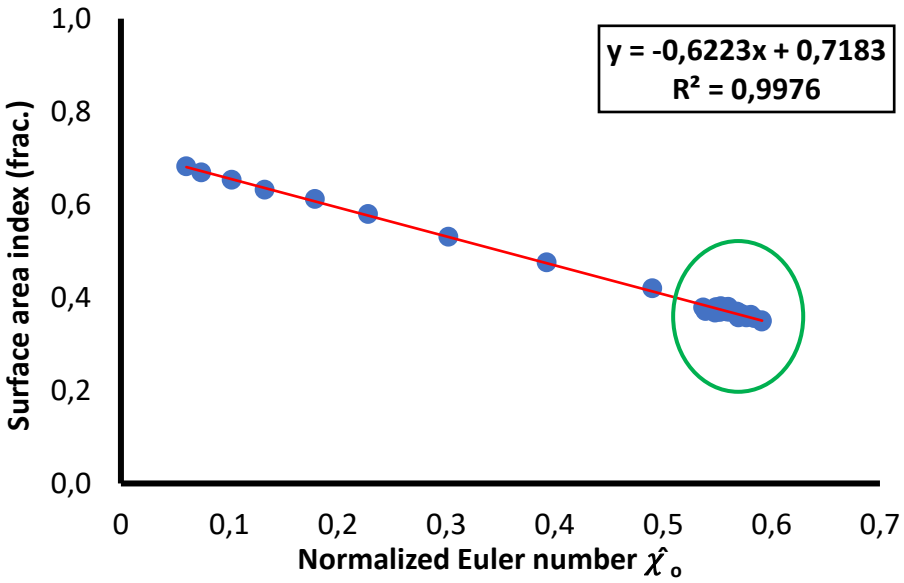

Figure 34: Surface area index as a function of normalized Euler number ($\hat{\chi}_o$) for dataset 2

4.3.3 Pore-Scale Events

The change in the oil phase topology and surface area index is not significant for many points (scans) from dataset 2, indicated by the green circle in Figure 34. These points correspond to early and middle time of imbibition. The late time of imbibition shows higher changes in topology and contact surface area, which slows down at the end of the imbibition, due to the approach to the residual oil saturation. Figure 35 demonstrates that the change in contact surface area with the wetting phase, i.e. water, has only increased by 0.03 for 1200 seconds, and then increased by 0.303 during the last 400 seconds.

Rücker et al (2015) mentioned that the early and middle time of imbibition had wetting layers swelling and corresponding snap-off processes and the late time had dynamic displacement events [5]. Based on the discussion of snap-off in section 1.2.2.1, the non-wetting phase losses the contact with surface of the pore-throat when the critical capillary pressure is met, therefore, the small incremental index area is reasonable since the dynamic displacing events had no effect before t = 1200 s. Therefore, the surface area index is a useful tool in imaging of dynamic experiments to indicate the start of the dynamic displacement events such as pore-filling and pore-throat filling.

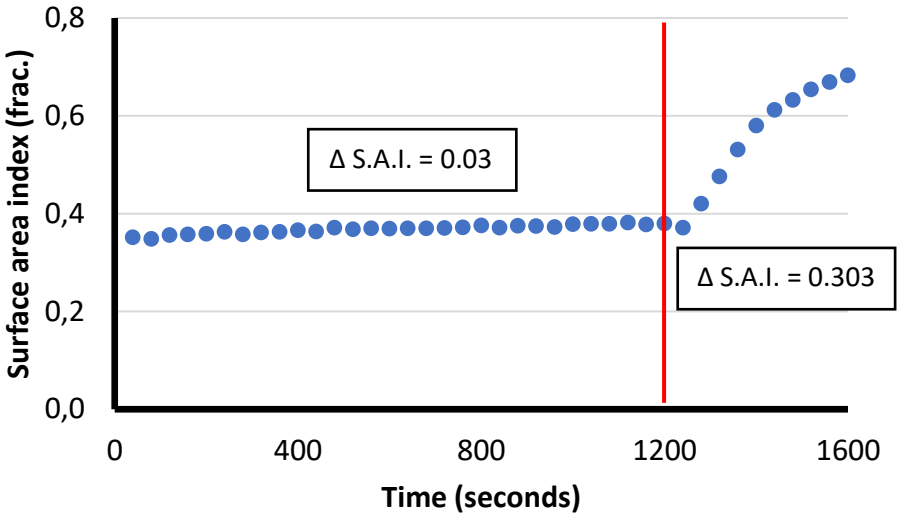

Figure 35: Surface area index as a function of imbibition time for dataset 2

Chapter 5

Experimental Materials and Methods

5.1 Rock and Fluids Properties

Rock. Five miniature samples were drilled from a Bentheimer sandstone plug, see Figure 36. The petrophysical properties and dimensions of the parent plug and the 6 miniature samples are presented in Table 6 and Table 7, respectively.

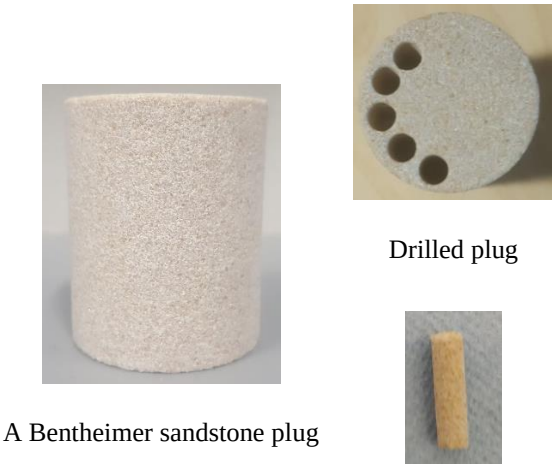

Figure 36: A Bentheimer sandstone sample from which the mini samples were drilled

Table 6: Petrophysical parameters and dimensions of the parent Bentheimer sandstone plug

Plug name	Diameter (cm)	Length (cm)	Porosity φ (%)	K_L (mD)	Pore volume (cm^3)
Bentheimer	3.78	4.55	16.77%	962.99	8.56

Table 7: Petrophysical parameters and dimensions of the six miniature samples

Sample name	Diameter (mm)	Length (mm)	Porosity φ (X-ray) [a] (%)	Pore Volume [b] (mm^3)
S1	4.0	14.9	16.00	31.29
S2	4.0	13.4	16.71	27.26
S3	4.0	15.2	15.85	30.70
S4	4.0	12.6	15.80	25.37
S5	4.0	16	16.56	33.3

[a] was determined from the imaged part of the mini sample.

[b] assuming that the imaged part and the whole miniplug have the same mean X-ray porosity.

Fluids. Crude oil from Heidrun field was used for the primary and main drainage, as the non-wetting phase. The fluid properties and composition of the oil are presented in Table 8. The crude oil was filtered before injection to avoid plugging problems in the small tubes of the core-holder assembly as well as plugging of the small pore-throats within the sample. In addition, the crude oil was degassed to avoid the presence of air bubbles in the porous medium.

Table 8: Properties of the crude oil used in the experiments

	Density (g/cm^3)	Viscosity (mPa-s)	Oil/brine IFT (mN/m)	Oil/nanofluid IFT (mN/m)
Crude oil	0.9087	61	13.64	5.35

The wetting fluids for imbibition tests were degassed brine (7 wt.% caesium chloride (CsCl)) and nanofluid (7 wt.% caesium chloride (CsCl) + 0.1 wt.% nanosilica). Table 9 provides the fluid properties of the brine and nanofluid. The addition of the nanosilica to the brine increased the density and viscosity by 3.1% and 8.8%, respectively, and it decreased the interfacial tension with the oil phase by 60.2%. In addition, the silica NPs used in this study has an average diameter of 144.5 nanometre, and the size distribution is shown in Figure 37.

Table 9: Properties of the fluids used in the experiments

Fluid	Density (g/cm^3)	Viscosity (mPa-s)
Brine (7 wt.% CsCl)	1.0883	1.02
Nanofluid (7 wt.% CsCl + 0.1 wt.% NPs)	1.1226	1.11

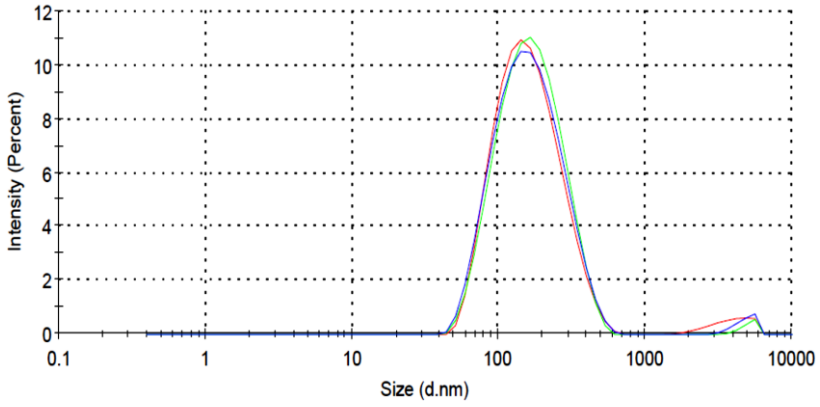

Figure 37: Nanoparticles size distribution by intensity (three tests are shown)

Methods and equipment. The porosity of the parent rock was measured using a helium porosimeter (manufactured by Core Laboratories, USA) based on Boyle's law. The liquid permeability was estimated using Klinkenberg correlation between apparent gas permeability at mean pressures and the true liquid permeability [88]. The X-ray porosity was estimated by segmenting the pore space from the grain phase by using watershed segmentation method included in Avizo Software 9.2 (developed by Thermo Fisher Scientific). Appendix A elaborates on the helium porosity, Klinkenberg permeability and X-ray porosity for this study.

The fluid density was measured using a highly precise digital density meter (DMA™ 5000 M developed by Anton Paar) and the fluid viscosity was measured using a digital rotational viscometer (DV-II+Pro developed by Brookfield Engineering Laboratories, USA). The interfacial tension between the wetting and non-wetting phase was measured using the pendant drop method via a drop shape analyser (DSA100S manufactured by KRÜSS GmbH, Germany).

The particle size distribution of the NPs in the brine was determined using dynamic light scattering technique via a digital sizer (Zetasizer Nano developed by Malvern Panalytical, UK). The fluids properties presented in this section are measured at room conditions i.e. 21 ^{o}C and 1 atm. The filtration and degassing process of the fluids are shown in Appendix B.

5.2 Experimental Setup

A core-flooding setup integrated in a micro-CT scanner was used to perform the experiments in this study. A task of this thesis is to design the core-flooding setup and to set protocols for flooding and trapping experiments inside the micro-CT scanner. There were several challenges associated with the process of building the setup. Risk assessment was applied to protect the electrical and mechanical parts in the small-chamber micro-CT from the fluids, and quality control was performed to ensure the accuracy of the fluid types and fluid pore-configuration within the sample. Consequently, trails of the setup led to the replacement of components of the system with higher quality ones, and new components were also added to the setup. This section presents the final stable design of the experimental setup for the experiments in this study.

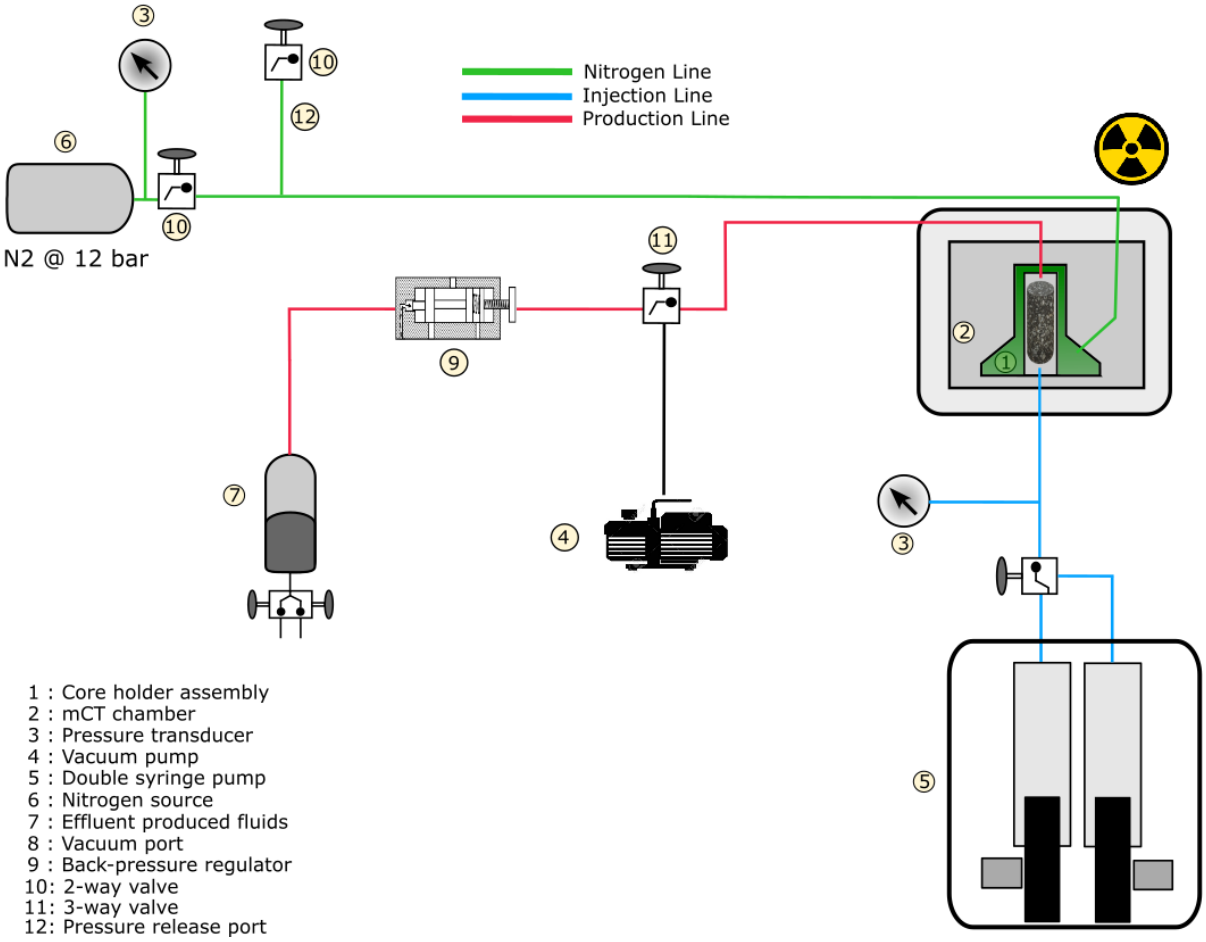

Figure 38: Schematic diagram of the core-flooding setup integrated with the micro-CT scanner

Core-Holder Assembly. The core-holder, see Figure 39, is custom made and manufactured by Reservoir Study Systems (RSS), Norway. The carbon PEEK core-holder has a maximum working pressure of 30 bar @ 25 ºC, and it had originally two production tubes connected at the top of the flow cell and three injection tubes at the bottom of the flow cell. There is a port for the confining pressure at the base of the core-holder. A main advantage of this core-holder is its small size, which made it easier to integrate it inside the micro-CT scanner. The second advantage that the tubes can be replaced in case of plugging, which occurred twice during the experiments. The maintenance of the core-holder takes a full day to properly glue the tubes and ensure a perfect seal. Therefore, filtration of the liquid is highly recommended to save time.

Since the experiments in this study has no fractional flow, the injection tubes were reduced to only one tube. In addition, the second production line was also removed, since there it was not possible to connect to a pressure transducer inside the micro-CT scanner. The removal of the extra tubes provided less difficulty of placing the core-holder on the scanner stage and helped to reduce the risk of leakage from these tubes, particularly the sample rotates during the scan. Furthermore, the backflow from these tubes to the sample was excluded. For example, after the

stop of the flow, if the second production tube (10 cm in length and has a closed end) has a wetting phase, i.e. brine, the brine will spontaneous imbibe to the sample, leading to a change in the fluid distribution within the sample. Removing the extra tubes was beneficial for this study.

Figure 39: Core-holder manufactured by Reservoir Study Systems (RSS), Norway

The biggest challenge encountered during the testing of the setup is to find a re-producible way to seal the top and bottom part of the Viton rubber sleeve. Appendix C presents the best practice to prevent high-pressure air (confining pressure @ 10 bar) leaking to the inner volume of the sleeve where the sample is located.

Micro-CT Scanner. The micro-CT scanner used in this study is the SkyScan 1172 manufactured by SkyScan, Belgium. Figure 40 shows the micro-CT scanner which has an X-ray energy between 20-100kV. The stage as well as the detector (a 11-megapixel digital camera) can be moved by changing the settings from the scanner software installed on the micro-CT desktop. There is a monitoring camera installed inside the chamber to view the sample while changing the vertical position of the stage. A challenge associated with this scanner is that the chamber is small, which made the placement of the core-holder and tubes a difficult task, see Figure 41.

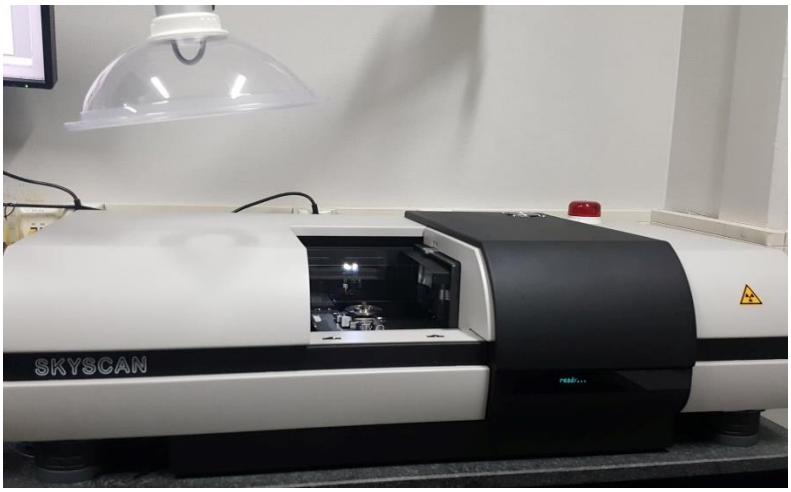

Figure 40: SkyScan 1172 micro-CT scanner used for the experiments of this study

Figure 41: The core-holder and tubes fixed on the scanner stage

Back-pressure regulator. The function of a back-pressure regulator is to stop the flow at its connection until the fluid pressure reaches a given pressure value. A high accuracy back-pressure regulator (from Bronkhorst High-Tech BV, Netherlands) with a full scale of 10 bar, see Figure 42, was used in the setup of this study. The regulator was connected to a computer to set the pressure value. It was used to increase the pore-pressure (i.e. the pressure of the fluids in the sample) while performing the primary imbibition. A high pore-pressure increases the solubility of the air in the brine following Henry's Law [89], hence, the tiny air bubbles presence in the system would easily dissolve in the brine and be produced after flooding the sample with many pore volumes.

Figure 42: A high accuracy back-pressure regulator used in the setup of this study

This approach significantly helped to solve the challenge of the air bubbles presence in the system. It was observed from the live X-ray projections that the higher back pressure in the system moved the air bubbles to the outlet end of the core-holder (top of the sample). After the sample is fully saturated with the brine, the set-value of the pressure was gradually decreased to zero. In addition, instead of using a manual valve to stop the flow after the imbibition or drainage test, the regulator was used, which provided a faster control.

The software application of this regulator provided an accurate measurement of the fluid pressure passing the regulator. The pressure obtained by the software was used to indicate the change in pressure within the system after stopping the flow, which is essential to ensure that the fluid interfaces reached an equilibrium. Furthermore, since the regulator showed a live single of the pressure during the scanning time, it was used to indicate a leakage inside the X-ray chamber, which would appear as a pressure drop. The back-pressure regulator was beneficial for the experiment setup via removing the air phase, indicate equilibrium state, and guarding the micro-CT scanner from the fluids.

Double syringe pump. The Harvard Apparatus pump 33 DDS (dual drive system), see Figure 43, was used in this system to precisely control the injection rate and injected volume to the system. Having two pumping channels made the change from a drainage process to an imbibition process easier and time-saving.

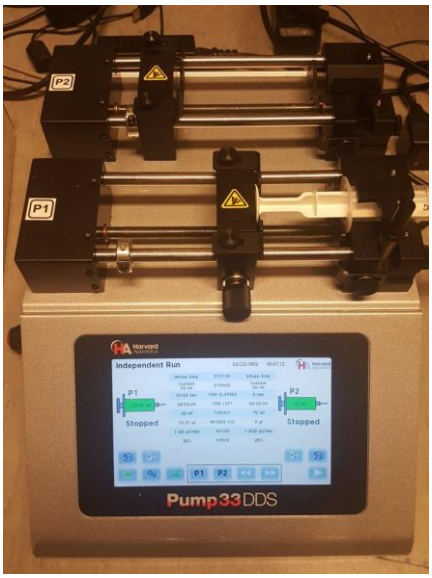

Figure 43: Harvard Apparatus pump 33 DDS (dual drive system) used in the setup of this study

Vacuum pump. Its function is to evacuate the air from the system prior to the primary imbibition to remove all the air from the system. The protocol was to vacuum the system until its pressure reaches 15 millitorr (0.02 millibar), see Figure 44 for reading of the vacuum gauge (275 Mini-Convectron, Granville-Phillips, USA) at the end of the vacuuming process. Lower values of pressure were not possible; however, the use of the back-pressure regulator and the degassing of the fluids provided a fully saturated sample.

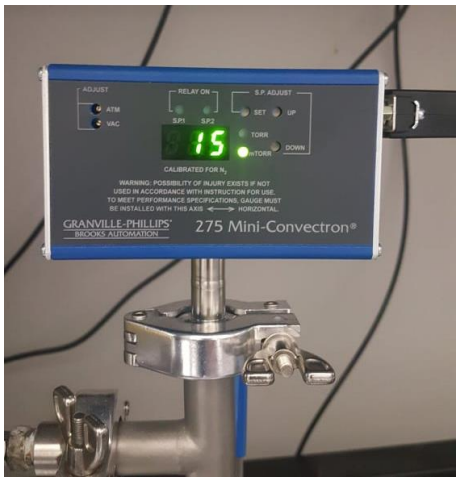

Figure 44: Vacuum gauge showing 15 millitorr pressure in the setup system

Pressure transducers. Two pressure transducers were used in the setup. The first one was connected to the nitrogen gas line to indicate any leakage occurrence. If the gauge shows a pressure drop, it means that either the confining air found a way to enter the inner volume of the sleeve or the connection between the end of the nitrogen line and the core-holder is loose. The loosening of this connection can be due to the rotation of scanner stage.

5.3 Experimental Procedure

Performing an experiment for this study started with placing the miniature sample in the core holder according to the procedure presented in Appendix C. After that, the core-holder assembly was tested by immersing the production and injection tube in water, while the confining pressure was connected to the core-holder, to check that there was no communication between the inner volume of the sleeve and the confining gas.

After passing this test, the core-holder was fixed on the scanner stage as seen in Figure 41. Next, the core system was vacuumed until the vacuum gauge showed 15 millitorr (0.02 millibar). Before starting the imbibition test, the sample was scanned with a resolution of 6.38 μm. This scan is called the dry scan of the sample, which is used to extract the pore-space of the sample.

The next step was to perform brine injection at 200 μl/min for 300 pore volumes (PVs) while the back pressure is 4.5 bar. An additional 50 PVs were injection at 20 μl/min with gradually decreasing the back pressure until it reaches 0 bar. After that, another scan of the same resolution was performed to ensure that this approach fully saturated the core with the brine.

To perform primary drainage, the filtered oil was injected at a flow rate of 20 μl/min for 25 PVs. Then, the core sample was scanned to obtain the fluid saturation pre-imbibition to quantify the initial oil saturation (S_o). After this step, the imbibition test to recover the oil phase was performed at the specified conditions in the next section 5.4. the last step was to scan the same sample to evaluate the final state after imbibition for fluid saturations, topology, wetted surfaces and recovery factors. Appendix D presents the main steps to process the micro-CT images after reconstructing them. A summary of the experimental procedure is presented in Figure 45.

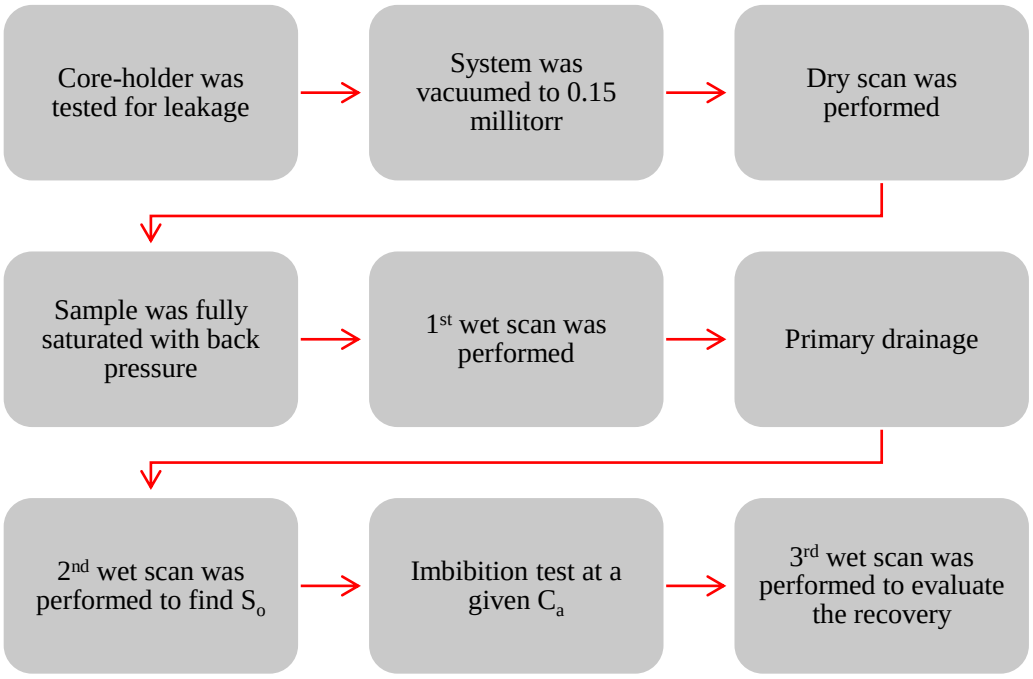

Figure 45: Experimental procedure used for the experiments in this study

5.4 Recovery Schemes Overview

Seven recovery schemes are evaluated in this study. The aim of these experiments is to discover the induced changes to the in-sit fluid distribution and configuration at given conditions. Based on the imbibition fluid, the experiments can be classified into brine (no NPs) flooding experiments and nanofluid (0.1 wt. % NPs) flooding experiments. The recovery scheme is called secondary recovery when it is after the primary drainage. When the secondary recovery is followed by another imbibition test, the recovery scheme is called tertiary recovery.

The first three experiments (I1, I2, and I3) were performed on sample S1. They were secondary recovery with brine (no NPs). The next three experiments (I4, I5, and I6) were performed on sample S2, S3, and S4 respectively. They were secondary recovery experiments with the nanofluid. The last experiment was a tertiary recovery test using nanofluid fluid performed after the secondary recovery experiment (I3) performed on S1. The injection flow rates and corresponding capillary numbers are given in Table 10.

Table 10: Flow rate and its corresponding C_a for the seven recovery schemes in this study

Experiment	Sample	Imbibition fluid	Recovery scheme	Flow rate Q (µl/min)	Capillary number (C_a) [b]
I1	S1	Brine	Secondary	50	2.955×10^{-05}
I2	S1	Brine	Secondary	100	5.910×10^{-05}
I3	S1	Brine	Secondary	150	8.865×10^{-05}
I4	S2	Nanofluid	Secondary	18[a]	2.955×10^{-05}
I5	S3	Nanofluid	Secondary	36[a]	5.910×10^{-05}
I6	S4	Nanofluid	Secondary	54[a]	8.865×10^{-05}
I7	S1	Nanofluid	Tertiary	54[a]	8.865×10^{-05}

[a] rounded off to the nearest whole number.
[b] calculated using equation 13 and 14 in section 2.3.1.

Chapter 6

Results and Discussion

6.1 Secondary Recovery

6.1.1 Capillary Number Effect on Trapped Oil and Recovery

As discussed in section 2.3.1, the capillary number, which is a function of interfacial tension, flow rate and fluid viscosity, significantly affects the trapping of the non-wetting phase within a porous media. Considering the brine imbibition tests (I1, I2, and I3), the capillary number of the brine imbibition experiments increased with only using higher flow rates. Similarly, the injection flow rate of the nanofluid imbibition tests (I4, I5, and I6) was increased to achieve higher capillary numbers. Therefore, the flowrate effect on trapping of crude oil in the Bentheimer sandstone can be examined. In addition, the three capillary numbers used in I1, I2, and I3 are the same for I4, I5, and I6, respectively. This was achieved by solving the capillary number equation for flow rates by using the lower IFT between the crude and the nanofluid, and the higher nanofluid viscosity. This enables a comparison between the two fluids at the same capillary numbers after secondary recovery.

Brine flooding (I1, I2, & I3). The amount of trapped oil decreased with increasing the injection flow rate, leading to a higher oil recovery factor, see Table 11. Although the flow rate of I2 and I3 were two-fold and three-fold of the flow rate in I1, the induced change in trapped oil and oil recovery did not follow a similar trend. The reason can be related to the flow regime type, such that the highest flow rate had much higher viscous-dominated flow regime than the second flow rate. Another reason might be that the injected pore volumes were more than 10 PV for I1, which was designed for all secondary recoveries.

Table 11: Flow rates for the brine experiments, and their corresponding S_{or} and R.F.

Experiment	Flow rate (Q)	Capillary number (C_a)	Residual oil saturation (S_{or})	Recovery factor (R.F.)
	µl/min	-	frac.	%
I1	50	2.955×10^{-05}	0.372	49.83
I2	100	5.910×10^{-05}	0.349	52.86
I3	150	8.865×10^{-05}	0.224	68.87

The remaining oil saturation consisted of smaller oil clusters with increasing the flow rate (capillary number) as shown in Figure 46. Comparing the size of clusters in the remaining oil and the oil recovery resulting from the different flow rates, it shows that the large oil clusters within the sample broke into smaller ones that can be produced (mobilized) or trapped. The results indicate that the trapping proportion of the fragmented oil clusters was higher in I2, whereas I3 had a higher proportion of the fragmented clusters to be produced. This suggests that the initial biggest cluster in I2 lost the oil from the connections, i.e. pore-throats, and the oil became trapped in the large pores via less connections/loops. This is verified by comparing the biggest cluster in all experiments as seen in Figure 47. The largest remaining oil cluster in I3 had a smaller size (volume) by 74% compared with I1 largest cluster and by 38% compared with I2 largest cluster, see Figure 47.

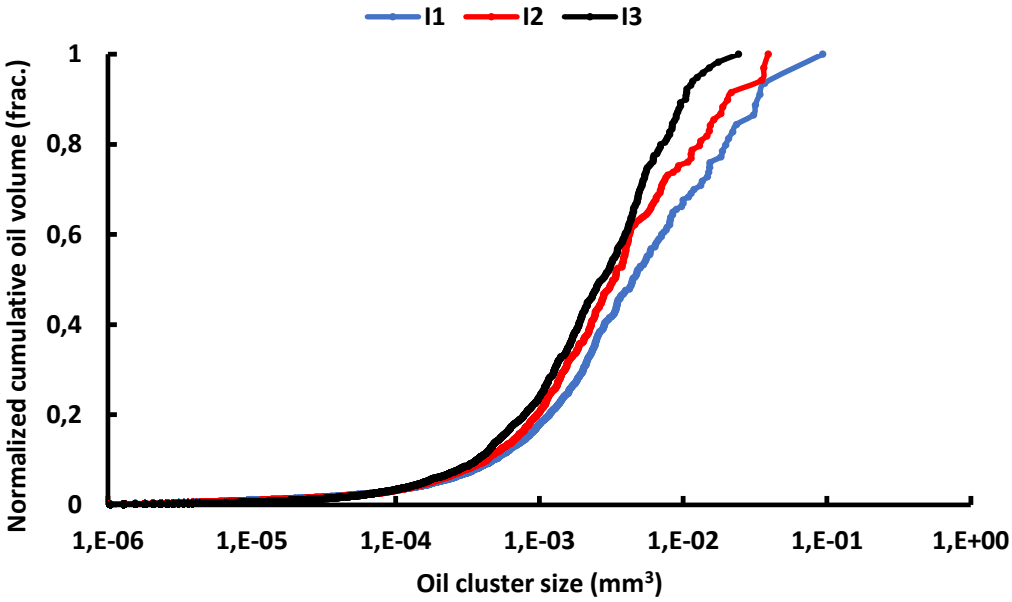

Figure 46: Normalized cumulative residual oil volume as a function of oil cluster size

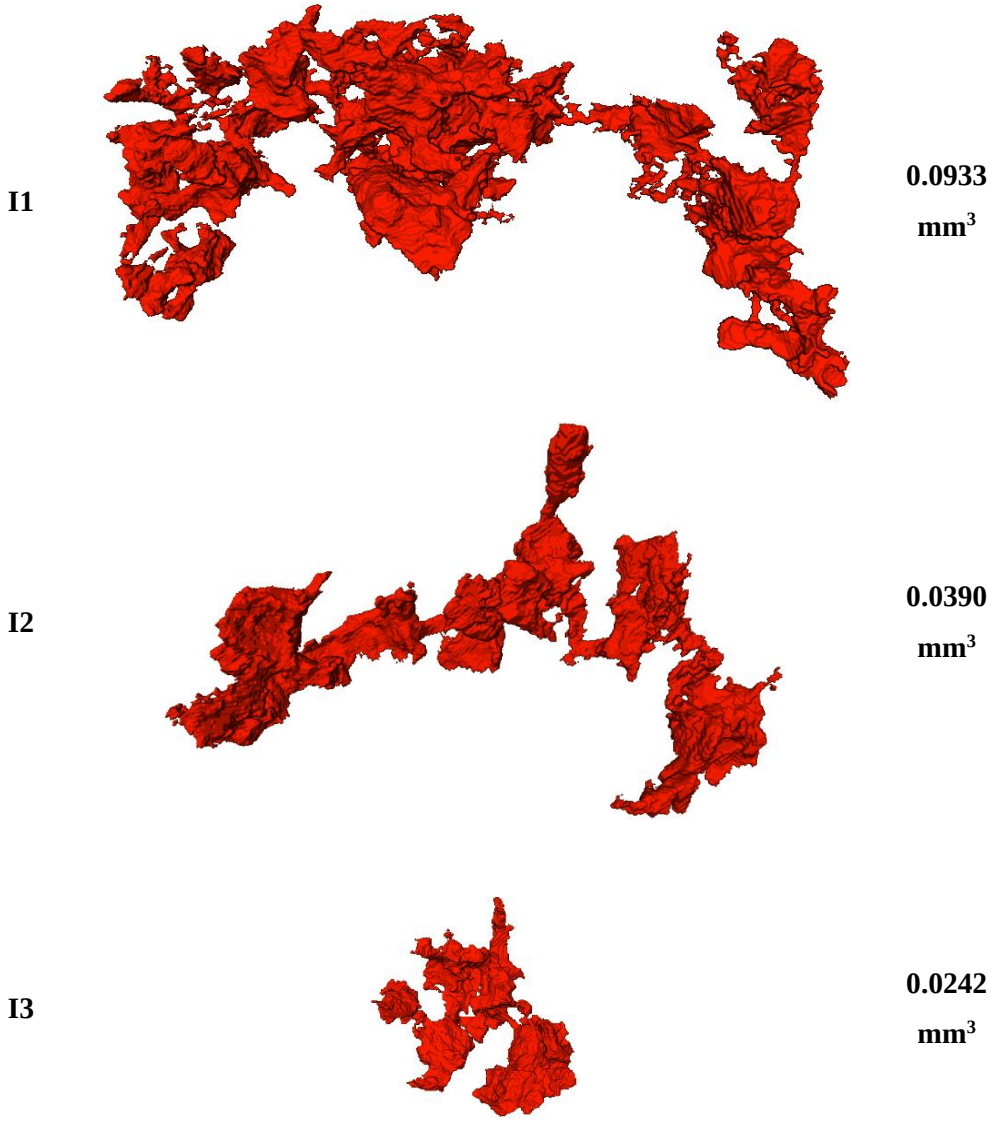

Figure 47: Visualization of the largest trapped oil cluster and its size for the I1, I2 and I3

Nanofluid flooding. A similar behaviour is observed from the 3 images for the nanofluid flooding experiments for I4, I5, and I6. With increasing the flow rate (capillary number), the amount of trapped oil reduced and the size of the residual clusters decreased, see Table 12 and Figure 48, respectively. In addition, a significant reduction in the size of the largest oil cluster at the end of the flooding, see Figure 49.

Table 12: Flow rates for the nanofluid experiments, and their corresponding S_{or} and R.F.

Experiment	Flow rate (Q)	Capillary number (C_a)	Residual oil saturation (S_{or})	Recovery factor (R.F.)
	µl/min	-	frac.	%
I4	18	2.955×10^{-05}	0.425	41.06
I5	36	5.910×10^{-05}	0.214	70.88
I6	54	8.865×10^{-05}	0.141	81.03

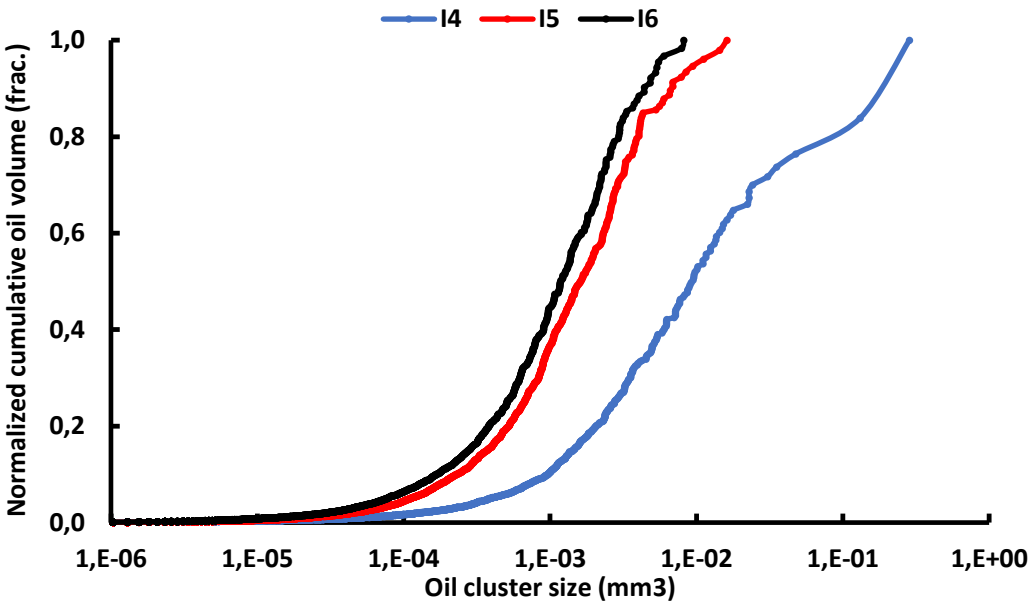

Figure 48: Normalized cumulative residual oil volume as a function of oil cluster size

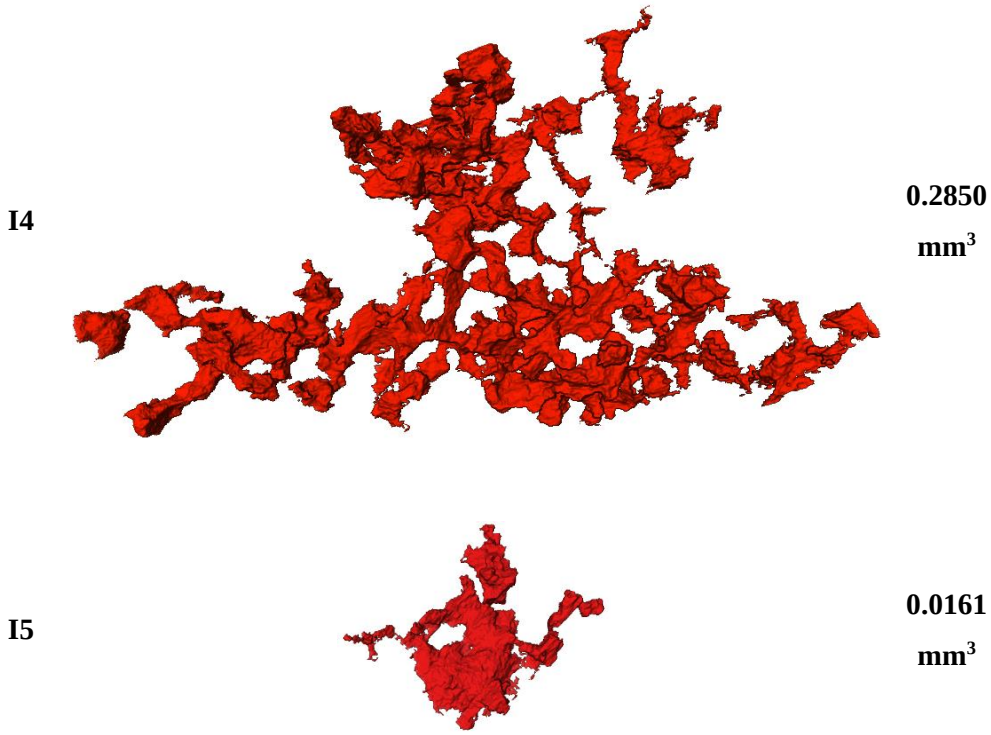

I6	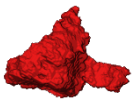	**0.0082 mm^3**

Figure 49: Visualization of the largest trapped oil cluster and its size for the I4, I5 and I6

Comparison. For the lowest capillary number ($C_a = 2.955 \times 10^{-05}$), the oil recovery factor was higher by the brine flooding, which is suspected to have higher injected pore volumes than the other experiments. However, the oil recovery factors were higher when nanoparticles used for the second and third capillary numbers. Although the capillary number of I3 was higher by 33% compared to the capillary number of I5, the later had achieved a lower residual oil saturation. higher oil recovery factor, and smaller oil clusters.

6.1.2 Residual Oil Topology

The normalized Euler characteristic of the remaining oil is used to provide more information to the effect of capillary number and fluid type on the oil phase. The equation used to normalize the Euler characteristic is equation 33 in chapter 2, since it excludes the effect of the different pore-space topology available for the fluids. Table 13 shows the maximum possible composite Euler number of the oil phase ($\chi_{100\%oil}$), (connectivity) for the analysed part of the sample, the zeroth Betti number (β_0), first Betti number (β_1), composite Euler number of the oil phase (χ_o), and the normalized Euler number ($\hat{\chi}_o$).

Table 13: Euler number and Betti numbers of the oil phase

Experiment	$\chi_{100\%oil}$	β_0	β_1	χ_o	$\hat{\chi}_o$
I1	-5388	1841	-3273	-1432	0.27
I2	-5195	1807	-2489	-682	0.13
I3	-7422	2188	-1264	924	-0.12
I4	-4759	1308	-1487	-179	0.04
I5	-4577	1653	-504	1149	-0.25
I6	-3961	1339	-167	1172	-0.30

From Table 13, the normalized Euler number decreased, which indicates less connectivity of the trapped oil phase, with increasing the flow rate (higher C_a), see Figure 50. Moreover, the post-imbibition oil connectivity was much less in the nanofluid experiments (I4: I6) compared

with the brine experiments (I1:I3). This suggest that the nanoparticles have a higher capability of dividing the oil clusters during the flooding, particularly by displacements at the pore-throats, because the number of redundant connections/loops described by β_1 was significantly lower in the presence of nanoparticles. This can be an indication of the ability of the nanoparticles to displace the oil from the smaller pore regions.

Consider experiments I1 to I4, although I4 had the highest remaining oil saturation, which should promote a higher oil connectivity, it had significantly a lower connectivity compared with the connectivity trend in the brine experiments (I1:I3), see Figure 50.

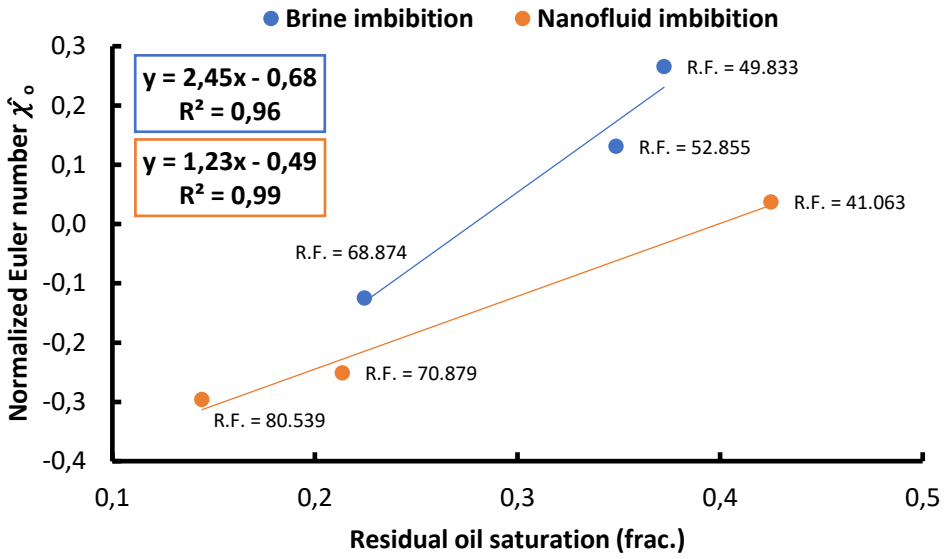

Figure 50: Normalized Euler number $\hat{\chi}_o$ as a function of S_{or} for I1 to I6

The topology of the largest remaining oil cluster after every experiment was characterized, see Figure 51. The connectedness of the biggest remaining oil cluster was lower for I5 than I3, although they have approximately the same oil recovery and remaining oil saturation. The largest cluster in I6 has no redundant loops ($\beta_1 = 0$) and Euler number of 1 representing an isolated ganglion, see Figure 49 for visualization of the cluster. This confirms the very low normalized Euler number ($\hat{\chi}_o = -0.30$) of the residual oil in the sample for experiment I6. Moreover, comparing the size and Euler number of the biggest cluster in I1, see Figure 47, to the biggest cluster in I4, confirms again that the nanoparticles had a high impact on the discontinuity of the remaining oil after an imbibition of the same capillary number.

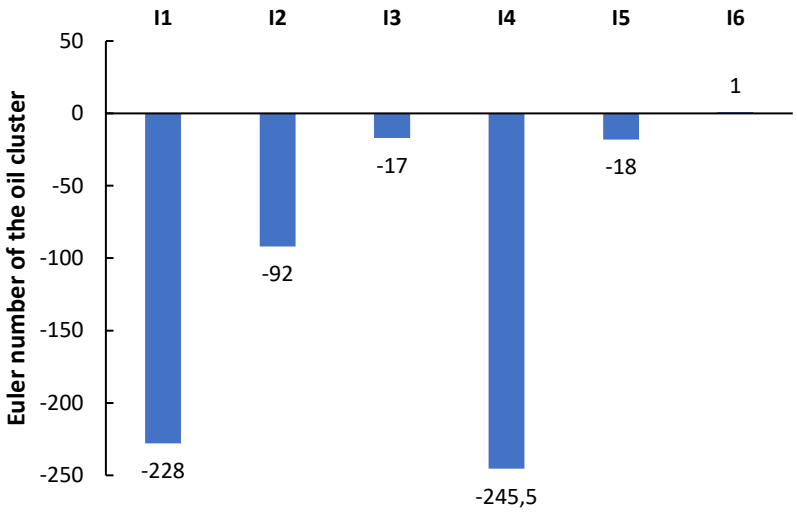

Figure 51: Euler number of the largest residual oil cluster for I1 to I6

6.1.3 Surface Area Index

The surface area index (S.A.I) quantifying the fraction of grain surfaces wetted with the aqueous phase was calculated for the six experiments, see Table 14. An experiment with a higher capillary number had a higher surface area index by comparing experiments of the same imbibition fluid. One reason of the increase in the index is the lower trapped oil in the system at higher Ca value. However, the imbibition experiments with the silica nanofluid had higher contact between the grain surfaces and nanofluid at the same capillary numbers for the brine imbibition. For example, the surface area index is 0.807 for I5, while it is 0.670 for I2. This suggests that the nanoparticles were able to detach more oil from the grain surfaces.

Table 14: Surface area index for the experiments I1 to I6

Experiment	Imbibition fluid: brine			Imbibition fluid: nanofluid		
	I1	I2	I3	I4	I5	I6
S.A.I (frac.)	0.647	0.670	0.791	0.677	0.807	0.862
S_{or} (frac.)	0.372	0.349	0.224	0.425	0.214	0.144

6.2 Tertiary Recovery by Nanofluid

The results of the 3 brine flooding experiments (I1, I2 and I3) and 3 nanofluid experiments (I4, I5 and I6) showed that nanoparticles had a higher efficiency in reducing the trapped oil phase in the Bentheimer sandstone samples, which is associated with a reduction in the residual oil connectivity and an increase in the surfaces wetted with the aqueous phase. Experiment I3 was

followed by nanofluid flooding with the same capillary number such that the flow rate was decreased. Table 15 summarizes the results pre- and post-imbibition.

Table 15: Sor, R.F., $\hat{\chi}_o$, and S.A.I. for pre- and post-tertiary recovery

Pre-tertiary recovery				Post-tertiary recovery			
S_o	R.F.	$\hat{\chi}_o$	S.A.I.	S_{or}	R.F.	$\hat{\chi}_o$	S.A.I.
frac.	%	-	frac.	frac.	%	-	frac.
0.224	68.87	-0.120	0.791	0.156	78.41	-0.209	0.852

The results show that the nanoparticles reduced the amount of trapped oil within the sample by roughly 30%, leading to an incremental oil recovery of 9.54%. In addition, the connectedness of the oil phase dropped further by 74%, see Figure 52 for comparison of the remaining oil for pre- and post-tertiary recovery. Figure 53 displays the vertical variation in oil saturation within the analysed part of the sample before and after the nanofluid injection. In addition, the injected nanofluid wetted an additional 6.1% of the grain surfaces (a change of 7.7%).

	Pre-tertiary	Post-tertiary
2D slice (oil in red, brine or nanofluid in blue and grain in gray)	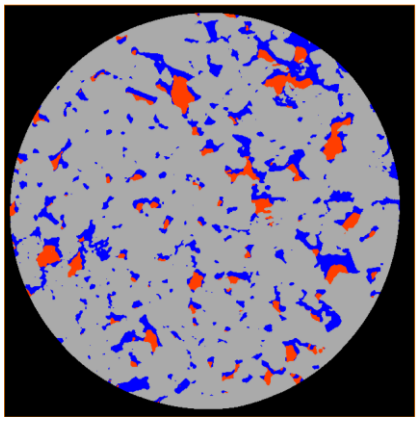	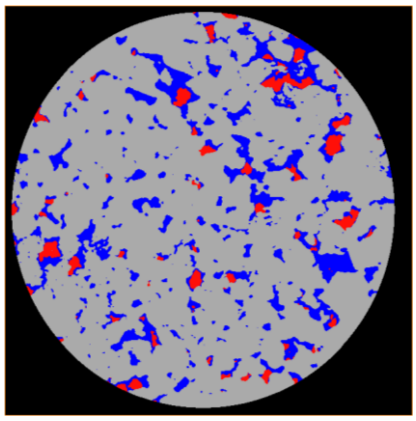
Largest oil cluster within the sample	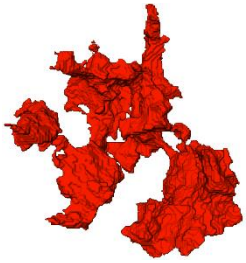 Size: 0.0243 mm^3 & $\chi_o = -17$	 Size: 0.0197 mm^3 & $\chi_o = -2$

Figure 52: Change in the remaining oil pre- and post-tertiary recovery

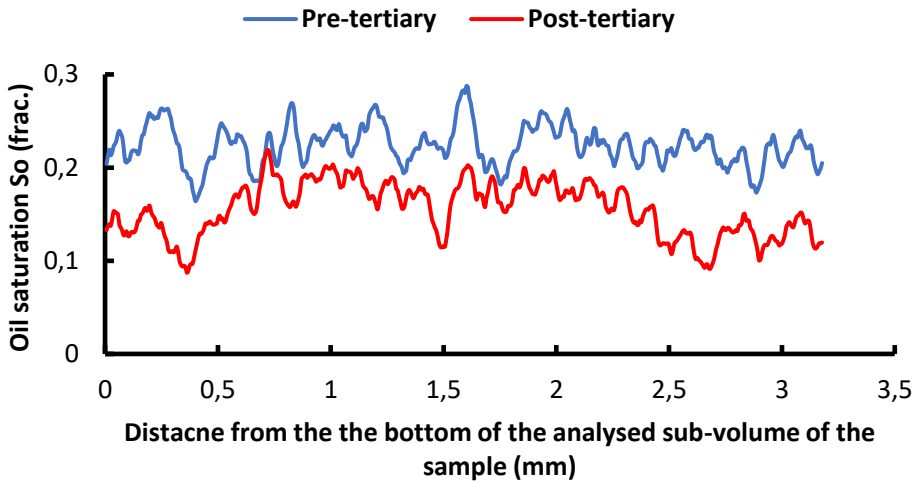

Figure 53: Vertical variation in oil saturation pre- and post-tertiary recovery

Chapter 7

Conclusions, Recommendations & Future Work

7.1 Conclusions

The following conclusions can be drawn based on the image analysis performed on open data in chapter 4, and the experimental work presented in chapter 5 and chapter 6:

- A workflow was presented to quantify the fraction of the grain surfaces in contact with the wetting phase within the sample. Application of the proposed surface area index (S.A.I.) on two open datasets showed that the index decreased as the mean in-situ contact angle increased i.e. towards a less water-wet condition. The data (S.A.I. vs. mean in-situ contact angle) was best-fitted with a line ($R^2 = 0.86$); however, more data are required to establish a better understanding of the relationship.
- In addition, it was found that the normalized Euler number of non-wetting phase was in a perfect linear relationship with the surface area index. Therefore, the index can be utilized to indicate the state of connectivity of the non-wetting phase.
- For dynamic experiments, the index was also used to differentiate between the changes within the sample by snap-off events and by dynamic displacement events such as pore-filling and throat filling.
- A flooding setup was successfully integrated with a micro-CT scanner for pore-scale trapping experiments. It was found that the challenge of removing the gas phase (i.e. air or N_2) was best solved by using back-pressure during the primary imbibition of the miniplug to dissolve the gas into the brine, in addition to flooding the sample with many pore volumes of degassed brine. Furthermore, the new adopted method to isolate the inner volume, where the sample was located, from the confining gas, significantly helped to perform long experiments (up to 16 hours) without leakage.
- 3D micro-visualization of brine (7 wt.% CsCl) imbibition tests of different flow rates (50, 100, and 150 μl/min) to recover crude oil from a Bentheimer sample showed that the residual oil saturation and remaining oil clusters size decreased. The connectivity of the oil phase post-imbibition was reduced with increasing the flow rate. The highest flow rate led to a significant disconnectedness in the residual oil phase such that the normalized Euler number was lower than zero compared to the flow rates. Moreover, the surfaces wetted with the brine, quantified with the S.A.I., increased with increasing the flow rate.

- Adding 0.1 wt.% nanosilica to the same brine to flood three miniature samples with different flow rates (18, 36, and 54 μl/min) showed a similar trend as the results found for the non-nanofluid. The capillary numbers used for the brine experiments and the nanofluid experiments were the same. The results showed that the use of nanoparticles led to a higher reduction in the amount of remaining oil and smaller sizes of the residual oil clusters compared with non-nanofluid flooding.
- Via quantifying the Euler characteristic for the remaining oil phase after nanofluid flooding, it was found that the nanoparticles had a unique ability to disconnect the remaining oil phase even when the remaining oil phase saturation was high.
- Furthermore, the nanoparticles were significantly able to detach the oil phase from the grain surfaces as shown by the surface area index. The surface area indices evaluated for the nanofluid experiments were always higher compared to the brine experiments at the same capillary numbers.
- Silica-based nanofluid of 0.1 wt.% nanosilica was a successful EOR fluid to induce positive pore-scale changes within the sample. Following a brine flooding with a nanofluid flooding resulted in a reduction in the amount of trapped oil within the sample by roughly 30%, leading to an incremental oil recovery of 9.54%. In addition, the connectedness of the oil phase dropped further by 74% and an additional 6.1% of the grain surfaces became wetted with the nanofluid.

7.2 Recommendations

The following recommendations will help to enhance the quality and efficiency of the work presented in this study.

- **Core-holder assembly.** While scanning the core-holder assembly placed on the scanner stage, it rotates 180 degrees, and consequently the tubes connected to the base of the holder rotate around the stage. During this study, the tubes were long enough to ensure that there would be no tension in the tube ends possibly leading to disconnection. However, the small production and injection tubes were subjected to possible bending during the rotation, which could lead to a higher injection pressure to ensure a constant flow rate injection due to reduction in the cross-sectional area. In addition, the possibility of the leakage was high from these bent parts during the experiments.

  Therefore, it is recommended to devote time to design a core-holder assembly to solve this issue. For example, the base could be of two parts such that the first part leads to the rotation

of the core-holder when the stage rotates, and the second part is stationary. The inner part of the core-holder may need to have a small room to receive the fluids from the tubes instead of having the tubes running inside the flow cell until the face of the sample. It is worth to conduct a survey on what is available in the market of small core-holders.

- **Degassing unit.** The fluids were subjected to a degassing process as described in chapter 5. However, the use of syringes to inject the fluids increases the chance of having small air bubbles entering from the base of these syringes, which accumulate on the surface of the base for a relatively long time, and then they travel across the syringe to be produced with the brine. This problem was solved during the experiments in this study by disconnecting the syringe and subjecting it to a degassing process. This was possible since the imbibition/drainage time was not long. However, for future experiments of very low rates, there must be a solution to avoid this issue. Therefore, it is recommended to install a small degassing unit after all the connections on the production line and before the end of the tube, see component 13 in Figure 54.

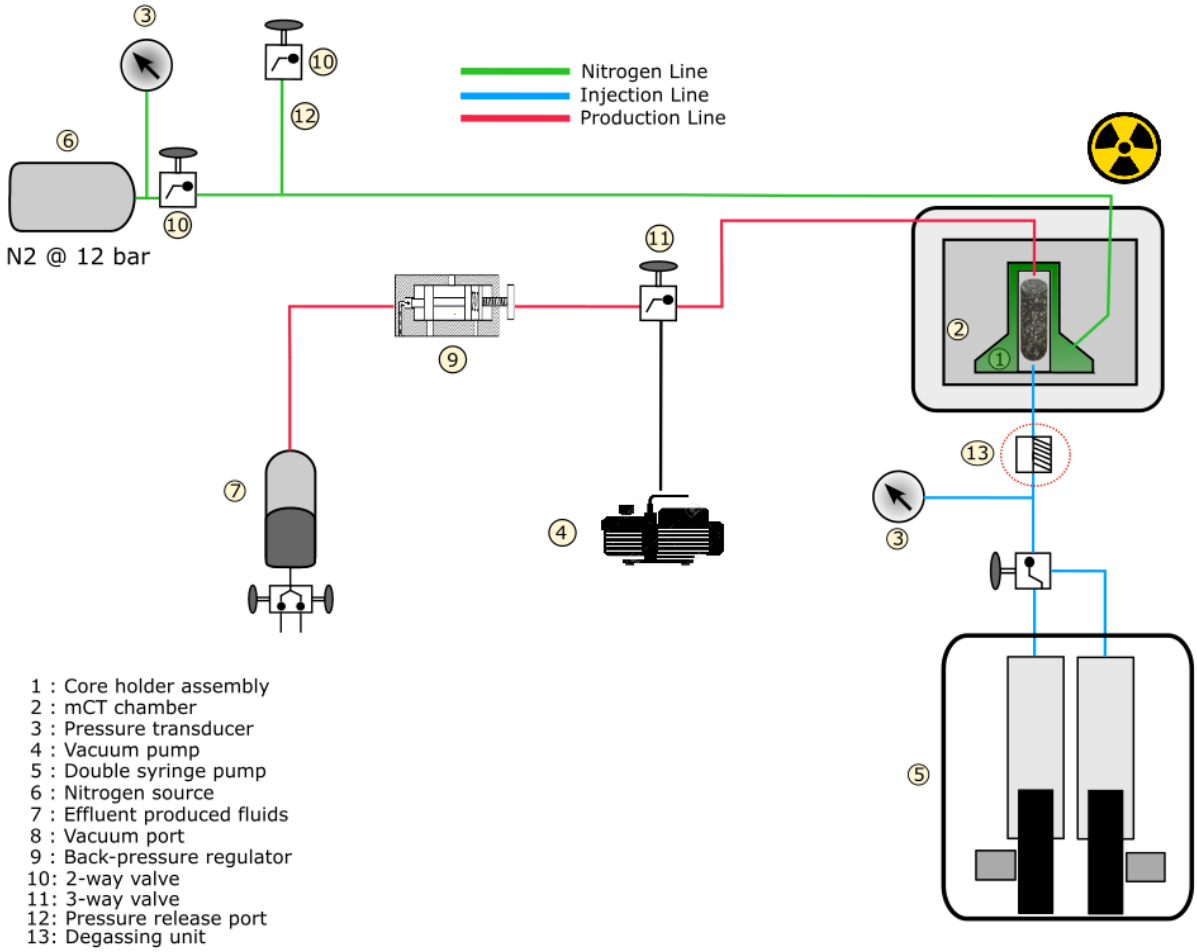

Figure 54: Modified experimental setup by adding a degassing unit in the production line

- **Differential Pressure Transmitter.** Measurement of the differential pressure of the system will enable performing simulation work based on experiments conducted using this setup in the reservoir laboratory at NTNU. Therefore, it is highly recommended to acquire a high accuracy differential pressure transmitter and to be connected as shown in Figure 55 (see component 14).

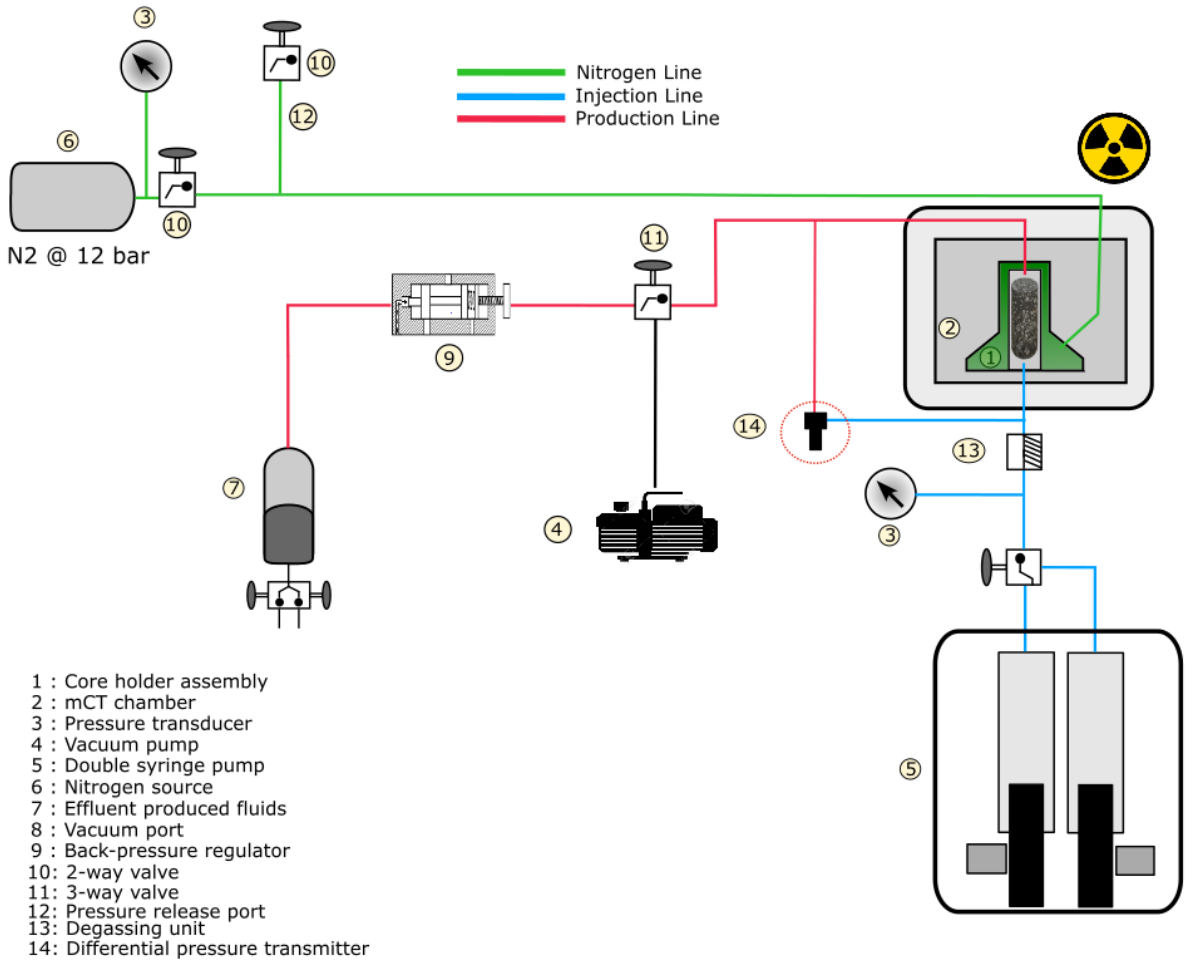

Figure 55: Modified experimental setup by adding a differential pressure transmitter

- **Image processing and analysis.** The processing and analysis of the micro-CT images is time consuming. The many steps followed to extract the data from these images are defined manually by the user. Instead of giving an order to the program to perform a single step, and then waiting until the job is finished to give the following order, effort should be devoted to write python routines to be included in the Avizo software to digitalize the work. Digitalization of the process will provide the user with more time to be more creative with the results.

7.3 Future Work

In the future, research will be devoted to gain in-depth knowledge about the surface area index and nanotechnology for EOR. The following is a list of potential experimental studies.

- A comparison study between a strongly water wet and a strongly oil wet glass bead based on the surface area index.
- Studying the surface area index hysteresis between primary drainage and imbibition using glass beads of variable wettabilities, ranging from strongly water wet to strongly oil wet.
- Acquiring vast amount of post-imbibition pore-scale experiments to establish a better understanding of the relationship between the surface area index and the in-situ contact angle.
- An experiment of a rock sample saturated with nanofluid and crude oil post-imbibition is a potential study to provide a strong pore-scale description of the detaching process by structural disjoining pressure with time. This experiment needs a new holder to prevent spontaneous imbibition from the tubes. Collaboration with the authors of [73] is also possible to apply the surface area index on their data, for example.
- Pore-scale visualization of the effect of nanoparticles concentration on the remaining oil configuration is an interesting study to explain why at a concentration of nanoparticles the oil recovery decreased as reported in core-scale studies.
- This thesis conduced only 1 tertiary experiment. Future work may include several scenarios of variable conditions for tertiary recovery coupled with micro-visualization.
- The effect of the rock wettability on the efficiency of the nanoparticles could be a possible study using the modified setup. The pore-scale changes monitored for different systems will provide new insights for the results reported on core-scale in literature.
- Work should be devoted for the digitalization of the image processing and analysis part to improve the productivity in this field of research.

References

1. Wildenschild, D. and A.P. Sheppard, *X-ray imaging and analysis techniques for quantifying pore-scale structure and processes in subsurface porous medium systems.* Advances in Water Resources, 2013. **51**: p. 217-246 DOI: https://doi.org/10.1016/j.advwatres.2012.07.018.
2. Khishvand, M., M. Akbarabadi, and M. Piri, *Micro-scale experimental investigation of the effect of flow rate on trapping in sandstone and carbonate rock samples.* Advances in Water Resources, 2016. **94**: p. 379-399 DOI: https://doi.org/10.1016/j.advwatres.2016.05.012.
3. Al-Menhali, A.S. and S. Krevor, *Capillary Trapping of CO2 in Oil Reservoirs: Observations in a Mixed-Wet Carbonate Rock.* Environmental Science & Technology, 2016. **50**(5): p. 2727-2734 DOI: 10.1021/acs.est.5b05925.
4. Herring, A.L., et al., *Effect of fluid topology on residual nonwetting phase trapping: Implications for geologic CO2 sequestration.* Advances in Water Resources, 2013. **62**: p. 47-58 DOI: https://doi.org/10.1016/j.advwatres.2013.09.015.
5. Rücker, M., et al., *From connected pathway flow to ganglion dynamics.* Geophysical Research Letters, 2015. **42**(10): p. 3888-3894 DOI: 10.1002/2015GL064007.
6. Khanamiri, H.H. and O. Torsæter, *Fluid Topology in Pore Scale Two-Phase Flow Imaged by Synchrotron X-ray Microtomography.* Water Resources Research, 2018. **54**(3): p. 1905-1917 DOI: 10.1002/2017WR021302.
7. Armstrong, R.T., et al., *Flow regimes during immiscible displacement.* Petrophysics, 2017. **58**(01): p. 10-18.
8. Schlüter, S., et al., *Pore-scale displacement mechanisms as a source of hysteresis for two-phase flow in porous media.* Water Resources Research, 2016. **52**(3): p. 2194-2205 DOI: 10.1002/2015WR018254.
9. Armstrong, R.T., et al., *Beyond Darcy's law: The role of phase topology and ganglion dynamics for two-fluid flow.* Physical Review E, 2016. **94**(4): p. 043113.
10. Valori, A. and B. Nicot, *A REVIEW OF 60 YEARS OF NMR WETTABILITY.* International Symposium of the Society of Core Analysts held in Trondheim, 2018.
11. Khishvand, M., A.H. Alizadeh, and M. Piri, *In-situ characterization of wettability and pore-scale displacements during two- and three-phase flow in natural porous media.* Advances in Water Resources, 2016. **97**: p. 279-298 DOI: https://doi.org/10.1016/j.advwatres.2016.10.009.
12. Andrew, M., B. Bijeljic, and M.J. Blunt, *Pore-scale contact angle measurements at reservoir conditions using X-ray microtomography.* Advances in Water Resources, 2014. **68**: p. 24-31 DOI: https://doi.org/10.1016/j.advwatres.2014.02.014.
13. Blunt, M.J., *Multiphase flow in permeable media: A pore-scale perspective*. 2017: Cambridge University Press.

14. Raeini, A.Q., B. Bijeljic, and M.J. Blunt, *Generalized network modeling of capillary-dominated two-phase flow*. Physical Review E, 2018. **97**(2): p. 023308 DOI: 10.1103/PhysRevE.97.023308.
15. AlRatrout, A., M.J. Blunt, and B. Bijeljic, *Wettability in complex porous materials, the mixed-wet state, and its relationship to surface roughness.* Proceedings of the National Academy of Sciences, 2018. **115**(36): p. 8901.
16. Lv, P., et al., *Pore-Scale Imaging and Analysis of Phase Topologies and Displacement Mechanisms for CO2-Brine Two-Phase Flow in Unconsolidated Sand Packs.* 2017. **53**(11): p. 9127-9144 DOI: 10.1002/2016wr020270.
17. Berg, S., et al., *Onset of Oil Mobilization and Nonwetting-Phase Cluster-Size Distribution.* Petrophysics, 2015. **56**(01): p. 15-22.
18. Herring, A.L., et al., *Efficiently engineering pore-scale processes: The role of force dominance and topology during nonwetting phase trapping in porous media.* Advances in Water Resources, 2015. **79**: p. 91-102 DOI: https://doi.org/10.1016/j.advwatres.2015.02.005.
19. Andrew, M., B. Bijeljic, and M.J. Blunt, *Pore-scale imaging of trapped supercritical carbon dioxide in sandstones and carbonates.* International Journal of Greenhouse Gas Control, 2014. **22**: p. 1-14 DOI: https://doi.org/10.1016/j.ijggc.2013.12.018.
20. Klise, K.A., et al., *Automated contact angle estimation for three-dimensional X-ray microtomography data.* Advances in Water Resources, 2016. **95**: p. 152-160 DOI: https://doi.org/10.1016/j.advwatres.2015.11.006.
21. AlRatrout, A., et al., *Automatic measurement of contact angle in pore-space images.* Advances in Water Resources, 2017. **109**: p. 158-169 DOI: https://doi.org/10.1016/j.advwatres.2017.07.018.
22. Lv, P., et al., *Pore-scale contact angle measurements of CO2-brine-glass beads system using micro-focused X-ray computed tomography.* IET Micro & Nano Letters, 2016. **11**(9): p. 524-527 DOI: https://doi.org/10.1049/mnl.2016.0215.
23. *The World Energy Outlook 2018*. 2018.
24. *BP Statistical Review of World Energy 2018*. 2018.
25. Cheraghian, G. and L. Hendraningrat, *A review on applications of nanotechnology in the enhanced oil recovery part B: effects of nanoparticles on flooding.* International Nano Letters, 2016. **6**(1): p. 1-10 DOI: 10.1007/s40089-015-0170-7.
26. Kamal, M.S., et al., *Recent advances in nanoparticles enhanced oil recovery: rheology, interfacial tension, oil recovery, and wettability alteration.* Journal of Nanomaterials, 2017. **2017**.
27. Negin, C., S. Ali, and Q. Xie, *Application of nanotechnology for enhancing oil recovery – A review*. Petroleum, 2016. **2**(4): p. 324-333 DOI: https://doi.org/10.1016/j.petlm.2016.10.002.
28. Donaldson, E.C. and W. Alam, *Wettability*. 2008, Houston, TX: Gulf Pub. Company.

29. Herring, A.L., et al., *Observations of nonwetting phase snap-off during drainage.* Advances in Water Resources, 2018. **121**: p. 32-43 DOI: https://doi.org/10.1016/j.advwatres.2018.07.016.
30. Scanziani, A., et al., *Automatic method for estimation of in situ effective contact angle from X-ray micro tomography images of two-phase flow in porous media.* Journal of Colloid and Interface Science, 2017. **496**: p. 51-59 DOI: https://doi.org/10.1016/j.jcis.2017.02.005.
31. AlRatrout, A., et al., *Automatic measurement of contact angle in pore-space images.* Advances in Water Resources, 2017. **109**(Supplement C): p. 158-169 DOI: https://doi.org/10.1016/j.advwatres.2017.07.018.
32. Herring, A.L., V. Robins, and A.P. Sheppard, *Topological Persistence for Relating Microstructure and Capillary Fluid Trapping in Sandstones.* Water Resources Research, 2018. **0**(ja) DOI: 10.1029/2018WR022780.
33. Tanino, Y. and M.J. Blunt, *Capillary trapping in sandstones and carbonates: Dependence on pore structure.* Water Resources Research, 2012. **48**(8) DOI: 10.1029/2011WR011712.
34. Wardlaw, N.C. and L. Yu, *Fluid topology, pore size and aspect ratio during imbibition.* Transport in Porous Media, 1988. **3**(1): p. 17-34 DOI: 10.1007/BF00222684.
35. Al-Gharbi, M.S. and M.J. Blunt, *Dynamic network modeling of two-phase drainage in porous media.* Physical Review E, 2005. **71**(1): p. 016308 DOI: 10.1103/PhysRevE.71.016308.
36. Yuan, C., B. Chareyre, and F. Darve, *Pore-scale simulations of drainage in granular materials: Finite size effects and the representative elementary volume.* Advances in Water Resources, 2016. **95**: p. 109-124 DOI: https://doi.org/10.1016/j.advwatres.2015.11.018.
37. Bultreys, T., et al., *Real-time visualization of Haines jumps in sandstone with laboratory-based microcomputed tomography.* Water Resources Research, 2015. **51**(10): p. 8668-8676 DOI: 10.1002/2015WR017502.
38. Armstrong, R.T., et al., *Modeling the velocity field during Haines jumps in porous media.* Advances in Water Resources, 2015. **77**: p. 57-68 DOI: https://doi.org/10.1016/j.advwatres.2015.01.008.
39. Singh, K., et al., *Dynamics of snap-off and pore-filling events during two-phase fluid flow in permeable media.* Scientific Reports, 2017. **7**(1): p. 5192 DOI: 10.1038/s41598-017-05204-4.
40. Schlüter, S., et al., *Image processing of multiphase images obtained via X-ray microtomography: A review.* Water Resources Research, 2014. **50**(4): p. 3615-3639 DOI: 10.1002/2014WR015256.
41. Klaus, M. and C.H. Arns, *Fluids in porous media: a morphometric approach.* Journal of Physics: Condensed Matter, 2005. **17**(9): p. S503.
42. Liu, Z., et al. *Prediction of Permeability from Euler Characteristic of 3D Images*. in *International Symposium of the Society of Core Analysts*. 2017.

43. Khanamiri, H.H., et al., *Description of Free Energy for Immiscible Two-Fluid Flow in Porous Media by Integral Geometry and Thermodynamics.* Water Resources Research, 2018. **0**(0) DOI: 10.1029/2018WR023619.
44. Wildenschild, D. and A.P. Sheppard, *X-ray imaging and analysis techniques for quantifying pore-scale structure and processes in subsurface porous medium systems.* Advances in Water Resources, 2013. **51**(Supplement C): p. 217-246 DOI: https://doi.org/10.1016/j.advwatres.2012.07.018.
45. Kumar, S., et al., *Interfacial Interaction of Cationic Surfactants and Its Effect on Wettability Alteration of Oil-Wet Carbonate Rock.* Energy & Fuels, 2016. **30**(4): p. 2846-2857 DOI: 10.1021/acs.energyfuels.6b00152.
46. Amott, E., *Observations Relating to the Wettability of Porous Rock.* Petroleum Transactions, AIME, 1959. **216**: p. 156-162.
47. Salathiel, R.A., *Oil Recovery by Surface Film Drainage In Mixed-Wettability Rocks.* Journal of Petroleum Technology, 1973. **25**(10): p. 1216 - 1224 DOI: https://doi.org/10.2118/4104-PA.
48. Hendraningrat, L. and O. Torsæter, *Effects of the Initial Rock Wettability on Silica-Based Nanofluid-Enhanced Oil Recovery Processes at Reservoir Temperatures.* Energy & Fuels, 2014. **28**(10): p. 6228-6241 DOI: 10.1021/ef5014049.
49. Carpenter, C., *A Study of Wettability-Alteration Methods With Nanomaterials Application.* 2015 DOI: 10.2118/1215-0074-JPT.
50. Amirpour, M., et al., *Experimental investigation of wettability alteration on residual oil saturation using nonionic surfactants: Capillary pressure measurement.* Petroleum, 2015. **1**(4): p. 289-299.
51. Tiab, D. and E.C. Donaldson, *Petrophysics: theory and practice of measuring reservoir rock and fluid transport properties*. 2015: Gulf professional publishing.
52. Treiber, L.E. and W.W. Owens, *A Laboratory Evaluation of the Wettability of Fifty Oil-Producing Reservoirs.* Society of Petroleum Engineers Journal, 1972. **12**(06): p. 531-540 DOI: 10.2118/3526-PA.
53. Morrow, N.R., *Capillary Pressure Correlations For Uniformly Wetted Porous Media.* Journal of Canadian Petroleum Technology, 1976. **15**(04): p. 22 DOI: 10.2118/76-04-05.
54. Chilingar, G.V. and T.F. Yen, *Some Notes on Wettability and Relative Permeabilities of Carbonate Reservoir Rocks, II.* Energy Sources, 1983. **7**(1): p. 67-75 DOI: 10.1080/00908318308908076.
55. Yuan, Y. and T.R. Lee, *Contact Angle and Wetting Properties*, in *Surface Science Techniques*, G. Bracco and B. Holst, Editors. 2013, Springer Berlin Heidelberg: Berlin, Heidelberg. p. 3-34.

56. Deglint, H., et al., *Comparison of Micro- and Macro-Wettability Measurements for Unconventional Reservoirs: The Devil is in the Detail*, in *Unconventional Resources Technology Conference, Austin, Texas, 24-26 July 2017*. 2017, Society of Exploration Geophysicists, American Association of Petroleum Geologists, Society of Petroleum Engineers. p. 2544-2552.
57. Cnudde, V. and M.N. Boone, *High-resolution X-ray computed tomography in geosciences: A review of the current technology and applications.* Earth-Science Reviews, 2013. **123**: p. 1-17 DOI: https://doi.org/10.1016/j.earscirev.2013.04.003.
58. Cnudde, V., et al., *Recent progress in X-ray CT as a geosciences tool.* Applied Geochemistry, 2006. **21**(5): p. 826-832 DOI: https://doi.org/10.1016/j.apgeochem.2006.02.010.
59. Alhammadi, A.M., et al., *In situ characterization of mixed-wettability in a reservoir rock at subsurface conditions.* Scientific Reports, 2017. **7**(1): p. 10753 DOI: 10.1038/s41598-017-10992-w.
60. Singh, K., B. Bijeljic, and M.J. Blunt, *Imaging of oil layers, curvature and contact angle in a mixed-wet and a water-wet carbonate rock.* Water Resources Research, 2016. **52**(3): p. 1716-1728 DOI: 10.1002/2015WR018072.
61. Lv, P., et al., *In Situ Local Contact Angle Measurement in a CO2–Brine–Sand System Using Microfocused X-ray CT.* Langmuir, 2017. **33**(14): p. 3358-3366 DOI: 10.1021/acs.langmuir.6b04533.
62. Idowu, N., et al. *Wettability analysis using micro-CT, FESEM and QEMSCAN, and its applications to digital rock physics*. in *International Symposium of the Society of Core Analysts*. 2015.
63. AlRatrout, A., M.J. Blunt, and B. Bijeljic, *Spatial Correlation of Contact Angle and Curvature in Pore-Space Images.* Water Resources Research, 2018. **54**(9): p. 6133-6152 DOI: 10.1029/2017WR022124.
64. Scanziani, A., et al., *In situ characterization of immiscible three-phase flow at the pore scale for a water-wet carbonate rock.* Advances in Water Resources, 2018. **121**: p. 446-455 DOI: https://doi.org/10.1016/j.advwatres.2018.09.010.
65. Cense, A. and S. Berg. *The viscous-capillary paradox in 2-phase flow in porous media*. in *International Symposium of the Society of Core Analysts held in Noordwijk, The Netherlands*. 2009.
66. Chatzis, I., M.S. Kuntamukkula, and N.R. Morrow, *Effect of Capillary Number on the Microstructure of Residual Oil in Strongly Water-Wet Sandstones.* SPE Reservoir Engineering, 1988. **3**(03): p. 902-912 DOI: 10.2118/13213-PA.
67. Wildenschild, D., et al., *Exploring capillary trapping efficiency as a function of interfacial tension, viscosity, and flow rate.* Energy Procedia, 2011. **4**: p. 4945-4952 DOI: https://doi.org/10.1016/j.egypro.2011.02.464.

68. Krummel, A.T., et al., *Visualizing multiphase flow and trapped fluid configurations in a model three-dimensional porous medium.* AIChE Journal, 2013. **59**(3): p. 1022-1029 DOI: 10.1002/aic.14005.
69. Georgiadis, A., et al., *Pore-scale micro-computed-tomography imaging: Nonwetting-phase cluster-size distribution during drainage and imbibition.* Physical Review E, 2013. **88**(3): p. 033002 DOI: 10.1103/PhysRevE.88.033002.
70. Heshmati, M. and M. Piri, *Interfacial boundary conditions and residual trapping: A pore-scale investigation of the effects of wetting phase flow rate and viscosity using micro-particle image velocimetry.* Fuel, 2018. **224**: p. 560-578 DOI: https://doi.org/10.1016/j.fuel.2018.03.010.
71. Mahmud, W.M. and V.H. Nguyen, *Effects of snap-off in imbibition in porous media with different spatial correlations.* Transport in porous media, 2006. **64**(3): p. 279-300.
72. Akai, T., et al., *Modeling Oil Recovery in Mixed-Wet Rocks: Pore-Scale Comparison Between Experiment and Simulation.* Transport in Porous Media, 2018 DOI: 10.1007/s11242-018-1198-8.
73. Zhang, H., et al., *Enhanced Oil Recovery Driven by Nanofilm Structural Disjoining Pressure: Flooding Experiments and Microvisualization.* Energy & Fuels, 2016. **30**(4): p. 2771-2779 DOI: 10.1021/acs.energyfuels.6b00035.
74. Pak, T., et al., *The Dynamics of Nanoparticle-enhanced Fluid Displacement in Porous Media - A Pore-scale Study.* Scientific Reports, 2018. **8**(1): p. 11148 DOI: 10.1038/s41598-018-29569-2.
75. Li, S. and O. Torsæter, *Experimental Investigation of the Influence of Nanoparticles Adsorption and Transport on Wettability Alteration for Oil Wet Berea Sandstone*, in *SPE Middle East Oil & Gas Show and Conference*. 2015, Society of Petroleum Engineers: Manama, Bahrain. p. 16.
76. Li, S. and O. Torsaeter, *The Impact of Nanoparticles Adsorption and Transport on Wettability Alteration of Intermediate Wet Berea Sandstone*, in *SPE Middle East Unconventional Resources Conference and Exhibition*. 2015, Society of Petroleum Engineers: Muscat, Oman. p. 14.
77. Li, S., et al., *Experimental Study of Wettability Alteration during Nanofluid Enhanced Oil Recovery Process and Its Effect on Oil Recovery*, in *SPE Reservoir Characterisation and Simulation Conference and Exhibition*. 2015, Society of Petroleum Engineers: Abu Dhabi, UAE. p. 11.
78. Maghzi, A., et al., *Monitoring wettability alteration by silica nanoparticles during water flooding to heavy oils in five-spot systems: A pore-level investigation.* Experimental Thermal and Fluid Science, 2012. **40**: p. 168-176 DOI: https://doi.org/10.1016/j.expthermflusci.2012.03.004.

79. Li, R., et al., *Experimental Investigation of Silica-Based Nanofluid Enhanced Oil Recovery: The Effect of Wettability Alteration.* Energy & Fuels, 2017. **31**(1): p. 188-197 DOI: 10.1021/acs.energyfuels.6b02001.
80. Li, S., et al., *Effect of Silica Nanoparticles Adsorption on the Wettability Index of Berea Sandstone*. The international symposium of the society of core analysts (SCA) California, USA, 2013.
81. Wasan, D.T. and A.D. Nikolov, *Spreading of nanofluids on solids.* Nature, 2003. **423**: p. 156 DOI: 10.1038/nature01591 https://www.nature.com/articles/nature01591#supplementary-information.
82. Kondiparty, K., et al., *Wetting and Spreading of Nanofluids on Solid Surfaces Driven by the Structural Disjoining Pressure: Statics Analysis and Experiments.* Langmuir, 2011. **27**(7): p. 3324-3335 DOI: 10.1021/la104204b.
83. Kondiparty, K., et al., *Dynamic Spreading of Nanofluids on Solids. Part I: Experimental.* Langmuir, 2012. **28**(41): p. 14618-14623 DOI: 10.1021/la3027013.
84. Wang, D., et al., *Mechanism Discussion of Nanofluid for Enhanced Oil Recovery: Adhesion Work Evaluation and Direct Force Measurements between Nanoparticles and Surfaces.* Energy & Fuels, 2018. **32**(11): p. 11390-11397 DOI: 10.1021/acs.energyfuels.8b02825.
85. Zhang, H., A. Nikolov, and D. Wasan, *Enhanced Oil Recovery (EOR) Using Nanoparticle Dispersions: Underlying Mechanism and Imbibition Experiments.* Energy & Fuels, 2014. **28**(5): p. 3002-3009 DOI: 10.1021/ef500272r.
86. Li, S. and O. Torsæter, *An Experimental Investigation of EOR Mechanisms for Nanoparticles Fluid in Glass Micromodel*. The international symposium of the society of core analysts (SCA) Avignon, France, 2014.
87. Agista, M., K. Guo, and Z. Yu, *A State-of-the-Art Review of Nanoparticles Application in Petroleum with a Focus on Enhanced Oil Recovery.* Applied Sciences, 2018. **8**(6): p. 871.
88. Torsæter, O. and M. Abtahi, *Experimental Reservoir Engineering Laboratory Work Book, first edition.* 2003: Norwegian University of Science and Technology.
89. Averill, B.A. and P. Eldredge, *Principles of general chemistry.* Creative Commons, 2012.

Appendices

Appendix A: Rock properties

Porosity. The porosity of the parent rock plug was measured using a helium porosimeter (manufactured by Core Laboratories, USA) based on Boyle's law, see Figure 56. The volume of the void space in the holder occupied by the helium gas is given by V_1 when the holder is empty (no sample) and V_2 when the sample is placed in the holder. For the parent Bentheimer sandstone plug (diameter = 3.78 cm and length = 4.55 cm) used in this study, the porosity was found to be 16.77%.

Data:

$V_1 = 63\ cm^3$ and $V_2 = 20.5\ cm^3$

Calculation:

Plug bulk volume $(V_b) = \pi \frac{3.78^2}{4} \cdot 4.55 = 51.06\ cm^3$

Plug grain volume $(V_g) = V_1 - V_2 = 63 - 20.5 = 42.5\ cm^3$

Plug pore volume $(V_p) = V_b - V_g = 51.06 - 42.5 = 8.56\ cm^3$

Porosity $(\emptyset) = \frac{V_p}{V_b} = \frac{8.56}{51.06} = 0.1677 = 16.77\%$

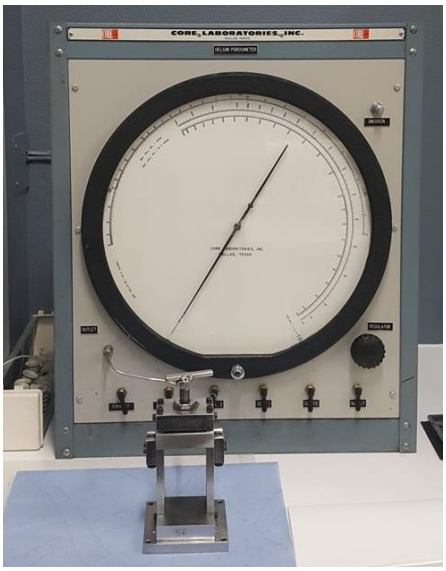

Figure 56: Helium porosimeter (manufactured by Core Laboratories, USA) based on Boyle's law

Liquid permeability. The liquid permeability was estimated using Klinkenberg correlation between apparent gas permeability at mean pressures and the true liquid permeability [87]. Figure 57 shows the experiment setup in the reservoir laboratory at NTNU. Table 16 provides the recorded data in the lab and the calculated parameters using equation 1 and 2 for the plot in Figure 58 [87]. The extrapolation of the best-fit line to the data gives a y-axis intercept of 962.99 mD which is the approximated liquid permeability.

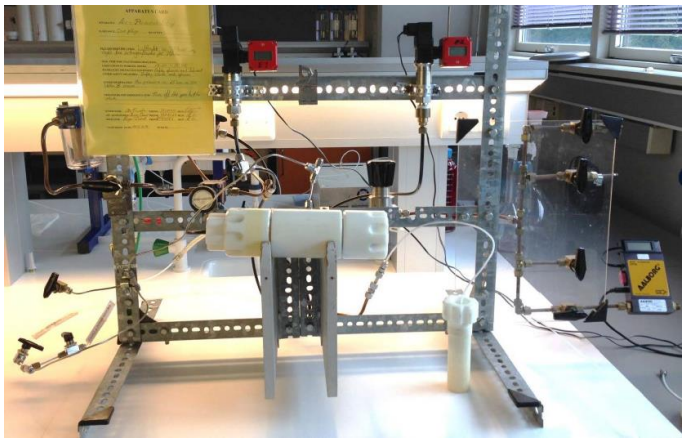

Figure 57: Apparatus for measuring gas permeability

$$Q_{atm} = \frac{A\,k_a}{\mu_{N_2} L}\frac{(P_1^2 - P_2^2)}{2P_{atm}} \quad (1)$$

$$P_m = \frac{(P_1 + P_2)}{2} \quad (2)$$

Where:

Q_{atm} : Volumetric flow rate, (cm^3/sec)
A : Cross-sectional area of the plug, (cm^2)
k_a : Apparent gas permeability, (Darcy)
L : Plug length, cm
P_1 : Inlet pressure, atm
P_2 : Outlet pressure, atm
P_{atm} : atmospheric pressure (1 atm)
μ_{N_2} : Viscosity of flowing nitrogen gas, cp
P_m : Mean pressure, atm

Table 16: Recorded experimental data and calculated parameters to estimate the liquid permeability

Recorded data					Calculated parameters for Figure 58	
P_1	P_2	ΔP	Q	Q	$1/P_m$	k_a
[bara]	[bara]	[bar]	[L/min]	[cm^3/sec]	[atm^{-1}]	[mD]
1.10	1.00	0.10	1.70	28.33	0.95	1958.39
1.20	1.10	0.10	1.76	29.33	0.87	1851.21
1.30	1.20	0.10	1.87	31.17	0.80	1809.56
1.40	1.30	0.10	1.95	32.50	0.74	1747.20
1.50	1.40	0.10	2.00	33.33	0.69	1668.41

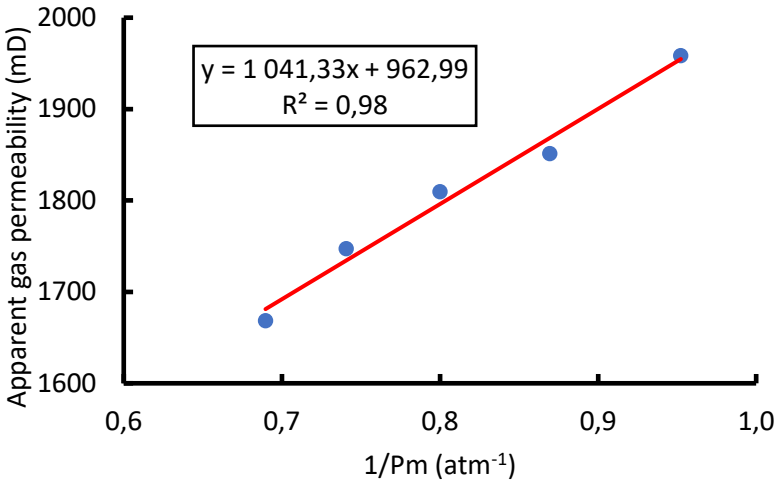

Figure 58: Plot to estimate the liquid permeability using the Klinkenberg method

X-ray porosity. The miniplug were scanned in the micro-CT and then images are processes, see chapter 5 for details, and finally the pore space is segmented from the grain phase by using watershed segmentation method included in Avizo Software 9.2 (developed by Thermo Fisher Scientific). The segmented image will have a label of 0 for the pore space and a label of 1 for the grain phase. Using label analysis, the pore-space (porosity) of the sample is found and also the porosity distribution of the sample along the sample length (z-direction) is found. Sample S5 was imaged with a high resolution of 2.4 µm, the captured part of the sample was 8.3 cm in length, and the porosity variation with length from the bottom to the top of this part is presented in Figure 59. The average porosity of the captured section of the sample is 16.56%.

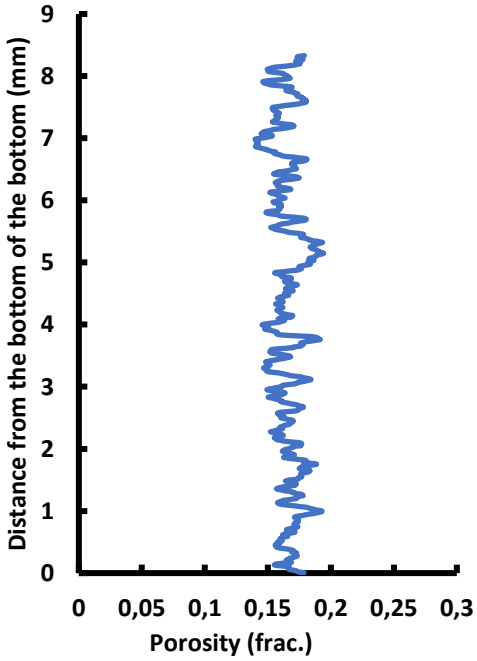

Figure 59: Variation of porosity with length for sample S5

Appendix B: Pre-injection fluid preparation

Filtration. The filtration process was for the crude oil phase to avoid the presence of particles, such as debris, which can plug the pore-throats of the sample or the 1/32-inch tubes attached to the core-holder assembly. Figure 60 shows the four stages of filtration, based on the pore-size of the membrane filter (produced by Merck Millipore, USA). The use of four different filters increases the efficiency of the process (less time and no leakage in the setup) since the plugging of the filter pores is reduced by filtration the biggest particles in the first stages. Figure 61 shows the setup used to filter the crude oil.

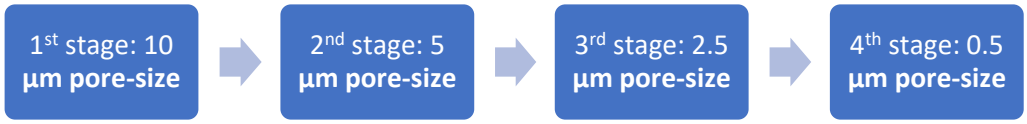

Figure 60: The pore-size of the membrane filter used in every stage to filter the crude oil

Figure 61: Setup for filtering the crude oil under vacuum

Degassing. This process is important to remove the gas dissolved in the brine and crude oil. The dissolved gas in the liquid phases can lead to gas/air bubbles formation in the porous medium which is undesirable event. There are three problems caused by the presence of air bubbles in the sample: (1) the presence of the gas phase in the sample as air bubbles led to the requirement of higher injection pressure of the fluid to maintain the flow rate. (2) the gas phase occupies some pores resulting in less pore volume for the tested liquid phases (3) the gas phase

may look like trapped small oil ganglia in the micro-CT images and thus a higher oil saturation will be calculated.

Figure 62 shows that (a) a glass bottle with a two-port cap is connected to (b) a vacuum pump (manufactured by Edwards, UK) through one port (in red circle) and the other port is closed by a plastic plug (in green circle). This method results in properly degassed liquid and provides the user the means to seal the system after the process, which is faster than the traditionally used method in the lab by the system in Figure 61. For this study, the degassing time was around 2 hours for 125 ml. In addition, after filling the syringe with the liquid, the syringe was also connected to the second port of the glass bottle to remove any air bubbles formed during the filling process of the syringe, see Figure 63.

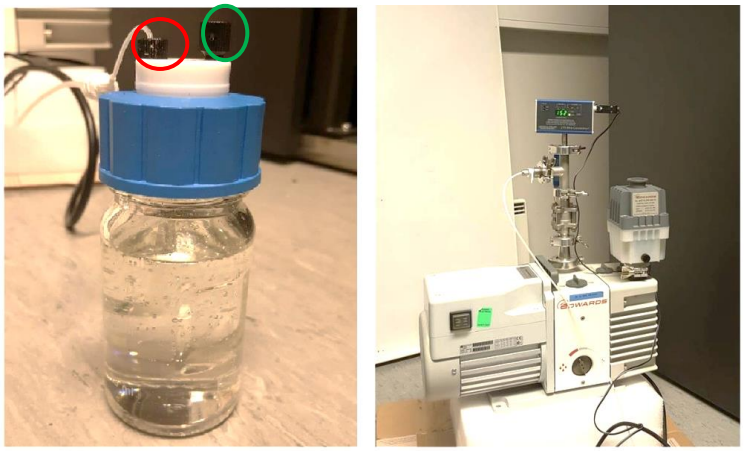

Figure 62: Setup for degassing the liquid consisting of a glass bottle and vacuum pump

Figure 63: Demonstration of connecting the syringe to the degassing system to remove the air bubbles

Appendix C: Best sealing practice for the flow cell

The best sealing practice for the core-holder to ensure that the confining air does not enter to the inner volume of the sleeve where the sample is placed, is as follows:

1. The process starts with the base of the flow cell. Two O-rings should be installed on the part indicated with the red arrow, see Figure 64 (a).
2. After that, this part is wrapped with a Teflon tape as shown in the Figure 64 (b).
3. Next the sleeve is installed such that it should be forced to the end but not to cover the hole indicated with a green arrow, see Figure 64 (c). Because the confining gas passes through this small hole.
4. The sample is placed carefully into the sleeve, Figure 64 (d).
5. Two 1/16-inch tubes should be connected to the holes on the base as shown in the Figure 64 (e), to protect them from the glue that will be used to seal the lower end of the sleeve, in the next step.
6. Hot melt adhesive (HMA) which commonly known as hot glue is used to seal the lower end of the sleeve, see Figure 64 (f). This type of glue is selected since it can be removed after the experiments easily with heating up to 100 ^{o}C, which is acceptable since the temperature resistance of the core holder is 200 ^{o}C.
7. Two O-rings should be installed on the top part of the flow cell as shown in Figure 64 (g). HMA should be added on O-rings and to be given time to harden. Otherwise, the O-rings can easily move to the top while pushing the sleeve part.
8. The top part is connected to the sleeve and small amount of HMA is added around the contact between the top part and the sleeve top end, see Figure 64 (h).
9. Next, a heat-shrinkable Viton tube is added to the top part, see Figure 64 (i), providing an extra seal. This technique is not needed for the lower part. The upper part needs it since the room in the top of the core-holder is so tight, which may remove the glue which installing the flow cell in the core-holder.
10. The flow cell is placed in the oven for 2 mins at 80 ^{o}C to make the Viton rubber shrink around the top and make the HMA homogenous around the top and bottom end of the sleeve, as shown in Figure 64 (j).
11. After letting the flow cell to cool down, it is installed in the core-holder and a sealing test outside the micro-CT scanner is performed as a final check.

This re-producible method was the best to solve the issue among several other techniques.

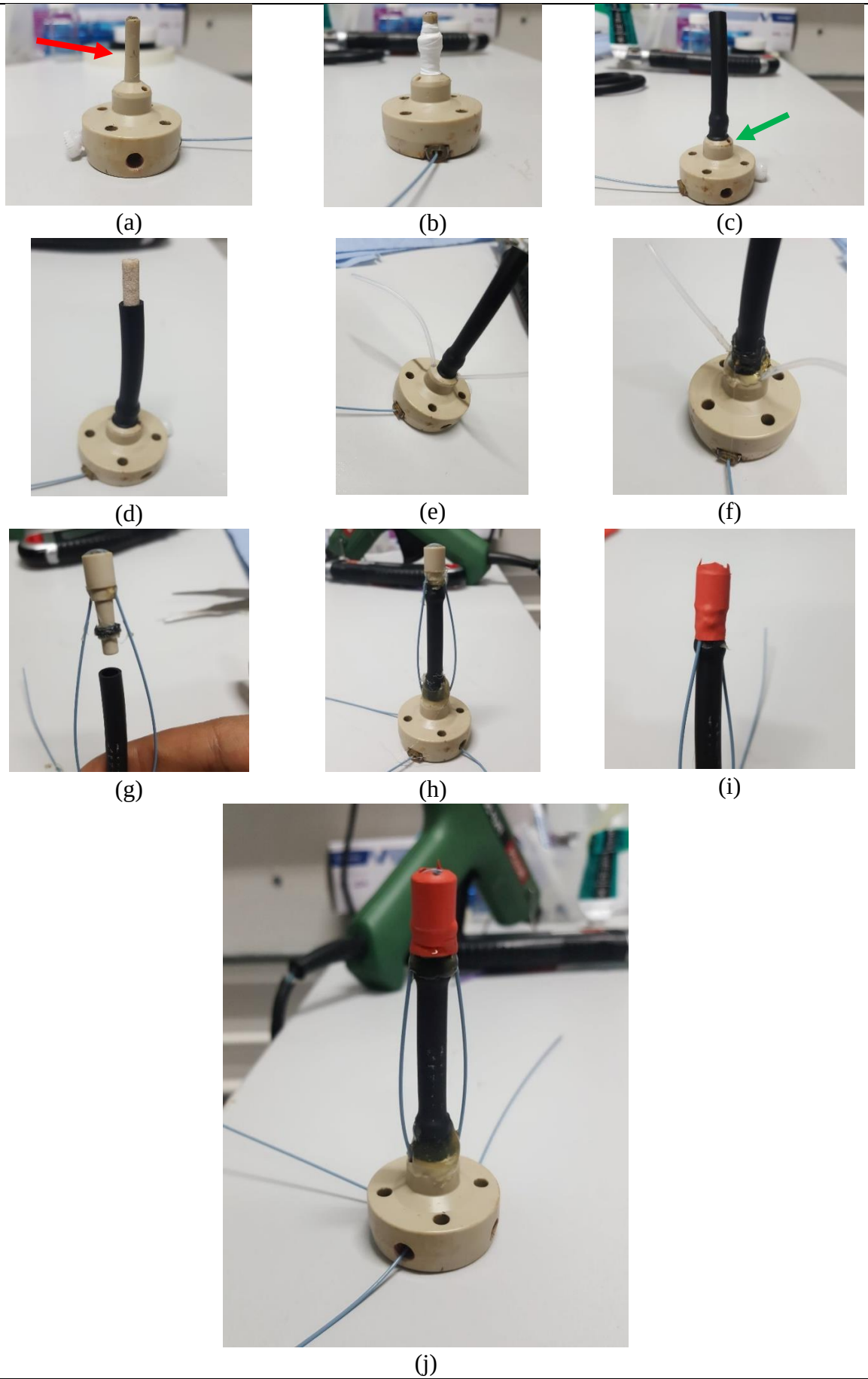

Figure 64: Demonstration of the steps followed to seal the flow cell

Appendix D: Image Processing

The main steps to process the obtained images from the Skyscan 1172 scanner are as follows:

1. The images contain the medium around the miniature sample, including: the sleeve, core-holder, and the small tubes. Therefore, the first step is to crop out these parts from the image, which also reduces the size of the images enabling faster computation for the next steps. Figure 65 shows an example of images pre- and post-cropping.

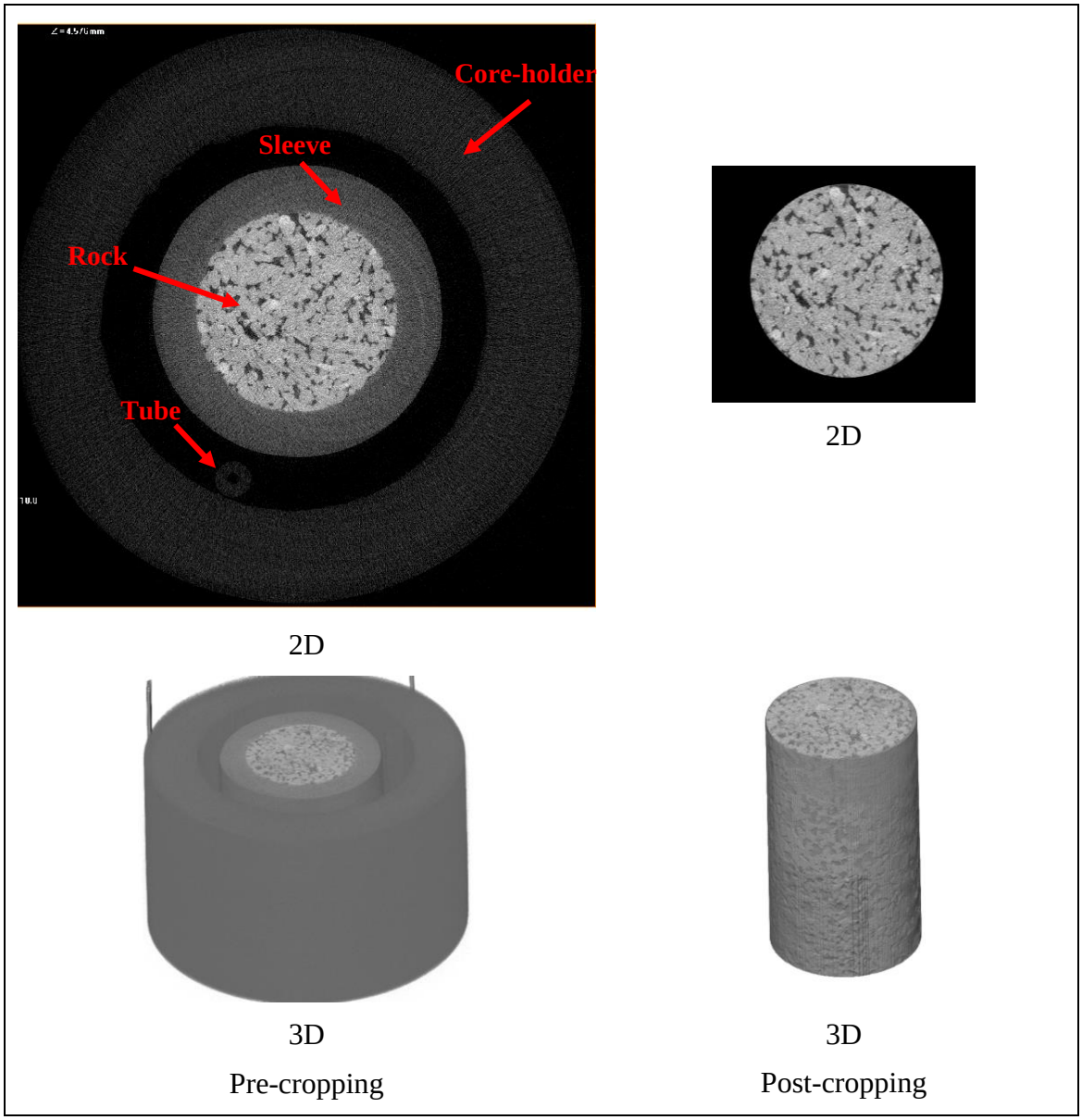

Figure 65: Demonstration of the micro-CT images pre- and post-cropping

2. The images have noise that should be removed using a denoising filter. A highly cited filter in recent studies on pore-scale investigation of porous media is the Non-Local Means filter [2, 11, 12, 17, 19, 39, 60]. Figure 66 shows a 2D slice before and after denoising with NLM filter.

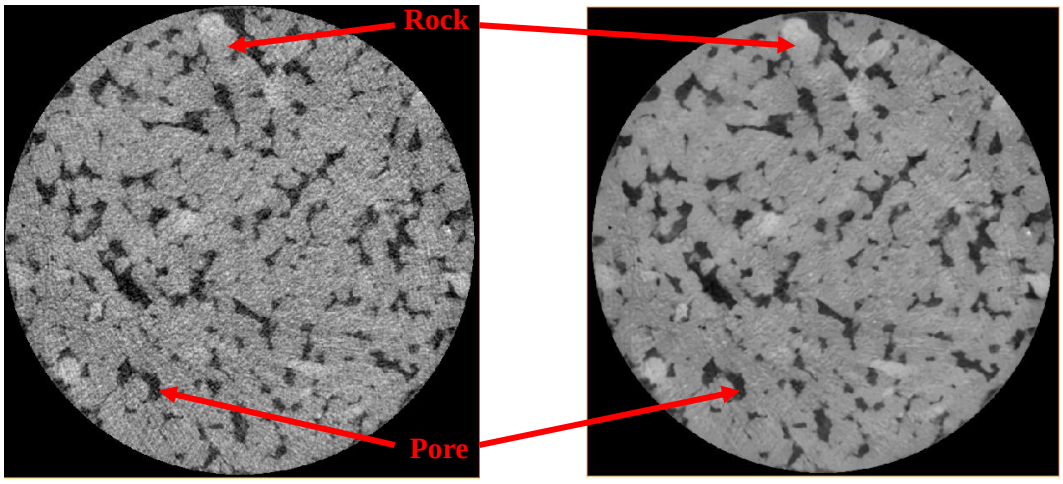

Pre-filtered image Filtered image

Figure 66: Comparison between non-filtered and filtered image with the NLM filter

3. The next step is to segment the grain phase from the void phase with a seeded watershed algorithm included in Avizo Software 9.2 (developed by Thermo Fisher Scientific), based on the 3D gray-scale gradient of the filtered image, see Figure 67.

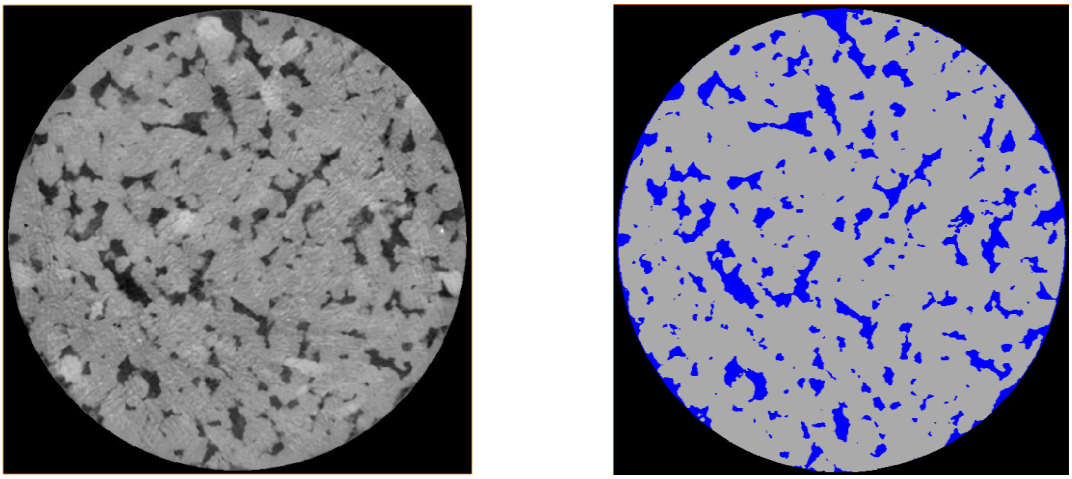

Gray-scale image Segmented image

Figure 67: Demonstration of a gray-scale image and its corresponding segmented image

4. A rock phase is extracted from the segmented images and used as a mask for the wet images to exclude it from the image after a registration process between the dry and wet image. As a result, the wet image will only have two phases; the brine and the oil, which makes it easier to segment them compared with a wet image of three phases. The reason

is that the gray-scale boundaries between the phases will not be distinguished. Figure 68 shows a wet image containing brine (in light gray) and oil (in dark gray) after masking it with the grain phase (in black), and the corresponding segmented image where grain is in gray, brine in blue and oil in red.

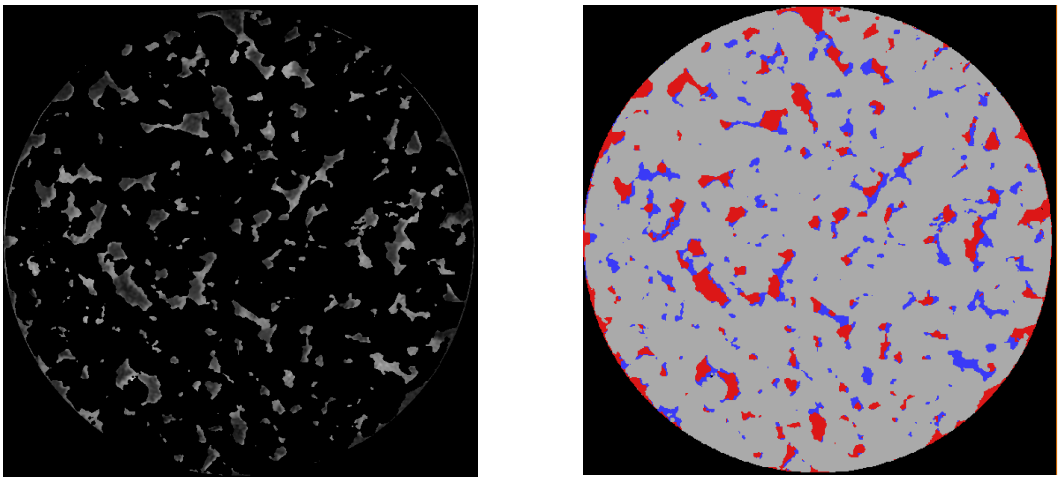

Masked image Segmented image

Figure 68: Masked image and its corresponding segmented image